Dynamic Neural Network-based Pulsed Plasma Thruster (PPT) Fault Detection and Isolation for the Attitude Control Subsystem of Formation Flying Satellites

Arturo Valdes

A Thesis

In

The Department

of

Electrical and Computer Engineering

Presented in Partial Fulfillment of the Requirements
For the Degree of Master in Applied Science (Electrical Engineering) at
Concordia University
Montreal, Quebec, Canada

May 2008

Your file Votre référence
ISBN: 978-0-494-42518-3
Our file Notre référence
ISBN: 978-0-494-42518-3

Abstract

Dynamic Neural Network-based Pulsed Plasma Thruster (PPT) Fault Detection and Isolation for the Attitude Control Subsystem of Formation Flying Satellites

Arturo Valdes

The main objective of this thesis is to develop a dynamic neural network-based fault detection and isolation (FDI) scheme for the Pulsed Plasma Thrusters (PPTs) that are used in the Attitude Control Subsystem (ACS) of satellites that are tasked to perform a formation flying mission. In order to accomplish these objectives three fault detection and isolation (FDI) approaches based on dynamic neural networks (DNN) are developed: (i) a "Low Level" FDI scheme, (ii) a "High Level" FDI scheme, and (iii) an "Integrated" FDI scheme. Based on data that is collected from the electrical circuit of the PPTs, our proposed "Low Level" FDI scheme can detect and isolate faults in the PPT actuators. Using a Confusion Matrix evaluation system we demonstrate that can achieve a high level of accuracy but the precision level is below expectations and the misclassification rate is expressed as False Healthy and False Faulty parameters is significant. Our proposed "High Level" FDI scheme utilizes data collected from the relative attitudes of the formation flying satellites. According to the simulation results, our proposed FDI scheme can detect the pair of thrusters which is faulty. It represents a promising detection capability, however its isolation capabilities are not adequate. Finally, our proposed "Integrated" FDI scheme takes advantage of the strengths of each of the previous schemes and at same time reduces their individual weaknesses. To demonstrate its capabilities, various fault scenarios were simulated. The results demonstrate a high level of accuracy (99.79%) and precision (99.94%) with a misclassification rate that is quite negligible. Furthermore, our proposed "Integrated" FDI scheme provides additional and interesting information related to the effects of faults in the thrust production levels that would not be available from simply the low and high levels separately.

Acknowledgements

This work was performed at the Department of Electrical and Computer Engineering at Concordia University. First, I would like to thank my supervisor, Dr. K. Khorasani for letting me join his group of research and patiently answering my questions. Also, I would like to thank the members of the Fault Diagnosis and Isolation Research Group for our discussions and positive atmosphere.

Secondly, I would like to thank the Ministerio de Planificación y Cooperación of Chile (MIDEPLAN) for economically supporting me during the entire period of study and research.

And last, but definitely not least, I would like to thank my amazing wife Karla for her infinite patience, collaboration, and care during the last two years.

Table of Contents

List of Figures

List of Tables

Nomenclature

a_i	:	IIR filter i-th feedback parameter
A_{th}	:	Torque matrix
b	:	Superscript indicates the spacecraft body fixed coordinate system
b_i	:	IIR filter i-th feed-forward parameter
BE	:	Top event
C	:	Capacitance (F)
DNN_{roll}	:	Dynamic neural network (roll angle)
DNN_{pitch}	:	Dynamic neural network (pitch angle)
DNN_{yaw}	:	Dynamic neural network (yaw angle)
$\vec{e}_{th}$	:	Unit thrust vector
e	:	Neural network estimation error (training phase)
f	:	Pulse requency (Hz)
$\vec{f}_{null}$	:	Nullspace component
$\vec{f}_{sys}$	:	Binary on-off set of signals
F_{th}	:	Magnitude of the thrust force
$\vec{F}_{th}$	:	Thrust force generated for each thruster
${}^{follower,j}_{leader}q_1$	:	angle rotation about the x-axis ($s/c_{f,j}$ w.r.t. s/c_l)
${}^{follower,j}_{leader}q_2$	:	angle rotation about the y-axis ($s/c_{f,j}$ w.r.t. s/c_l)
${}^{follower,j}_{leader}q_3$	:	angle rotation about the z-axis ($s/c_{f,j}$ w.r.t. s/c_l)
${}^{follower,j}_{leader}\Delta\omega_x$	:	angle velocity about the x-axis ($s/c_{f,j}$ w.r.t. s/c_l)
${}^{follower,j}_{leader}\Delta\omega_y$	:	angle velocity about the y-axis ($s/c_{f,j}$ w.r.t. s/c_l)
${}^{follower,j}_{leader}\Delta\omega_z$	:	angle velocity about the z-axis ($s/c_{f,j}$ w.r.t. s/c_l)
${}^{follower,j}_{leader}T_{PPT1/PPT2}$	:	sequence of pulses about the x-axis ($s/c_{f,j}$ w.r.t. s/c_l)
${}^{follower,j}_{leader}T_{PPT3/PPT4}$	:	sequence of pulses about the y-axis ($s/c_{f,j}$ w.r.t. s/c_l)
${}^{follower,j}_{leader}T_{PPT5/PPT6}$	:	sequence of pulses about the z-axis ($s/c_{f,j}$ w.r.t. s/c_l)
$g\|F(\cdot)$	:	Activation function of the neuron

h	:	Distance between electrodes (m)
$\vec{h}$	:	Angular momentum of the spacecraft
i	:	Counter used to identify the *i-th* axis
$\vec{I}$	:	Inertia matrix of the spacecraft
$\mathbf{1}$	:	Identity matrix
IE	:	Intermediate vent
j	:	Counter used to identify the *j-th* follower spacecraft
$J \times B$	:	Lorentz force
$\mathbf{K_d}$	:	Diagonal gain matrix of the angular velocity term of the controller
$k_{d,1}$	:	First element of the diagonal gain matrix $\mathbf{K_d}$
$k_{d,2}$	:	Second element of the diagonal gain matrix $\mathbf{K_d}$
$k_{d,3}$	:	Third element of the diagonal gain matrix $\mathbf{K_d}$
$\mathbf{K_p}$	:	Diagonal gain matrix of the error quaternion term of the controller
$k_{p,1}$	:	First element of the diagonal gain matrix $\mathbf{K_p}$
$k_{p,2}$	:	Second element of the diagonal gain matrix $\mathbf{K_p}$
$k_{p,3}$	:	Third element of the diagonal gain matrix $\mathbf{K_p}$
L_c	:	Internal Inductance of the capacitor (H)
L_e	:	Inductance due to wires and leads (H)
L_{pe}	:	Inductance due to current sheet moving down (H)
L'_{pe}	:	Inductance per unit channel length (Hm^{-1})
L_T	:	Total circuit inductance (H)
m_0	:	Mass of plasma at $t = 0$ (kg)
mse	:	Mean square error
MAE	:	Mean absolute error
n_e	:	Electron density (m^{-3})
o	:	Subscript indicates orbital reference coordinate system
$PPT_{i,(+)}$	:	PPT which generates thrust in the positive direction of the *i-th* axis
$PPT_{i,(-)}$	:	PPT which generates thrust in the negative direction of the *i-th* axis
$\underline{q}$	:	Quaternion attitude representation vector (4x1)
$\bar{q}$	:	Quaternion axes rotation vector (3x1)
$\bar{\mathbf{q}}$	:	Skew-symmetric matrix
q_0	:	Quaternion magnitude rotation

q_1	:	Quaternion angular rotation about the x-axis of the spacecraft
q_2	:	Quaternion angular rotation about the y-axis of the spacecraft
q_3	:	Quaternion angular rotation about the z-axis of the spacecraft
$\bar{q}_E$	:	Error quaternion vector
R_c	:	Capacitor resistance (Ω)
R_e	:	Wire and lead resistance (Ω)
R_p	:	Plasma resistance (Ω)
R_{pe}	:	Electrode resistance (Ω)
R_T	:	Total circuit resistance (Ω)
SAE	:	Sum absolute error
s/c_{f1}	:	Follower 1 spacecraft
s/c_{f2}	:	Follower 2 spacecraft
s/c_l	:	Leader spacecraft
$\bar{r}_{th}$	:	Position vector
$t.c.$	:	Termination criterion
$\bar{T}$	:	Total torque action on the spacecraft
TE	:	Basic event
$\bar{T}_{com}$	:	Commanded torque vector
T_e	:	Electron temperature
$\bar{T}_{sys}$	:	Total control torque applied
$T_{sys,i}$	:	Producible torque in direction of the *i-th* axis
$\bar{T}_{th}$	:	Generated torque about the CoM of the spacecraft
T_x	:	Total torque applied about the x-axis of the CoM of the spacecraft
T_y	:	Total torque applied about the y-axis of the CoM of the spacecraft
T_z	:	Total torque applied about the z-axis of the CoM of the spacecraft
u_i	:	Nullspace command
$U(k)$	:	Neural Network input vector
μ_0	:	Magnetic permeability of free space ($WbA^{-1}m^{-1}$)
$v(t)$	:	Capacitor voltage
v_i	:	Capacitor voltage of the PPTs which generate thrust in the *i-th* axis
V_{max}	:	Maximum capacitor voltage charge

w	:	Width of electrodes (m)
W	:	Neural network weight vector
$\vec{\omega}$	:	Rotational rate vector of the spacecraft
ω_x	:	Angular velocity of the CoM of the spacecraft w.r.t. the x-axis
ω_y	:	Angular velocity of the CoM of the spacecraft w.r.t. the y-axis
ω_z	:	Angular velocity of the CoM of the spacecraft w.r.t. the z-axis
$\vec{x_l}$	:	Leader's state vector
$\vec{x_{f1}}$	:	Follower 1's state vector
x_1	:	Position state variable
x_2	:	Charge on capacitor state variable
x_3	:	Velocity state variable
x_4	:	Current state variable
$y_1(t)$	:	Thrust
$y_2(t)$	:	Discharge current
y_{1min}	:	Minimum healthy thrust
y_{1max}	:	Maximum healthy thrust
$y_{1nominal}$	:	Nominal thrust
$y_{i,(+)}$	:	Discharge current of the $PPT_{i,(+)}$
$y_{i,(-)}$	:	Discharge current of the $PPT_{i,(-)}$
[x y z] (ECI)	:	Three axes representation in Earth centered inertial coordinate system
[x y z] (ECF)	:	Three axes representation in Earth centered earth fixed coordinate system
[x y z] (body)	:	Three axes representation in satellite body fixed coordinate system
φ	:	Roll angle
φ_{max}	:	Maximum roll angle
θ	:	Pitch angle
θ_{max}	:	Maximum pitch angle
ψ	:	Yaw angle
ψ_{max}	:	Maximum yaw angle
σ	:	Threshold sensitivity parameter
$\Delta\omega_{max}$	:	Maximum angular velocity
$\Delta\omega_{min}$	:	Minimum angular velocity
$\Delta\vec{\omega}$	:	Rotational rate Vector
τ	:	Characteristic pulse time (s)

Chapter 1

Introduction

1.1 Statement of the Problem

Traditionally, space missions have been extremely expensive and that cost is directly related to the size and weights of the space vehicle (i.e. spacecraft) that is sent to the space. The new generation of space missions are evolved to groups of coordinated small-size spacecraft that can perform the same mission that a large spacecraft can achieve but with much reduced mission cost ([1]-[13]). One type of coordinated small-size spacecraft missions is called formation flying mission. There are a number of examples of formation flying missions for deep space environment (such as ST-3, TPF, LISA, DARWIN [14]-[16]) and formation flying missions for near-Earth environment (EO-1, ION-F, PRISMA, CLS3, SMART-2 [16]-[23]). Some of the most important issues related with the formation of spacecraft are: (i) collisions avoidance between the members of the formation during orbital or attitude maneuvers, and (ii) precise formation keeping during the execution of the mission. These two issues can be ideally fulfilled with an appropriate control law and precise sensors and actuators. However, malfunctions of any of these components can affect the performance of the formation. Early detection of malfunctions or faults is mandatory for this type of missions.

Fault detection is the process of declaring the presence of a fault based on the presence of an abnormality in the system. This is the first step for understanding the occurrence of malfunctions or failures. Once the fault is detected, fault isolation must be performed. Fault isolation goes one step further and implies the identification of the faulty component. A system with detection and isolation capabilities is known as Fault Detection and Isolation (FDI) system. FDI systems have been developed for various types of controlled systems. During the spacecraft missions, engineers

do not have physical access to the system and its components therefore, only limited FDI systems have been employed for this application. FDI systems for the attitude and orbital control subsystems of spacecraft have been developed in the last two decades. Literature on FDI systems for spacecraft provides some examples of FDI systems for faulty components such as sensors, actuators, and controllers ([24]-[32]).

The types of actuators and sensors utilized for a spacecraft depend on the objective of the mission. For attitude maneuvers, the most commonly used actuator is the reaction wheel. It is a precise and reliable actuator but its size and weight can be a limitation. Thrusters are the other alternative to reaction wheels. They use propellant for generating forces in the direction of which the propellant is discharged. Based on the type of propellant and configuration, they are divided into different categories such as Ion Thrusters ([33]-[37]), Hall Thrusters ([38]-[46]), Colloid Thrusters ([47]-[49]), Magneto Plasma Dynamic (MPD) Thrusters ([50]-[53]), Pulsed Plasma Thrusters ([54]-[63]), among others ([64]-[66]). Pulsed Plasma Thruster (PPT) actuator can reach the same accuracy level than that of reaction wheels but at lower cost, mass and complexity. Furthermore, a PPT system can be used for different purposes such as stationkeeping, attitude control and orbit insertion and drag make-up. Unfortunately, the amount of force generated by a PPT cannot be measured and therefore, faults that produce undesirable variations in the amount of force generated by the thruster are not observable.

Currently, the development of a FDI system for detecting and isolating faults in PPT thrusters of formation flying spacecraft is a challenging problem and a necessity. The desirable autonomous FDI system must be capable of detecting faults and isolating the faulty thrusters among all the members of the formation flying spacecraft system.

1.2 Objectives of the Research

The main objective of this thesis is to provide a solution to the fault detection and isolation problem of formation flying spacecraft mission with faults affecting the actuators of the attitude control subsystem. In order to fulfill this objective, the actuators and the formation flying dynamics are presented and explained. The characteristics and the capabilities of different FDI techniques are analyzed and compared prior to selecting the Dynamic Neural Networks (DNNs) as the more appropriate FDI technique for this specific application. Finally, we develop a compact and reliable FDI scheme capable of detecting and isolating faults. The expected FDI scheme must fulfill minimum requirements of accuracy and precision avoiding misclassification and false alarms.

1.3 Contributions of this Thesis

The contributions of the work developed in this thesis are detailed as follows:

- A novel Fault Detection and Isolation (FDI) scheme for Pulsed Plasma Thrusters (PPTs) of the Attitude Control Subsystem (ACS) of formation flying satellites has been proposed and tested by using simulated formation flying missions. By means of four Dynamic Neural Networks (DNN) the proposed FDI scheme is capable of detecting and isolating faults of the actuators (i.e. PPTs) which affect the precision of the formation flying attitudes.
- The results obtained show high levels of accuracy (99.79%) and precision (99.94%) and the misclassification rate of the False Healthy (0.03%) and the False Faulty (0.61%) parameters are quite negligible. Therefore, the applicability of the DNN technique for solving fault diagnosis problems in highly complex nonlinear systems such as formation flying systems has been demonstrated.
- Although there are a number of results in the literature on fault diagnostic of the standard attitude control actuators (e.g. reaction wheels), the development of fault diagnostic systems

for Pulsed Plasma Thrusters is not covered in the literature. Since the force generated by this actuators cannot be measured and due to the lack of precise mathematical models, the development of fault diagnostic system for PPTs is not a trivial work. In this thesis, we demonstrate that our proposed FDI scheme is a not computationally intensive and is a reliable tool for detecting and isolating faulty PPTs.

- Formation Flying missions are starting to gain popularity due to the advantages that are offered by these systems. A significant reduction in the amount of hours spent by the ground station personnel can be reached by implementing our proposed DNN-based FDI schemes. Therefore the cost of the mission can be significantly reduced.

1.4 Outline of the Thesis

In Chapter 2, FDI methods available in the literature for dynamical systems are reviewed and classification of different FDI techniques is presented. Development of FDI systems for spacecraft especially for formation flying spacecraft attitude control subsystem (ACS) is addressed. Two general FDI approaches are presented as examples of the actual level of development of FDI schemes for ACS of single spacecraft. Finally, the necessity of FDI for actuators of the ACS of spacecraft in formation flying missions is discussed.

In Chapter 3, the concepts of coordinate systems and attitude representation techniques are defined and explained. The equations of motion that describe the rotational dynamics of the spacecraft are presented. The concept of formation flying spacecraft is introduced. Formation flying control architectures and formation flying control laws are also provided and design of the formation flying control laws are provided. Finally, the pulsed plasma thrusters (PPT) are introduced as actuators of our formation flying spacecraft and the dynamical model describing the PPT's electromechanical system and PPT configurations are also provided. The dynamics of formation flying and the PPT's electromechanical systems are presented in this chapter. They are used to simulate the satellite's attitude maneuvers under normal and abnormal PPT's conditions

to provide the required data for developing and testing our proposed FDI schemes.

In Chapter 4, a dynamic neural network-based fault detection and isolation scheme for the PPT system of a spacecraft is developed. This scheme avoids the need for directly measuring the generated thrust that in real operational situation is not available. By using a dynamic model of the PPT, we simulated the operation of this actuator under healthy and faulty conditions. The data set collected from these simulations are used for evaluating the FDI scheme.

In Chapter 5, an alternative dynamic neural network-based fault detection and isolation scheme is developed. This FDI scheme requires data from the attitude control subsystem of the formation flying system and not from the actuators. The simulation results are discussed and compared with the results of the previously proposed FDI schemes.

In Chapter 6, the strengths and weaknesses of both FDI schemes are discussed and an integrated FDI scheme capable of taking advantages of the strengths of each scheme and at same time reducing their individual weaknesses is proposed. Various fault scenarios are simulated and the performance of our proposed FDI scheme is evaluated and compared to the FDI scheme that is proposed in Chapter 4. Finally, the promising advantages of our proposed integrated FDI scheme are presented and the precision and accuracy of the FDI scheme are evaluated.

In Chapter 7, the main conclusion and the most important contributions of this thesis are presented and explained. Finally, possible future research work based on the contributions made in this thesis is provided.

Chapter 2

Fault Detection and Isolation

2.1 Fault Detection and Isolation Problem

In order to fully understand the concept of fault detection and isolation, we first introduce the most important and general definitions and nomenclatures in this field. According to [67], fault can be defined as a departure from an acceptable range of an observable variable or a calculated parameter associated with a process. This definition implies that a fault can be understood as a process abnormality or symptom. Therefore, failure can be understood as a total process malfunction. In this context, a general controlled process system may be composed of the plant, sensors, controllers and actuators. As shown in Figure 2.1, faults and failures can occur in any of these components. Fault detection is the action of declaring the presence of a fault based on the presence of an abnormality whereas, fault isolation goes one step further and implies the identification of the faulty component. According to [68] fault detection is the process which indicates that a malfunction is affecting the system and fault isolation is the process that by means of analyzing the fault detection alarms proposes hypotheses of the faults. A system capable of detecting and isolating a fault in a general system is known as the Fault Detection and Isolation (FDI) system. Malfunctioning sensors and actuators, structural changes in the dynamic plant and complications in the controller are the most common sources of failures. As examples of FDI systems, [135] and [136] present different approaches for detecting and isolating faulty sensors and actuators meanwhile [137] provides a general architecture for fault tolerant controllers.

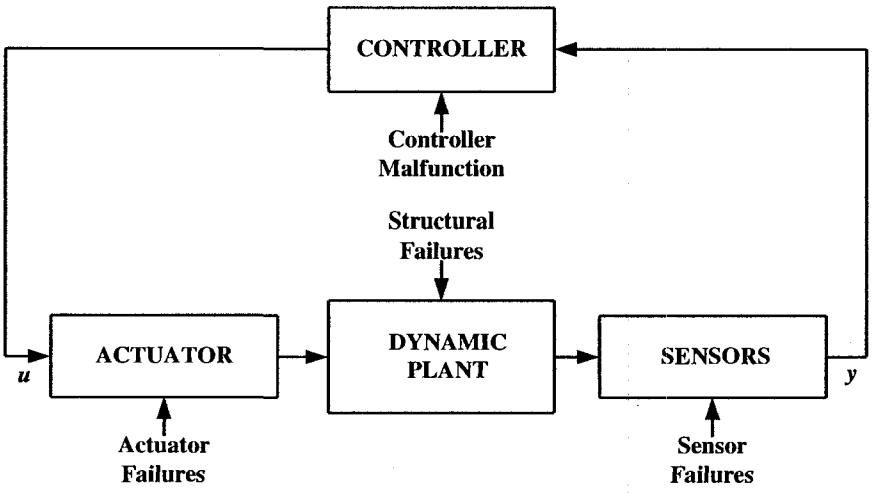

Figure 2.1. Possible Causes of Failures in a Controlled System.

To avoid the occurrence of these failures, an FDI system must detect and isolate the faults to allow recovery actions such as controller reconfiguration or utilization of redundant sensors and actuators. According to [67], the ideal FDI system should posses the following set of desirable characteristics:

- **Quick Detection:** The FDI system must be quick in detecting the process fault. Systems with quick detection capabilities are highly sensitive to noise and may lead to false alarms.
- **Isolability:** This is the ability of the FDI system to distinguish the location of the fault. Usually, high degree of isolability implies poorness in rejecting modeling uncertainties.
- **Robustness:** It is desirable that the FDI system be robust to various noise, uncertainties, and unmodeled dynamics.
- **Novelty identifiability:** The FDI system must classify the fault as a known fault or an unknown fault if the cause of the fault is different from the existing classes.
- **Classification error estimate:** The FDI system should provide *a priori* estimate on the classification of the error that can occur.
- **Adaptability:** Processes in general change and evolve producing variations in the operating conditions. The FDI system should be adaptable to these changes.
- **Explanation facility:** This characteristic implies that the FDI system should provide explanations on how the fault originated and propagated to the actual operating conditions.

- **Modeling requirements:** For the development of the FDI system, the modeling effort should be as minimal as possible.
- **Storage and computational requirements:** The FDI system should use algorithms that are computationally less expensive but having high capability of storing relevant information.
- **Multiple fault identifiability:** This is the ability to identify multiple faults. The FDI system should be capable of detecting single as well as multiple faults.

Designing a FDI system which satisfies all the above desirable characteristics is a complex task. There is a trade-off between quick detection time and robustness. Adaptability, multiple fault identifiability and classification error estimation generally require complex and expensive computational effort. Meanwhile, characteristics such as modeling requirements and storage computational requirements are related to reducing the computational efforts. There is a wide spectrum of FDI systems which offer different capabilities and weaknesses. For this reason, the design and implementation of the best fault diagnostic system is strongly related to the nature of the process.

2.2 Classification of Fault Diagnostic Systems

Early detection and isolation of a fault allows the application of recovery actions leading to maintaining the process operation. This is a critical issue for systems such as chemical process, nuclear plants, power distribution and unmanned systems. For the last two decades, researchers from the academic and industrial fields have been investigating and developing diverse FDI approaches for diverse systems such as networking systems [68], building systems [69] and [70] and mechanical systems [71]. Different FDI techniques ranging from analytical methods to artificial intelligence approaches can be classified into model-based and history-based methods depending on the specific method used to generate the information to be used for the health monitoring system. In this sense, based on how this information is presented, FDI systems are classified as quantitative or qualitative. According to [67], [72] and [73], FDI methods can be

classified as shown Figure 2.2.

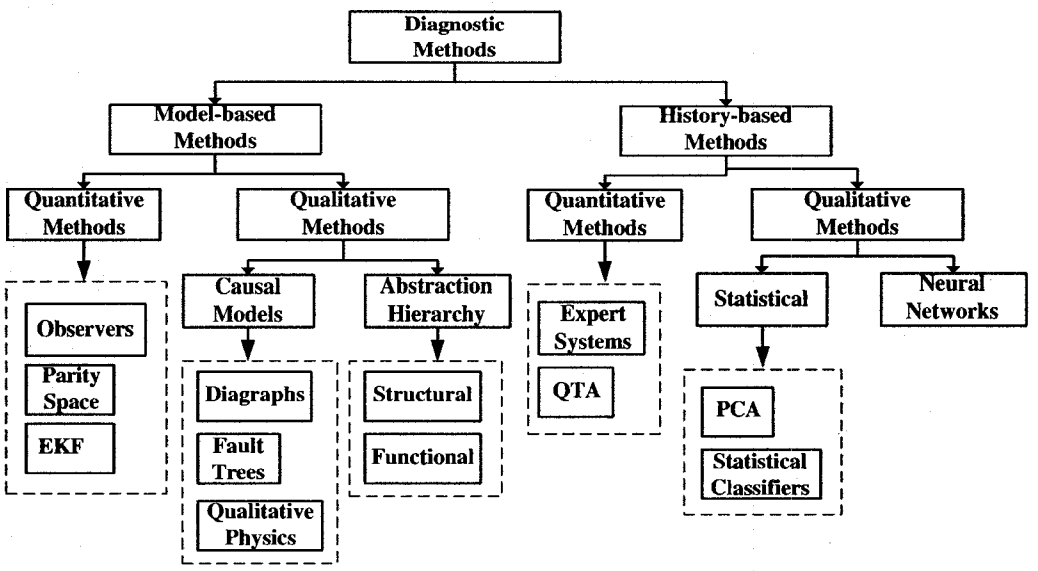

Figure 2.2. Classification of Fault Diagnostic Systems (EKF: Extended Kalman Filter, QTA: Qualitative Trend Analysis, PCA: Principal Component Analysis).

Both model-based and history-based methods need as basic *a priori* knowledge, the set of failures and the relationship between the faults and the failures. This kind of *a priori* knowledge may be developed by using model-based or history-based approaches. Model-based approaches are based on an *a priori* knowledge developed from an understanding of the process, meanwhile, history-based approaches are designed based on an *a priori* knowledge extracted from past experiences from the process. As explained in [67] and [74], this *a priori* knowledge is used to predict the behavior of a system under normal conditions and then, compare it with the actual behavior.

Model-based and history-based methods can be classified as qualitative or quantitative methods. If the *a priori* knowledge is expressed as a mathematical functional relationship between inputs and outputs, the method is classified as quantitative. On the other hand, if the relationship between faults and failures is expressed in term of qualitative functions using different units of the process, the method is considered as a qualitative method. References [67], [72] and [73] provide a complete explanation of the fault diagnostic problem including a comparative analysis of the different approaches.

2.3 Previous Work on Fault Diagnosis of Unmanned Space Vehicles for the Attitude Control Subsystem

Unmanned space vehicles are complex autonomous systems designed to perform specific missions in unforeseen environments. Traditionally, near-earth unmanned spacecraft sends periodic batch of systems data to ground stations. At ground stations, flight operations team (FOT) analyzes the data to determine the health status of the on-board systems. When a fault is detected, several new analyses must be performed to isolate the fault. To recover the spacecraft, FOT must define recovery measures which are applied in the faulty spacecraft subsystem. This entire health monitoring and recovery process is a time-consuming task which is also very expensive, especially in the case of long-duration space missions. Generally, a continuous time communication between spacecraft and ground station is not feasible and therefore, if the manifestation of a fault occurs during one of those periods, FOT must wait until the communication is recovered to detect the fault. For deep-space missions, the situation is even worse. The influence of ground-station in on-board systems is almost nonexistent. Due to these limitations, the development of autonomous fault diagnostic approaches for on-board subsystems has been identified as a critical need for current and future space missions. In this sense, there is a special interest in developing autonomous fault diagnostic approaches for actuators of the attitude control subsystem (ACS).

References [24]-[32] proposed FDI schemes for faulty components (i.e., sensors, actuators and controllers). In [75] a hierarchical fault detection, isolation and recovery approach is developed for avionics and spacecraft applications. Fault-three synthesis and neural networks are utilized in [76] to develop a fault diagnosis approach for the RADARSAT-1 ACS. Reference [77] provides a fault detection, isolation and recovery approach for the ACS of the ESA GOCE satellite. References [78]-[82] deal with the integration, reutilization, and standardization of FDI systems used in previous missions planned by the Jet Propulsion Laboratory (JPL) and European

Space Agency (ESA).

In order to introduce the current state of the development of FDI solutions for unmanned spacecraft, in the remaining part of this section we present two recently developed fault diagnostic systems for actuators of the attitude control subsystem. The first one corresponds to a model-based fault diagnostic method and the second one is a history-based fault diagnostic method.

2.3.1 Model-based Fault Diagnostic Approach

Fault detection and isolation problem in actuators of the attitude control subsystem of an unmanned space vehicle has been investigated by the approach that is proposed in [28]. As shown in Figure 2.3, a qualitative model-based method called Fault-Tree technique is used as the engine of the proposed fault diagnostic system.

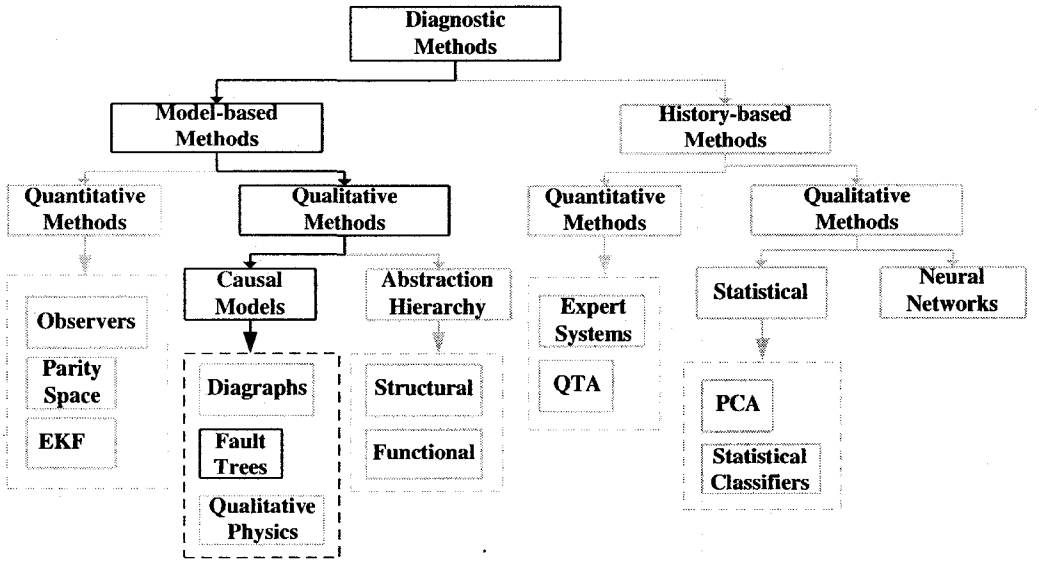

Figure 2.3. Fault-Tree Model-based Method.

Based on an existing fault detection mechanism, which could be a model-based or a history-based method, the integration of the proposed fault-tree approach allows the overall system to translate the fault symptom into a visual diagram which provides a mechanism for analyzing very complex systems. The basic structure of a fault-tree for failure analysis is shown in Figure 2.4. The basic events (BE) are fault manifestations which are the input to the fault-tree. The following

level(s) of events, called intermediate events (IE) show the propagation of the faults into the system. At the top of the fault-tree, the top event (TE) is the failure which is to be analyzed. The events at different levels are connected by logic gates.

The construction of the fault-tree proposed in [28] is a modification of the automatic process called Induction of Fault-Trees (IFT). To perform this automatic construction, a database example which includes system behaviors under faulty and healthy conditions is presented. Then, by utilizing machine learning techniques, the IFT algorithm constructs the fault-tree for failure analysis purposes. From the database example, preliminary information is extracted and labeled as attributes with specific numerical value. Finally, the correct combination of this attributes allows the system to identify different classes of failures.

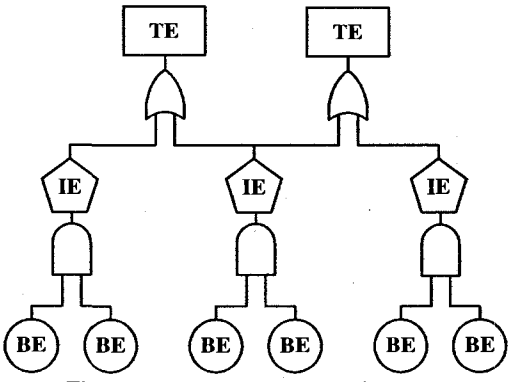

Figure 2.4. Basic Fault-Tree Structure.

A simulated ACS-model was used to generate the database for the automatic construction of the above fault-tree system. The attributes selected are: reaction wheel motor current, reaction wheel motor torque, reaction wheel speed, bus voltage input to the reaction wheel and torque command input voltage to the reaction wheel. These five variables are taken from one of the reaction wheels of the ACS. Using as maximum tolerable error, an error of 0.03° in the pitch angle, four failure scenarios were simulated. The generated output indicates if the actuator is acting under faulty or non-faulty conditions (occurrence of a TE) and gives complementary information about the attributes (value of each BE). The results establish that the proposed diagnostic approach may be applied as health monitoring and diagnosis tool for unmanned

spacecraft.

2.3.2 History-based Fault Diagnostic Approach

In [29], an actuator fault detection and isolation system for the ACS of a satellite is proposed. This FDI system uses the pattern recognition and modeling capabilities of neural networks to perform the tasks of detection and isolation. As shown in Figure 2.5, neural networks are classified as a qualitative history-based method.

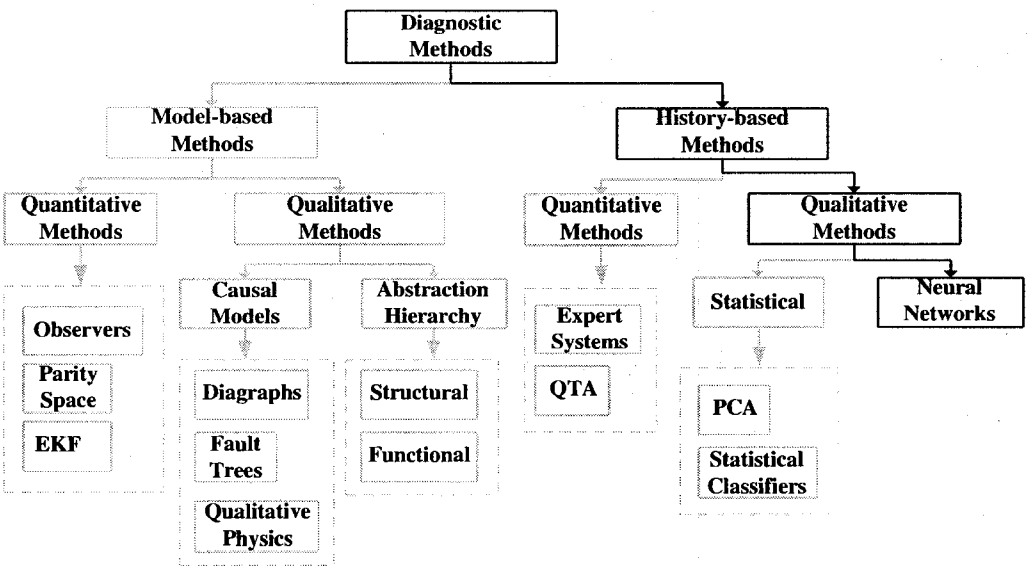

Figure 2.5. Neural Network History-based Method.

The proposed FDI system in [27] includes two different structures: a dynamic neural network for detection and a static neural network for isolation. The composition of a multilayer feedforward neural network, as shown in Figure 2.6, includes layers of neurons which are connected to the neurons of other layers. This general structure is common for both dynamic and static networks. The difference between these two networks is shown in Figure 2.7. Furthermore, the dynamic neuron includes an Infinite Impulse Response filter (IIR), whereas the static neuron does not include that filter.

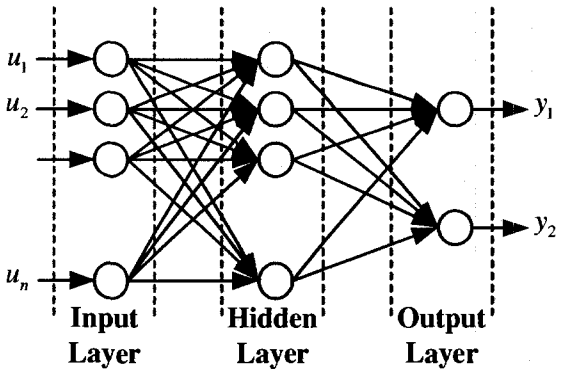

Figure 2.6. Multilayer Feedforward Neural Network.

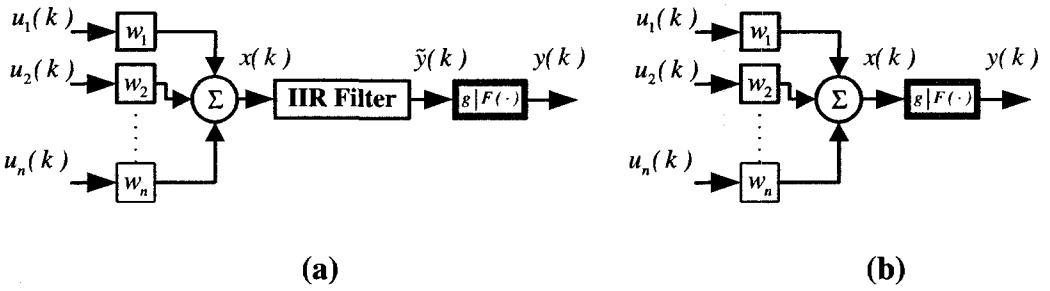

Figure 2.7. (a) Dynamic Neuron Model, (b) Static Neuron Model.

The above structural difference produces differences in the capabilities and complexity between the two networks. In the case of a dynamic neuron model, the internal filter injects internal dynamics to the overall activity of the neuron making the construction of a dynamic network capable of modeling the dynamic behavior of the process possible. The output of the dynamic neural network is used as dynamic model of the process and, by comparing the actual process output with the estimated output produced by the dynamic neural network, residual signals are generated. Finally, if the residuals exceed pre-defined threshold values, then the FDI system considers that the actuator is operating under faulty conditions. On the other hand, a static neural network cannot model the dynamics process but can be used for static classification. Therefore, static neural networks are responsible for isolating of the faults. The residuals generated with the dynamic neural network are used as inputs to the static neural network which, according to the value of the residual, associate the faulty data with a corresponding fault class which must be previously defined. Figure 2.8 shows the general structure of the proposed FDI system.

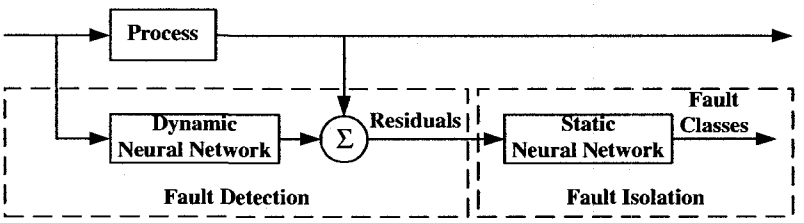

Figure 2.8. General Structure of an FDI System.

Using a simulated ACS-model, healthy and faulty data set from a reaction wheel actuator was generated. Part of the healthy data set was used to train the networks and the rest of the healthy data set was used to validate the FDI system. The faulty data set includes data corresponding to different fault scenarios and was used to evaluate the performance of the FDI system. The results showed that faults due to malfunctions in the reaction wheel actuator may be detected and isolated using this history-based fault diagnostic method.

Reference [28] proposed a reliable failure classification system based on the fault-tree method and [29] proposed a fault detection and isolation system based on neural networks. Both methods were tested with data extracted from a reaction wheel actuator of a simulated attitude control subsystem of a satellite. In the case of the fault-tree approach, the failure classification is achieved for attitude errors in the pitch angle of 0.03° or greater but the system was not designed to detect faults. This goal must be achieved by another system. On the other hand, the neural network approach is capable of detecting and isolating faults in the mechanical and electrical system of a reaction wheel actuator. The neural network based FDI system was validated for different faulty scenarios where the magnitude of the faults were significantly bigger than the magnitude used in the fault-tree approach (deviations equal or above 44.3 % from the healthy value of the signal). Another comparative aspect is that fault-tree approach uses 5 attributes (or variable) of the ACS with sampling time of the order of magnitude of seconds, whereas neural networks approach uses only 2 attributes and with a sampling time of milliseconds.

Although both methods show interesting capabilities, there are still issues that have not been covered and addressed. Development of an FDI system for other complex actuators such as

micro-thrusters is still a pending task. This kind of actuators is replacing traditional reaction wheels in almost all the latest and the important missions such as formation-flying missions. Deep space formation-flying missions (ST-3, TPF, LISA, DARWIN [14]-[16]) and near-earth formation-flying missions (EO-1, ION-F, PRISMA, CLS3, SMART-2 [16]-[23]) include precise micro-thrusters as actuators for the attitude control subsystem of the spacecraft in the formation.

2.4 Conclusions

In this chapter, concepts such as Fault, Failure, Detection and Isolation have been provided. The necessity of fault detection and isolation (FDI) systems for critical controlled processes has been clearly established. Based on the nature of the process, the FDI systems must fulfill certain specific objectives. A set of desirable characteristics for an ideal FDI system is provided and explained.

From the point of view of process engineering, FDI approaches can be divided into two classes: model-based and history-based approaches and, each of these classes is subdivided into quantitative and qualitative techniques. A list of FDI systems for different processes such as networking, building and mechanical systems are presented.

Development of FDI systems for airspace systems (i.e., aircraft and spacecraft) with special interest in unmanned spacecraft attitude control subsystem (ACS) is addressed. Previous efforts in developing FDI systems for actuators, sensors and fault tolerant and reconfigurable controllers are provided. To demonstrate the actual stage of development of FDI systems for ACS of spacecraft, two previously proposed FDI approaches (a model-based and a history-based approaches) are presented and explained.

Finally, motivated by the introduction of precise formation flying missions with micro-thrusters as actuators, the necessity of FDI systems is established. These types of missions are expensive unmanned space missions where early fault detection is a key issue that has not been completely investigated. The intention of this chapter is to demonstrate that FDI systems for

actuators in the ACS of spacecraft, especially in formation-flying missions, are extremely important and research efforts in this field are needed.

Chapter 3

Formation Flying and Attitude Control Subsystem of Satellites

3.1 Fundamentals

A group of coordinated small-size spacecraft can perform the same mission as a large spacecraft but with reduced mission cost ([1]-[13]). The small spacecraft can be grouped as a formation or as a constellation. According to [83], a formation is defined as "two or more spacecraft that use an active control scheme to maintain the relative positions of the spacecraft". On the other hand, a constellation is defined as "two or more spacecraft with no active control by either to maintain a relative position".

In this chapter, we present different formation-flying control schemes and define the formation-flying attitude control subsystem used to evaluate our fault diagnosis system. The concept of coordinate systems is explained to facilitate the understanding of the attitude representation of a single and multiple spacecraft. Control laws for the spacecraft in the formation and a brief description of sensors and actuators involved in the ACS is presented. Finally, we present a one dimensional model of a Parallel-Plates Pulsed-Plasma Thruster (PPT) which is the actuator used by the spacecraft to perform attitude correction maneuvers. Configuration details and number of actuators per spacecraft is explained at the end of the chapter.

3.2 Spacecraft Attitude Representation

Calculation of position and velocity of a spacecraft depends on its reference coordinate system. In this section we present four Coordinate Systems (CS) and three Attitude Representation Techniques (ART) most commonly used in the aerospace attitude control field.

3.2.1 Coordinate Systems

The representation of any rigid body in space depends on the selection of the reference location. A spacecraft orbiting the Earth can generally be represented in one of the following four coordinate systems:

Earth Centred Inertial (ECI): This CS has its origin in the center of the Earth. The x-axis points to the vernal equinox in the equatorial plane, the z-axis points in direction to the North Pole of the Earth, parallel to the rotation axis of the Earth, and the y-axis is perpendicular to the x-axis and the z-axis (right-handed rule). Figure 3.1 shows the axes of the Earth Centered Inertial (ECI) frame.

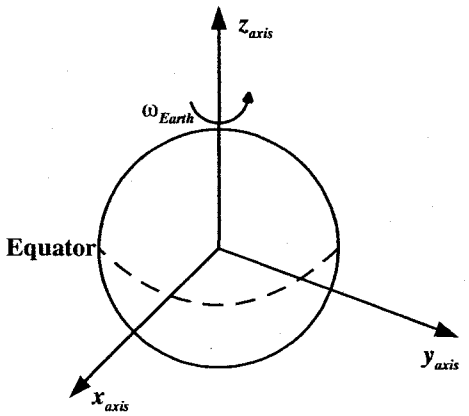

Figure 3.1. Earth Centered Inertial (ECI) Frame.

Earth Centered Earth Fixed (ECF): Similar to ECI, ECF coordinate system has its origin in the center of the Earth, but rotates with it. The x-axis points to the Greenwich meridian in the equatorial plane, the z-axis points to the North Pole and the y-axis completes the reference system with the right-handed rule. This CS is shown in Figure 3.2.

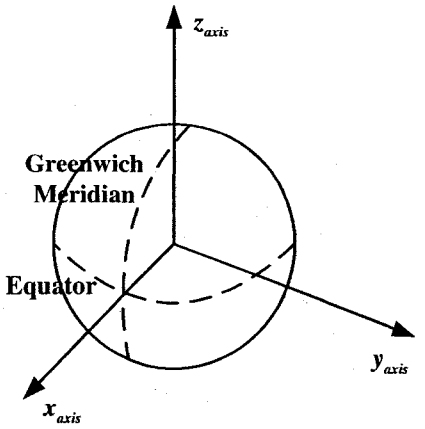

Figure 3.2. Earth Centered Earth Fixed (ECF) Frame.

Satellite Body Fixed: In this reference frame, the origin is in the center of mass (CoM) of the satellite (body) and the axes (x-axis, y-axis and z-axis) correspond to the principal axes of the satellite. This coordinate system is mainly used for attitude calculations and to describe relative positions and directions of the satellite. Figure 3.3 shows the system axes.

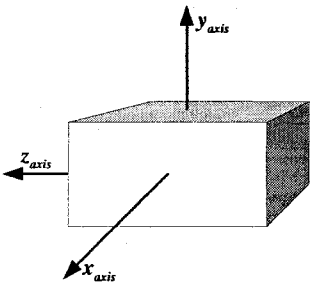

Figure 3.3. Satellite Body Fixed Frame.

Orbit References: This CS describes the desired satellite attitude in its orbit. Generally, this system is used for attitude control purposes and is a Nadir pointing system. The axes frame is shown in Figure 3.4.

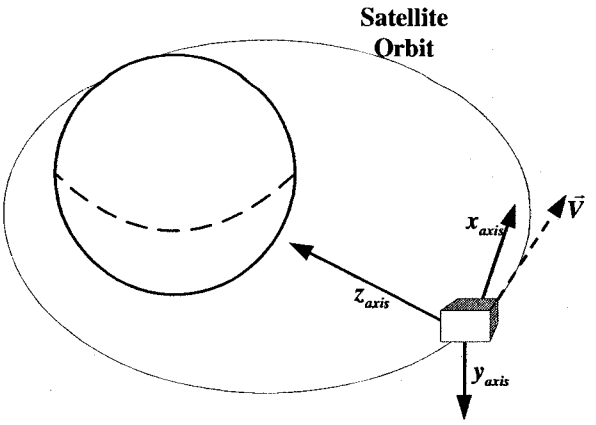

Figure 3.4. Orbit Reference Frame (Nadir pointing frame).

3.2.2 Attitude Representation

In Section 3.2.1 we defined the different coordinate systems. In this section we present the three choices for the attitude representation. The spacecraft attitude representation with respect to a reference frame may be calculated using any of the following representation techniques:

Euler Angles: This representation uses the deviation angles with respect to a reference frame. Usually, the angles are given as roll angle φ, pitch angle θ and yaw angle ψ about the Satellite Body Fixed CS. The change of the spacecraft's attitude from an initial attitude to a final attitude is represented as a sequence of three rotations. The most common sequence of rotations is defined by a first rotation about z-axis (yaw angle), a second rotation about y-axis (pitch angle) and a final rotation about x-axis (roll angle). Equation (3.1) represents the transformation of a vector in an initial reference frame $(x, y, z)^T$ to a new vector $(x^b, y^b, z^b)^T$ in the Satellite Body Fixed CS.

$$\begin{pmatrix} x^b \\ y^b \\ z^b \end{pmatrix} = \begin{pmatrix} 1 & 0 & 0 \\ 0 & \cos\varphi & \sin\varphi \\ 0 & -\sin\varphi & \cos\varphi \end{pmatrix} \begin{pmatrix} \cos\theta & 0 & -\sin\theta \\ 0 & 1 & 0 \\ \sin\theta & 0 & \cos\theta \end{pmatrix} \begin{pmatrix} \cos\psi & \sin\psi & 0 \\ -\sin\psi & \cos\psi & 0 \\ 0 & 0 & 1 \end{pmatrix} \cdot \begin{pmatrix} x \\ y \\ z \end{pmatrix} \tag{3.1}$$

Due to the use of trigonometric functions, the Euler Angles technique presents a non desirable singularity for $\theta = 90$ degree.

Direction Cosine Matrix (DCM): Another transformation of reference system can be achieved by using the Direction Cosine Matrix (DCM). For the same sequence of rotations of the Euler Angles, the transformation is expressed as follows:

$$\begin{pmatrix} x^b \\ y^b \\ z^b \end{pmatrix} = \mathrm{DCM} \cdot \begin{pmatrix} x \\ y \\ z \end{pmatrix}$$
$$\mathrm{DCM} := \begin{pmatrix} \mathrm{DCM}(1,1) & \mathrm{DCM}(1,2) & \mathrm{DCM}(1,3) \\ \mathrm{DCM}(2,1) & \mathrm{DCM}(2,2) & \mathrm{DCM}(2,3) \\ \mathrm{DCM}(3,1) & \mathrm{DCM}(3,2) & \mathrm{DCM}(3,3) \end{pmatrix} \tag{3.2}$$

where the DCM matrix is composed by the following elements:

$$\mathrm{DCM} = \begin{pmatrix} \cos\theta\cos\psi & \cos\theta\sin\psi & -\sin\theta \\ \sin\varphi\sin\theta\cos\psi - \cos\theta\sin\psi & \sin\varphi\sin\theta\sin\psi + \cos\theta\cos\psi & \sin\varphi\cos\theta \\ \cos\varphi\sin\theta\cos\psi + \sin\varphi\sin\psi & \cos\varphi\sin\theta\sin\psi - \sin\varphi\cos\psi & \cos\varphi\cos\theta \end{pmatrix} \tag{3.3}$$

The columns of the DCM shown in Equations (3.2) and (3.3) represent the unit vectors of the reference frames expressed in the target CS meanwhile the rows of the DCM give the target basis vector expressed in the reference frame. Euler angles can be calculated based on the DCM by using the mathematical relationship shown in Equation (3.4), namely

$$\begin{aligned} \varphi &= \arctan\left(\frac{\mathrm{DCM}(2,3)}{\mathrm{DCM}(3,3)}\right) \\ \theta &= \arctan\left(-\mathrm{DCM}(1,3)\right) \\ \psi &= \arctan\left(\frac{\mathrm{DCM}(1,2)}{\mathrm{DCM}(1,1)}\right) \end{aligned} \tag{3.4}$$

As far as DCM is concerned, sequential transformation requires more computation and is therefore computationally more expensive than Euler angles technique.

Quaternion: This attitude representation requires four elements (a scalar q_0 plus a vector $[q_1, q_2, q_3]^T$). The vector represents an axis rotation and the scalar defines the magnitude of the rotation. The quaternion elements represented by the Equation (3.5) hold the constraint of being a unity vector as described by Equation (3.6), namely

$$\underline{q} = \begin{pmatrix} q_0 \\ \bar{q} \end{pmatrix} = \begin{pmatrix} q_0 \\ q_1 \\ q_2 \\ q_3 \end{pmatrix} = \begin{pmatrix} cos(\mu/2) \\ m_1 \cdot sin(\mu/2) \\ m_2 \cdot sin(\mu/2) \\ m_3 \cdot sin(\mu/2) \end{pmatrix} \tag{3.5}$$

$$\underline{q}^T \underline{q} = q_0^2 + q_1^2 + q_2^2 + q_3^2 = 1 \tag{3.6}$$

where μ represent the rotation angle and m_1, m_2 and m_3 represent the rotation axis. The transformation from one initial CS (Satellite Body Fixed) to a target CS (Orbit Reference) can be done by using Equation (3.7) which represents the calculation of two consecutive rotations. This expression shows a reduction from 27 multiplications in the case of DCM to 16 multiplications using quaternion elements implying that the computational effort is reduced.

$$\begin{aligned} {}^o_b\underline{q} &= \left[{}^o_i\underline{q} \right] {}^i_b\underline{q} \\ \begin{pmatrix} {}^o_bq_0 \\ {}^o_bq_1 \\ {}^o_bq_2 \\ {}^o_bq_3 \end{pmatrix} &= \begin{pmatrix} {}^o_iq_0 & -{}^o_iq_1 & -{}^o_iq_2 & -{}^o_iq_3 \\ {}^o_iq_1 & {}^o_iq_0 & {}^o_iq_3 & -{}^o_iq_2 \\ {}^o_iq_2 & -{}^o_iq_3 & {}^o_iq_0 & {}^o_iq_1 \\ {}^o_iq_3 & {}^o_iq_2 & -{}^o_iq_1 & {}^o_iq_0 \end{pmatrix} \begin{pmatrix} {}^i_bq_0 \\ {}^i_bq_1 \\ {}^i_bq_2 \\ {}^i_bq_3 \end{pmatrix} \end{aligned} \tag{3.7}$$

where subscript b and superscript o imply Body Fixed and Orbit CS respectively. The calculation of the DCM from quaternion elements can be done with the Equation (3.8) in which $\mathbf{1}$ denotes the identity matrix and $\bar{\mathbf{q}}$ is the skew-symmetric matrix shown in Equation (3.9),

$$\text{DCM} = \left(2q_0^2 - 1\right)\mathbf{1}_{3x3} + 2 \cdot \left(\bar{\bar{q}}\bar{q}^T - q_0\bar{\mathbf{q}} \right) \tag{3.8}$$

$$\bar{\mathbf{q}} = \begin{pmatrix} 0 & -q_3 & q_2 \\ q_3 & 0 & -q_1 \\ -q_2 & q_1 & 0 \end{pmatrix} \tag{3.9}$$

Quaternion technique uses algebraic relations whereas Euler angles use trigonometric functions. This characteristic of quaternion technique allows one to avoid the singularities that may occur in the Euler angles technique.

3.3 Equations of Motion

The equations of motion that describe the rotational dynamics of a spacecraft are generated by a set of nonlinear equations. These equations may be classified as dynamic and kinematic equations. Here we present both sets of equations and also provide a state space model for the complete representation of the spacecraft attitude system. For more information about spacecraft's equations of motion, refer to [84] which provides a detailed discussion on this topic.

Nonlinear Dynamic Equations: The rotational movement of a spacecraft can be represented by the dynamical equation of a rigid body as shown in Equation (3.10):

$$\bar{T} = \dot{\bar{h}} + \bar{\omega} \times \bar{h} = \bar{I} \cdot \dot{\bar{\omega}} + \bar{\omega} \times \left(\bar{I} \cdot \bar{\omega} \right) \tag{3.10}$$

where $\bar{T}$ is the total torque acting on the spacecraft, $\bar{h}$ is its angular momentum, $\bar{\omega}$ is body rotational rates vector and I is the inertia matrix of the spacecraft. Using the Satellite Body Fixed CS, the inertia matrix is constant. By assuming that the body (spacecraft) is symmetric about the center of gravity, all the cross products of inertia (off diagonal elements) are zero and the inertia matrix becomes:

$$I = \begin{pmatrix} I_x & 0 & 0 \\ 0 & I_y & 0 \\ 0 & 0 & I_z \end{pmatrix} \tag{3.11}$$

Now, rearranging the elements of Equation (3.10) and substituting the expression of Equation (3.11), we can express the rotational dynamic equation as the set of body component equations as shown in Equation (3.12), namely

$$
\begin{aligned}
{}^{b}\dot{\omega}_x &= \frac{{}^{b}T_x}{I_x} + \frac{I_y - I_z}{I_x}\,{}^{b}\omega_y\,{}^{b}\omega_z \\
{}^{b}\dot{\omega}_y &= \frac{{}^{b}T_y}{I_y} + \frac{I_z - I_x}{I_y}\,{}^{b}\omega_z\,{}^{b}\omega_x \\
{}^{b}\dot{\omega}_z &= \frac{{}^{b}T_z}{I_z} + \frac{I_x - I_y}{I_z}\,{}^{b}\omega_x\,{}^{b}\omega_y
\end{aligned}
\tag{3.12}
$$

where the superscript '*b*' indicates the satellite body fixed CS.

Nonlinear Kinematic Equations: The kinematic equations of the spacecraft are represented by using the quaternion attitude representation technique. As the kinematics attitude are linear in the quaternion and rates, Equations (3.13) and (3.14) can represent the kinematics of the spacecraft, that is

$$
\underline{\dot{q}} = \frac{1}{2}\begin{pmatrix} 0 & -\omega_x & -\omega_y & -\omega_z \\ \omega_x & 0 & \omega_z & -\omega_y \\ \omega_y & -\omega_z & 0 & \omega_x \\ \omega_z & \omega_y & -\omega_x & 0 \end{pmatrix}\begin{pmatrix} q_0 \\ q_1 \\ q_2 \\ q_3 \end{pmatrix} \tag{3.13}
$$

$$
\underline{\dot{q}} = \frac{1}{2}\begin{pmatrix} -q_1 & -q_2 & -q_3 \\ q_0 & -q_3 & q_2 \\ q_3 & q_0 & q_1 \\ -q_2 & q_1 & q_0 \end{pmatrix}\begin{pmatrix} \omega_x \\ \omega_y \\ \omega_z \end{pmatrix} \tag{3.14}
$$

Similar to the dynamic equations, the kinematic equations can be written as quaternion elements equations (Equation (3.15)). The superscript '*b*' indicates satellite body fixed CS and the subscript '*o*' indicates orbital reference CS.

$$
\begin{aligned}
{}^{b}_{o}\dot{q}_0 &= \frac{1}{2}\left(-{}^{b}_{o}q_1\,{}^{b}\omega_x - {}^{b}_{o}q_2\,{}^{b}\omega_y - {}^{b}_{o}q_3\,{}^{b}\omega_z\right) \\
{}^{b}_{o}\dot{q}_1 &= \frac{1}{2}\left({}^{b}_{o}q_0\,{}^{b}\omega_x - {}^{b}_{o}q_3\,{}^{b}\omega_y + {}^{b}_{o}q_2\,{}^{b}\omega_z\right) \\
{}^{b}_{o}\dot{q}_2 &= \frac{1}{2}\left({}^{b}_{o}q_3\,{}^{b}\omega_x + {}^{b}_{o}q_0\,{}^{b}\omega_y - {}^{b}_{o}q_1\,{}^{b}\omega_z\right) \\
{}^{b}_{o}\dot{q}_3 &= \frac{1}{2}\left(-{}^{b}_{o}q_2\,{}^{b}\omega_x + {}^{b}_{o}q_1\,{}^{b}\omega_y + {}^{b}_{o}q_0\,{}^{b}\omega_z\right)
\end{aligned}
\tag{3.15}
$$

The dynamic equations and kinematic equations shown in Eq. (3.12) and (3.14) respectively, allow the formulation of the following nonlinear state space model for the spacecraft's rotational movement. For the sake of simplicity, in the following equations we neglect the superscripts '*b*' and subscript '*o*' as shown before, therefore

$$
\begin{aligned}
\dot{\vec{x}} &= f(\vec{x}) + g\left(\vec{x}\right)\vec{u} \\
\vec{y} &= \vec{x}
\end{aligned}
\tag{3.16}
$$

where the state, control and output vectors are $\vec{x} = \left[\omega_x \omega_y \omega_z\, q_0\, q_1\, q_2\, q_3\right]^T$, $\vec{u} = \left[T_x T_y T_z\right]^T$ and $\vec{y} = \left[\omega_x \omega_y \omega_z\, q_0\, q_1\, q_2\, q_3\right]^T$, respectively. The elements of the state vector ω_x, ω_y and ω_z are the angular velocity of the CoM of the spacecraft with respect to the *x*-axis, *y*-axis and *z*-axis, respectively, q_0 is the magnitude of the spacecraft rotation and q_1, q_2 and q_3 are the angle rotations about the *x*-axis, *y*-axis and *z*-axis, respectively. The elements of the control vector T_x, T_y and T_z are the total torque that is applied about the *x*-axis, *y*-axis and *z*-axis of the CoM of the spacecraft, respectively. The representation for $f(\cdot)$ and $g(\cdot)$ are shown in Equations (3.17) and (3.18), respectively.

$$f(\bar{x}) = \begin{pmatrix} \frac{I_y - I_z}{I_x}\omega_y\omega_z \\ \frac{I_z - I_x}{I_y}\omega_z\omega_x \\ \frac{I_x - I_y}{I_z}\omega_x\omega_y \\ \frac{1}{2}\left(-q_1\omega_x - q_2\omega_y - q_3\omega_z\right) \\ \frac{1}{2}\left(q_0\omega_x - q_3\omega_y + q_2\omega_z\right) \\ \frac{1}{2}\left(q_3\omega_x + q_0\omega_y - q_1\omega_z\right) \\ \frac{1}{2}\left(-q_2\omega_x + q_1\omega_y + q_0\omega_z\right) \end{pmatrix} \tag{3.17}$$

$$g(\bar{x}) = \begin{pmatrix} \frac{1}{I_x} & 0 & 0 \\ 0 & \frac{1}{I_y} & 0 \\ 0 & 0 & \frac{1}{I_z} \\ 0 & 0 & 0 \\ 0 & 0 & 0 \\ 0 & 0 & 0 \\ 0 & 0 & 0 \end{pmatrix} \tag{3.18}$$

Equations (3.16) to (3.18) are used to represent the dynamics and the kinematics of each spacecraft in the formation flying system as described next.

3.4 Formation Flying of Multiple Spacecraft

In Section 3.1 we provided basic definitions of formation and constellation of spacecraft. From the control point of view, formation of spacecraft is a more complex problem with at least two spacecraft. Figure 3.5 shows a typical formation of three spacecraft in a near Earth orbit that is used as an experimental formation of spacecraft. In this section we present the principal aspects

of formation flying missions and define the specifications for our hypothetical system to be implemented.

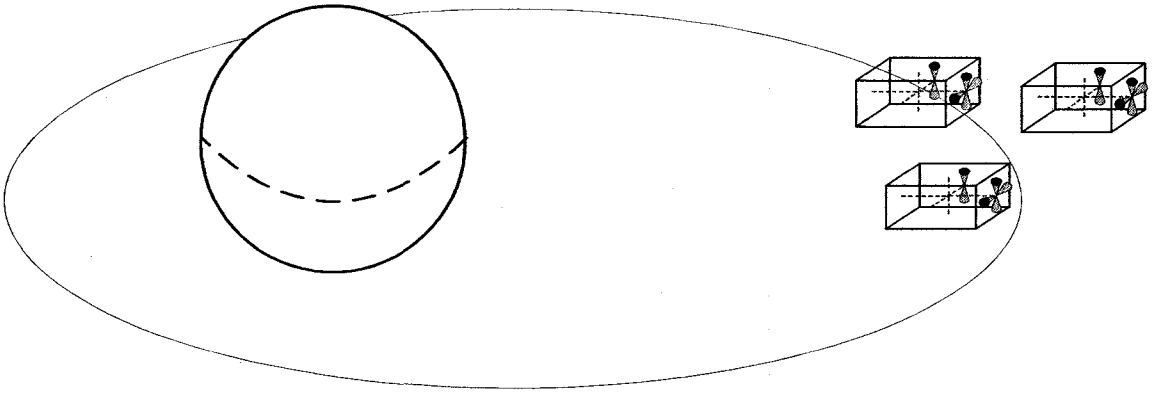

Figure 3.5. Formation of Three Spacecraft Flying in a Near Earth Orbit.

3.4.1 Formation Flying Control Architectures

According to [62] in a formation of spacecraft at least two of them use an active control scheme to maintain the relative positions. An alternative definition is provided in [85] where formation flying is defined as a set of more than one spacecraft in which any of the spacecraft dynamic states are coupled through a common control law. This definition is complemented with two conditions: at least one spacecraft of the formation must (i) track a desired state profile relative to another member, and (ii) the associated control law must at minimum depend upon the state of this other member. The above active control scheme or common control law can be understood as the formation flying control. Literature gives five formation flying control architectures ([83] and [85]) which can be defined as follows:

- **Leader/Follower:** In this architecture, one of the spacecraft is designed as the leader and the rest are the followers. The leader control system used absolute measurements to perform its maneuvers meanwhile the followers used relative measurements. Each follower has individual controllers that are connected hierarchically with the leader reducing the formation flying control to individual tracking controllers. Informally speaking, followers must change their

position and attitude based on the position and attitude of the leader. This architecture is also called Master/Slave, Chief/Deputy or Target/Chase

- **Virtual Structures:** The formation of spacecraft is thought as a large virtual structure in which each spacecraft is a rigid body embedded within it. The control of the formation attempts to ensure that the "virtual structure" follows the reference as a single body.
- **Multi-Input/Multi-output:** The formation is treated as a single multi-input multi-output system. The difference between this architecture and the virtual structure architecture is that there is a reference for the states of each spacecraft in the formation.
- **Cyclic:** This architecture is similar to the leader/follower architecture in the sense that there is an individual controller for each spacecraft but it is different in the sense that they are not in a hierarchical arrangement. Each spacecraft controls its motion with respect to its neighbors not with respect to the leader spacecraft.
- **Behavioral:** In this architecture, each spacecraft is designed to have individual performance objectives and different behaviors. The outputs of multiple spacecraft controllers are then combined to generate a control signal which considers the behavioral difference among the spacecraft.

The leader/follower architecture is among the most common formation flying configurations. For this reason the control architecture considered to be implemented for the formation flying will be the leader/follower scheme.

3.4.2 Formation Flying Architecture and the Attitude Control Subsystem (ACS) Design

In our formation flying system, the leader/follower architecture is composed of three spacecraft. One spacecraft is designed as the "Leader" (s/c_l) and the other two spacecraft are the "Followers" (s/c_{f1}) and (s/c_{f2}). Based on the definition of the leader/follower architecture (Section 3.4.1), s/c_{f1}

and s/c_{f2} have individual controllers which are hierarchically interfaced to the s/c_l. The followers receive the attitude coordinates of the leader and according to a previously defined reference, s/c_{f1} and s/c_{f2} correct their own attitude. For the attitude control point of view s/c_l can be considered as a single spacecraft. Therefore, the ACS of the s/c_l is operating with the absolute attitude measurements. On the other hand, the s/c_{f1} and s/c_{f2} correct their attitude relative to the leader's attitude and as result the ACS of the s/c_{f1} and s/c_{f2} operate with relative attitude measurements (i. e. relative to the leader's attitude).

Attitude controllers receive from the sensors the actual spacecraft's absolute (or relative) attitude measurements and then utilize them to calculate the deviations from a desired absolute (or relative) attitude. This would be translated into commands for the actuators to provide the required torques to perform absolute (or relative) attitude correction actions. There are various types of attitude controllers such as linear, quadratic, bang-bang, neural networks controllers, among others. Linear and nonlinear approaches have also been implemented for different missions. References [85]-[92] give some examples related to the controller design.

According to [84], the attitude control subsystem may be divided into two operational phases: Rate Control and Attitude Acquisition and Stabilization. Rate Control is required when the spacecraft is acting under any one of the following two scenarios: (i) after separation of the launcher vehicle, and (ii) when the attitude control subsystem of the spacecraft is re-activated after an unplanned shutdown. The objective is to reduce the angular velocities about the three-axes of the spacecraft's body prior to the activation of the Attitude Acquisition and Stabilization Controller which is used to perform angular rotations.

3.4.2.1 Controller Design

The Attitude Acquisition and Stabilization Controller commands the rotation of the spacecraft to a desired attitude and stabilizes the spacecraft in that reference attitude. Due to its simplicity and robustness, it was decided to implement a Quaternion Error Vector Command Law [84] for all the

spacecraft in the formation. First, we present the details on the design of the Quaternion Error Vector Command Law for the s/c_l and then comment on the required modifications necessary for the s/c_{f1} and s/c_{f2}.

Quaternion Error Vector Command Law for the s/c_l: The control law is a linear scheme which uses feedback from the attitude error quaternion as well as the angular velocity errors for the three-axes of the spacecraft's body. The maximum deviation from the reference attitude, expressed in the form of maximum Euler angles, may be transformed into the quaternion representation according to the following relationship:

$$ {}^{leader}\underline{q}_{max} = \begin{pmatrix} {}^{leader}q_{max,0} \\ {}^{leader}q_{max,1} \\ {}^{leader}q_{max,2} \\ {}^{leader}q_{max,3} \end{pmatrix} = \begin{pmatrix} 1 \\ {}^{leader}\varphi_{max}/2 \\ {}^{leader}\theta_{max}/2 \\ {}^{leader}\psi_{max}/2 \end{pmatrix} \tag{3.19} $$

Equation (3.19) is valid if all the angles are considered to be approximately smaller than 10 degrees. Based on the maximum Euler angles, we can calculate the maximum angular velocity ${}^{leader}\Delta\omega_{max} = [{}^{leader}\Delta\omega_{max,x} \; {}^{leader}\Delta\omega_{max,y} \; {}^{leader}\Delta\omega_{max,z}]^T$. On the other hand, in order to save resources, we want to avoid jitter around the equilibrium attitude. To fulfill this desirable condition we define a minimum angular velocity ${}^{leader}\Delta\omega_{min} = [{}^{leader}\Delta\omega_{min,x} \; {}^{leader}\Delta\omega_{min,y} \; {}^{leader}\Delta\omega_{min,z}]^T$. The construction of the controller is based now on the linear representation of the state space model as shown in Equation (3.16) and the linear control law becomes:

$$ {}^{leader}\overline{T}_{com} = -\begin{pmatrix} {}^{1}\mathbf{K_d} & 2{}^{1}\mathbf{K_p} \end{pmatrix} \begin{pmatrix} {}^{leader}\Delta\overline{\omega} \\ {}^{leader}\overline{q}_E \end{pmatrix} \tag{3.20} $$

where ${}^{leader}\overline{T}_{com}$ is the commanded torque vector, ${}^{leader}\Delta\overline{\omega}$ is the rotational rates vector with respect to the satellite body fixed CS and ${}^{leader}\overline{q}_E$ is the error quaternion vector. Using Lyapunov theory, the author in [85] analyzes the stability of this control law. The system is asymptotically stable if ${}^{1}\mathbf{K_d}$ and ${}^{1}\mathbf{K_p}$ are diagonal gain matrices as the one shown in Equation (3.21) and hold the

conditions given by Equation (3.22).

$$ {}^{l}\mathbf{K_d} = \begin{pmatrix} {}^{l}k_{d,x} & 0 & 0 \\ 0 & {}^{l}k_{d,y} & 0 \\ 0 & 0 & {}^{l}k_{d,z} \end{pmatrix}; \quad {}^{l}\mathbf{K_p} = \begin{pmatrix} {}^{l}k_{p,x} & 0 & 0 \\ 0 & {}^{l}k_{p,y} & 0 \\ 0 & 0 & {}^{l}k_{p,z} \end{pmatrix} \tag{3.21} $$

$$ \begin{aligned} \frac{\left|{}^{leader}T_{sys,i}\right|}{{}^{leader}\Delta\omega_{max,i}} \le {}^{l}k_{d,i} \le \frac{\left|{}^{leader}T_{sys,i}\right|}{{}^{leader}\Delta\omega_{min,i}} \\ {}^{l}k_{p,i} \ge \frac{\left|{}^{leader}T_{sys,i}\right|}{2\,{}^{leader}q_{max,0}\;{}^{leader}q_{max,i}} \end{aligned} \tag{3.22} $$

where ${}^{leader}T_{sys,i}$ is the producible torque in the direction of the *i-th* axis. Finally, in order to avoid the activation of the actuators for small values of ${}^{leader}T_{com,i}$, it is desirable to include a deadband (Equation (3.23)), namely

$$ {}^{leader}T_{com,i} = \begin{cases} {}^{leader}T_{com,i}; & \left|{}^{leader}T_{com,i}\right| \ge \left|{}^{leader}T_{sys,i}\right| / {}^{leader}k_{deadband,i} \\ 0; & \left|{}^{leader}T_{com,i}\right| < \left|{}^{leader}T_{sys,i}\right| / {}^{leader}k_{deadband,i} \end{cases} \tag{3.23} $$

where ${}^{leader}k_{deadband,i}$ is a positive gain which value depends on the producible torque in direction of the *i-th* axis.

Quaternion Error Vector Command Law for the s/c_{f1} and s/c_{f2}: The controller's design for the followers s/c_{f1} and s/c_{f2} is exactly the same as that of the above design for the s/c_l. The only difference is related to the measurements (angles and angular velocities) applied to the controller. In this case, angles and angular velocities are relative to the s/c_l attitude. In the following equations, the index *j* is used to identify the *j-th* follower spacecraft while the index *i* is used to identify the *i-th* axis. The maximum deviation from the reference attitude (s/c_l attitude), is expressed as follows:

$$ {}^{follower,j}_{leader}\underline{q}_{max} = \begin{pmatrix} {}^{follower,j}_{leader}q_{max,0} \\ {}^{follower,j}_{leader}q_{max,1} \\ {}^{follower,j}_{leader}q_{max,2} \\ {}^{follower,j}_{leader}q_{max,3} \end{pmatrix} = \begin{pmatrix} 1 \\ {}^{follower,j}_{leader}\varphi_{max}/2 \\ {}^{follower,j}_{leader}\theta_{max}/2 \\ {}^{follower,j}_{leader}\psi_{max}/2 \end{pmatrix} \tag{3.24} $$

The maximum angular velocity $\Delta\omega_{max}$ and the minimum angular velocity $\Delta\omega_{min}$ are represented in Equations (3.25) and (3.26), respectively, according to

$$ {}^{follower,j}_{leader}\Delta\omega_{max} = \left[{}^{follower,j}_{leader}\Delta\omega_{max,x} \quad {}^{follower,j}_{leader}\Delta\omega_{max,y} \quad {}^{follower,j}_{leader}\Delta\omega_{max,z} \right]^T \tag{3.25} $$

$$ {}^{follower,j}_{leader}\Delta\omega_{min} = \left[{}^{follower,j}_{leader}\Delta\omega_{min,x} \quad {}^{follower,j}_{leader}\Delta\omega_{min,y} \quad {}^{follower,j}_{leader}\Delta\omega_{min,z} \right]^T \tag{3.26} $$

Equation (3.20) is rewritten so that the control law becomes:

$$ {}^{follower,j}_{leader}\bar{T}_{com} = -\left({}^{l,j}\mathbf{K_d} \quad 2\,{}^{l,j}\mathbf{K_p} \right) \begin{pmatrix} {}^{follower,j}_{leader}\Delta\bar{\omega} \\ {}^{follower,j}_{leader}\bar{q}_E \end{pmatrix} \tag{3.27} $$

where ${}^{follower,j}_{leader}\bar{T}_{com}$ is the commanded torque vector for the *j-th* follower spacecraft, ${}^{follower,j}_{leader}\Delta\bar{\omega}$ is the rotational rates vector of the s/c_{fj} with respect to the rotational rates vector of the s/c_l. The error quaternion vector with respect to the leader spacecraft is represented by ${}^{follower,j}_{leader}\bar{q}_E$.

The diagonal gain matrices $({}^{f,j}_{l}\mathbf{K_d}, {}^{f,j}_{l}\mathbf{K_p})$ and the stability conditions are shown in Equations (3.28) and (3.29) respectively, namely

$$ {}^{f,j}_{l}\mathbf{K_d} = \begin{pmatrix} {}^{f,j}_{l}k_{d,x} & 0 & 0 \\ 0 & {}^{f,j}_{l}k_{d,y} & 0 \\ 0 & 0 & {}^{f,j}_{l}k_{d,z} \end{pmatrix}; \quad {}^{f,j}_{l}\mathbf{K_p} = \begin{pmatrix} {}^{f,j}_{l}k_{p,x} & 0 & 0 \\ 0 & {}^{f,j}_{l}k_{p,y} & 0 \\ 0 & 0 & {}^{f,j}_{l}k_{p,z} \end{pmatrix} \tag{3.28} $$

$$ \begin{aligned} \frac{\left| {}^{follower,j}_{leader}T_{sys,i} \right|}{{}^{follower,j}_{leader}\Delta\omega_{max,i}} \le {}^{f,j}_{l}k_{d,i} \le \frac{\left| {}^{follower,j}_{leader}T_{sys,i} \right|}{{}^{follower,j}_{leader}\Delta\omega_{min,i}} \\ {}^{f,j}_{l}k_{p,i} \ge \frac{\left| {}^{follower,j}_{leader}T_{sys,i} \right|}{2\,{}^{follower,j}_{leader}q_{max,0}\;{}^{follower,j}_{leader}q_{max,i}} \end{aligned} \tag{3.29} $$

Finally, in order to avoid the activation of actuators for small values of ${}^{follower,j}_{leader}T_{com,i}$, it is desirable to include the deadband shown in Equation (3.30), according to

$$ {}^{follower,j}_{leader}T_{com,i} = \begin{cases} {}^{follower,j}_{leader}T_{com,i}; & \left| {}^{follower,j}_{leader}T_{com,i} \right| \ge \left| {}^{follower,j}_{leader}T_{sys,i} \right| \Big/ {}^{follower,j}_{leader}k_{deadband,i} \\ 0; & \left| {}^{follower,j}_{leader}T_{com,i} \right| < \left| {}^{follower,j}_{leader}T_{sys,i} \right| \Big/ {}^{follower,j}_{leader}k_{deadband,i} \end{cases} \tag{3.30} $$

where ${}^{follower,j}_{leader}k_{deadband,i}$ is a positive gain whose value depends on the producible torque in the direction of the *i-th* axis.

As discussed above, the Attitude and Stabilization Controller based on the Quaternion Error Vector Command Law requires measurements of angles and angular velocities for the three axes of the spacecraft.

3.5 Sensors and Control Actuators

Sensors and actuators are fundamental devices for spacecraft's stabilization. Depending on the mission requirements and environmental scenarios the spacecraft must be equipped with specific sensors and actuators. To provide the basic information about the hardware of the attitude control subsystem of a spacecraft, different types of sensors and actuators are presented bellow.

Sensors: To obtain a complete attitude determination of a spacecraft with respect to a reference system, it desirable to know angles and angular velocities of the spacecraft. The following are some of the most commonly used sensors devices.

- ***Sun Sensor:*** These devices measure the unit vector to the Sun providing coarse attitude information. They have been developed having different designs and accuracies. Sun sensors cannot be used in eclipse phases.
- ***Earth Sensor:*** Measures the unit vector to the center of the Earth. They use infrared radiation to detect the horizon of the Earth. The accuracy level of this device is in the same level of the Sun sensor but cannot be used for mission far away from Earth. Their applications are restricted to Earth orbits.
- ***Star Sensor:*** Also known as 'star tracker' is the most accurate device because it calculates the attitude position based on the position of stars. This technology requires more complex computation. Due to these characteristics, sun sensors are more expensive than Sun and Earth sensors.

- ***Magnetometer:*** These devices are simple and robusts, they measure the magnetic field vector to describe the geomagnetic field at the spacecraft position. Due to the geomagnetic field, magnetometers can only be used for low Earth orbit missions.
- ***Gyroscope:*** This sensor provides information on the rotational rates of the spacecraft in the inertial frame.

Actuators: These devices are responsible for generating the torques required to change the angular position of the spacecraft. To fully control the three axes of the spacecraft body, groups of actuators must be located in proper positions. Here we present some of the most known actuators for attitude stabilization.

- ***Wheels:*** Reaction wheels, momentum wheels and fly wheels are actuators which operate under the same operational idea but with differences in the technique used. They do not generate external torques, however they provide only internal torques by using a spinning wheel. The direction and magnitude of the angular momentum is controlled by the wheel rate which produces a rotational acceleration of the spacecraft. This popular choice of the actuator provides a high accuracy stabilization and target pointing.
- ***Magnetotorquer:*** Magnetotorquers provide external torques by using the magnetic field of the Earth. These devices create a magnetic dipole which tries to align itself with the magnetic field of the Earth. As the spacecraft moves in its orbit, the magnetic field direction changes and the attitude control system gains controllability about the three axes.
- ***Thrusters:*** There are different types and sizes of thrusters but all of them are built based on the same principle, acceleration of a propellant is used to generate a force in the direction of which the propellant is discharged. Ion Thrusters [33]-[37], Hall Thrusters [38]-[46], Colloid Thrusters [47]-[49], Magneto Plasma Dynamic (MPD) Thrusters [50]-[53], Pulsed Plasma Thrusters [54]-[63], among others [64]-[66] can be utilized for the three-axis attitude control of a spacecraft.

In our formation-flying system, the three spacecraft (s/c_l, s/c_{f1} and s/c_{f2}) need Magnetometers

and Gyroscopes sensors. Due to the Formation-flying attitude control requirements, s/c_{f1} and s/c_{f2} need to know the s/c_l attitude, therefore communication equipment such the Autonomous Formation Flying (AFF) sensor ([93]) is required. To provide the commanded torque, the three spacecraft are equipped with a system of Pulsed Plasma Thrusters (PPTs). Figure 3.6 (a) and (b) shows the complete ACS for the leader and the followers respectively.

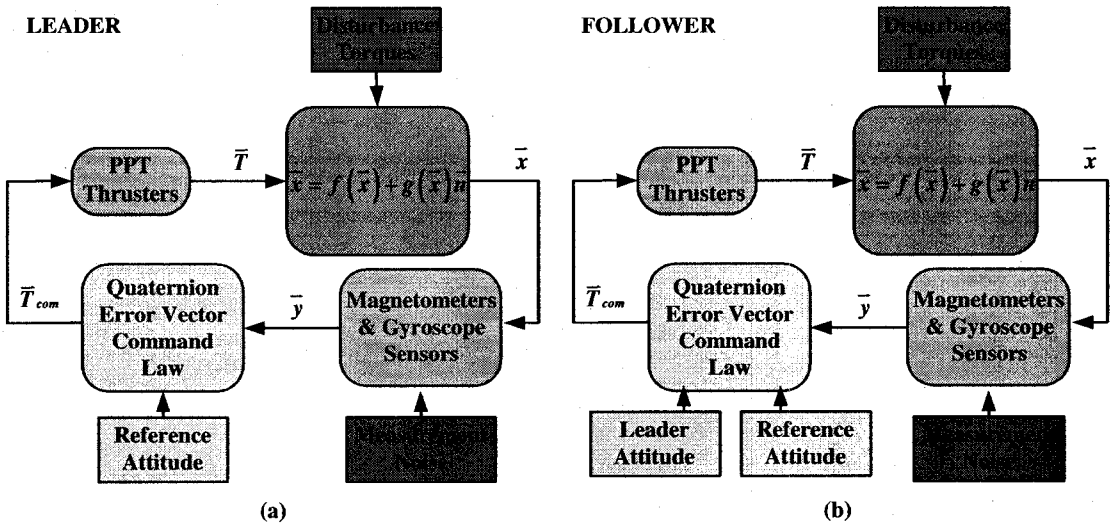

Figure 3.6. (a) Attitude Control Subsystem for a Leader Spacecraft and (b) Attitude Control Subsystem for a Follower Spacecraft.

In Chapter 2, we have indicated that a controlled system is composed of the dynamic plant, sensors, controllers and actuators, and any one of them can cause a failure. In the case of a formation flying system with a leader/follower control architecture, failures can be originated in any of the spacecraft. We study and analyze the case of malfunctions in the actuators (e.g. Pulsed Plasma Thrusters (PPTs)). In the following section, the PPT system is presented and explained in detail.

3.6 Pulsed Plasma Thrusters Actuators

As discussed in [94], a typical attitude control system for a three-axis stabilized spacecraft is accomplished by means of reaction wheels with magnetic torquers and thrusters. As an alternative to this control strategy, a Pulsed Plasma Thruster (PPT) actuator can reach the same accuracy level but at lower cost, mass and complexity. Furthermore, a PPT system can be used for different

purposes such as stationkeeping, attitude control and orbit insertion and drag make-up. Due to these reasons, in the past two decades various missions such as LES 6, LES 8/9, EO-1, TIP/NOVA and Dawgstar have been designed with PPT systems [59],[60],[62],[63] and [95]-[102].

In this section we define the operational characteristic of a PPT, present the dynamic equations which define the state space model of this specific actuator and, at the end of the section, we present the PPT's configuration required to perform maneuvers about the three axes of the spacecraft's body.

3.6.1 Pulsed Plasma Thruster (PPT)

Various types of PPTs are categorized into coaxial or parallel-plate according to the electrodes geometry, and into gas or ablative according to the propellant used. In this thesis we investigate a Parallel-Plate Ablative PPT similar to the one utilized in the Lincoln Experimental Satellite 8/9 (LES-8/9) [59], [60] and [94]. As shown in Figure 3.7, the main components are the capacitor, the electrodes, the igniter and the spring.

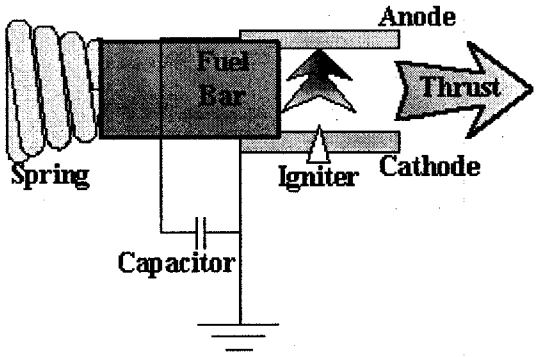

Figure 3.7. Pulsed Plasma Thruster (PPT) Schematic Diagram [111].

The physics of the PPT's pulse and the acceleration process are described as follows [94]:

- For a period of approximately 10 ms, the capacitor is charged to a maximum voltage V_{max}. The capacitor voltage appears across the electrodes (anode/cathode) of the thruster.
- The igniter, earlier charged, receives the discharge signal. This action ablates and ionizes part

of the material (e.g. Teflon) to create a conducting path which allows the discharge of the capacitor.

- The discharge current ablates and ionizes the fuel bar into a plasma slug. Due to the current that flows through this circuit, a self-magnetic field is produced.
- Finally, the plasma is accelerated by the Lorentz force ($J \times B$) due to the discharge current and the magnetic field.

The parallel plate PPT can be described as a one-diemnsional mathematical model represented by a specific type of electromechanical system (Figure 3.8).

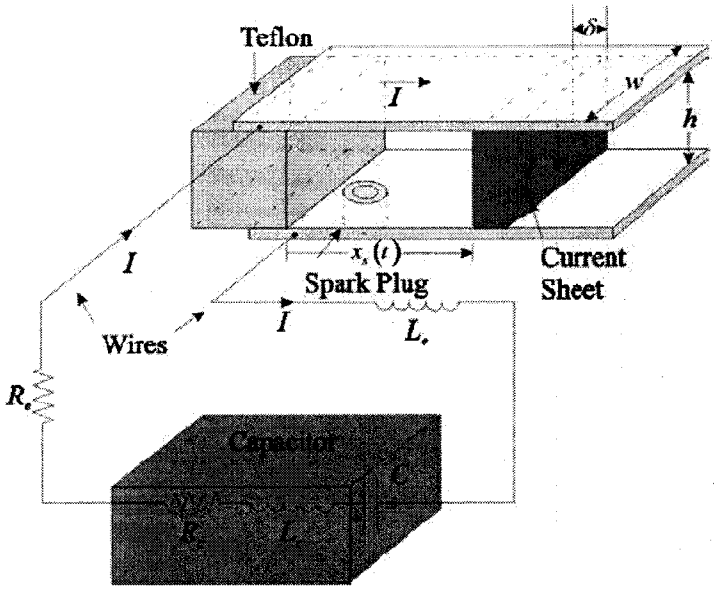

Figure 3.8. Parallel Plate PPT Components [134].

This PPT operates electrically as an LRC circuit. By assuming that the entire mass $m = m_0$ is accelerated as a single unit, m is taken as being constant throughout the process. Finally, the general parallel-plate ablative PPT thruster is described by the following system of two second order ordinary differential equations [134]:

$$
\begin{aligned}
\dot{x}_1 &= x_3 \\
\dot{x}_2 &= x_4 \\
\dot{x}_3 &= \frac{1}{2}\frac{L'_{pe}}{m_0}[x_3]^2 \\
\dot{x}_4 &= \frac{-\left(\frac{1}{C}\right)x_2 - \mu_0 \frac{h}{w} x_3 x_4 - R_T x_4 + v}{L_T}
\end{aligned}
\tag{3.31}
$$

$$
\begin{aligned}
y_1 &= m_0 x_3 f \\
y_2 &= x_4
\end{aligned}
$$

where x_1 is the position, x_2 is the capacitor charge, x_3 is the velocity and x_4 is the current, v is the capacitor voltage, y_1 is the thrust, y_2 is the discharge current, $R_T = R_c+R_e+R_{pe}+R_p$ and $L_T = L_c+L_e+L_{pe}$. Equations (3.32) and (3.33) provide expressions for R_p and $L_{pe}(t)$ respectively, and the parameters appearing in (3.31)-(3.33) are specified in Table 3.I. We furthermore assume that $x_1(0) = x_2(0) = x_3(0) = x_4(0) = 0$.

$$
R_p = 2.57\frac{h}{T_e^{\frac{3}{4}} w}\sqrt{\frac{\mu_0 \ln\left[1.24\times10^7\left(\frac{T_e^3}{n_e}\right)^{\frac{1}{2}}\right]}{\tau}} \tag{3.32}
$$

$$
L_{pe} = \mu_0 \frac{h}{w} x_1 \tag{3.33}
$$

C	:	Capacitance (F)
f	:	Pulse Frequency (Hz)
h	:	Distance between electrodes (m)
L_c	:	Internal Inductance of the capacitor (H)
L_e	:	Inductance due to wires and leads (H)
L_{pe}	:	Inductance due to current sheet moving down (H)
L'_{pe}	:	Inductance per unit channel length (Hm^{-1})
L_T	:	Total circuit inductance (H)
m_0	:	Mass of plasma at $t = 0$ (kg)
n_e	:	Electron density (m^{-3})
R_c	:	Capacitor resistance (Ω)
R_e	:	Wire and lead resistance (Ω)
R_p	:	Plasma resistance (Ω)
R_{pe}	:	Electrode resistance (Ω)
R_T	:	Total circuit resistance (Ω)
T_e	:	Electron temperature
w	:	Width of electrodes (m)
μ_0	:	Magnetic permeability of free space ($WbA^{-1}m^{-1}$)
τ	:	Characteristic pulse time (s)

Table 3.I. Parameters of the Parallel-Plates Ablative PPT Electromechanic Model [134].

In real situations, the electrical variables of the PPT actuator can be measured and collected. In this thesis we assume that the above PPT model can be used as an actual PPT for generating the data sets under healthy and faulty conditions.

3.6.2 PPT Configurations

The position and force direction of each thruster in the thrusters configuration is fundamental for performing the correct sequence of thruster's activation. Using the satellite body fixed CS, the thrust force generated for each thruster is obtained as follows:

$$^{b}\overline{F}_{th} = F_{th} \cdot {}^{b}\overline{e}_{th} \tag{3.34}$$

where ${}^{b}\overline{e}_{th}$ is the unit thrust vector and F_{th} is the magnitude of the thrust force. Equation (3.35) represents the generated torque about the CoM of the spacecraft, that is

$$^{b}\overline{T}_{th} = {}^{b}\overline{r}_{th} \times {}^{b}\overline{F}_{th} = F_{th} \cdot {}^{b}\overline{r}_{th} \times {}^{b}\overline{e}_{th} \tag{3.35}$$

To obtain full three-axis control, a minimum of four thrusters is needed, but in this thesis,

we consider the so-called six-independent PPT configuration (refer to Figure 3.9).

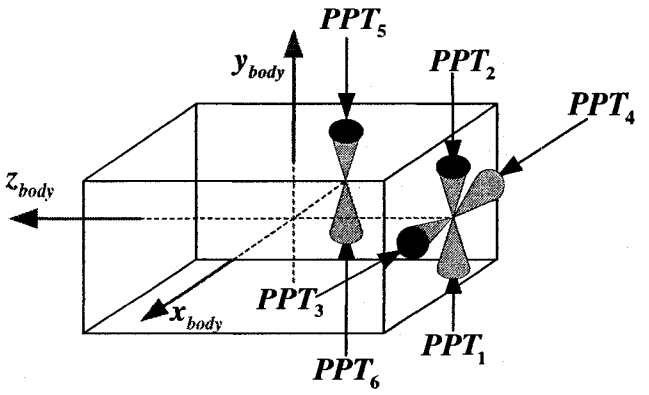

Figure 3.9. Six-Independent PPT Configuration.

In the above configuration, each thruster only generates a torque about a single axis of the spacecraft where independent control actuation is achieved. Equations (3.36) and (3.37) show the torque matrix and the total control torque that is applied to the satellite respectively:

$$A_{th} = \left(\begin{bmatrix} T_{th1,x} \\ T_{th1,y} \\ T_{th1,z} \end{bmatrix} \begin{bmatrix} T_{th2,x} \\ T_{th2,y} \\ T_{th2,z} \end{bmatrix} \begin{bmatrix} T_{th3,x} \\ T_{th3,y} \\ T_{th3,z} \end{bmatrix} \begin{bmatrix} T_{th4,x} \\ T_{th4,y} \\ T_{th4,z} \end{bmatrix} \begin{bmatrix} T_{th5,x} \\ T_{th5,y} \\ T_{th5,z} \end{bmatrix} \begin{bmatrix} T_{th6,x} \\ T_{th6,y} \\ T_{th6,z} \end{bmatrix} \right) \tag{3.36}$$

$$\overline{T}_{sys} = A_{th} \cdot \overline{f}_{sys} \tag{3.37}$$

where $T_{thi,j}$ is the magnitude that the *i-th* thruster generates in the direction of the *j*-axis. The vector $\overline{f}_{sys}$ represents a binary on-off set of signals which allows the activation of the thrusters. The calculation of this vector is shown in Equation (3.38) [84]. For the six-independent PPT configuration, the nullspace component $\overline{f}_{null}$ is shown in Table 3.II. The appropriated nullspace command u_i is calculated using Equation (3.39), that is

$$\begin{aligned} A_{th}^{I} &= \text{inv}(A_{th}) \\ \overline{f}_{sys} &= A_{th}^{I} \cdot \overline{T}_{com} - \sum_{i=1}^{6} u_i \overline{f}_{null,i} \end{aligned} \tag{3.38}$$

$$u_i = \min_j \left(A_{th}^{I} \cdot \overline{T}_{com} \right)_j \tag{3.39}$$

$\bar{f}_{null,3}$:	$(1 \;\; 1 \;\; 0 \;\; 0 \;\; 0 \;\; 0)^T$
$\bar{f}_{null,2}$:	$(0 \;\; 0 \;\; 1 \;\; 1 \;\; 0 \;\; 0)^T$
$\bar{f}_{null,3}$:	$(0 \;\; 0 \;\; 0 \;\; 0 \;\; 1 \;\; 1)^T$

Table 3.II. Nullspace Vectors for the Six-Independent PPT Configuration.

For the six-independent PPT configuration, the position vector ${}^{b}\bar{r}_{th}$ and the thrust vector ${}^{b}\bar{e}_{th}$ as shown in Equations (3.34) and (3.35) are specified in Table 3.III.

Thruster	Position vector ${}^{b}\bar{r}_{th}$	Thrust vector ${}^{b}\bar{e}_{th}$
PPT_1	$(0 \;\; 0 \;\; -z)^T$	$(0 \;\; 1 \;\; 0)^T$
PPT_2	$(0 \;\; 0 \;\; -z)^T$	$(0 \;\; -1 \;\; 0)^T$
PPT_3	$(0 \;\; 0 \;\; -z)^T$	$(-1 \;\; 0 \;\; 0)^T$
PPT_4	$(0 \;\; 0 \;\; -z)^T$	$(1 \;\; 0 \;\; 0)^T$
PPT_5	$(-x \;\; 0 \;\; 0)^T$	$(0 \;\; -1 \;\; 0)^T$
PPT_6	$(-x \;\; 0 \;\; 0)^T$	$(0 \;\; 1 \;\; 0)^T$

Table 3.III. Position and Thrust Vectors for the six-independent PPT Configuration.

Finally, using this configuration, the applied torque in the $+x$, $-x$, $+y$, $-y$, $+z$ and $-z$ is performed by the thrusters PPT_1, PPT_2, PPT_3, PPT_4, PPT_5 and PPT_6, respectively.

3.7 Conclusions

In this chapter, four coordinates systems are presented and explained. These coordinates systems provide the required reference frames in order to correctly calculate the position, attitude and velocity of a rigid body (e.g. spacecraft). Three attitude representation techniques are also defined. As discussed in Section 3.2.2, Quaternion technique presents important advantages over Euler angles and Direction Cosine Matrix (DCM) techniques therefore, the equations of motion that describe the rotational dynamics of the spacecraft are represented by this technique.

The concept of formation flying spacecraft is introduced and the motivations for using formation of multiple small spacecraft over a large spacecraft are given. In order to demonstrate the relevance of formation flying in the space field, example of past, current and future formation

flying space mission are provided. Formation flying control architectures and formation flying control laws are provided. Due to the advantages presented in Section 3.4, a quaternion error vector command law for a formation of three spacecraft flying in a leader/follower architecture is designed.

A list of different types of sensors and actuators of the attitude control subsystem of a spacecraft is provided and the required sensors and actuator used in our formation flying system is defined. Pulsed plasma thrusters (PPT) are chosen as the actuator of our formation flying spacecraft. A dynamical model describing the PPT's electromechanical system is provided and the PPT configuration, the so-called six-independent PPT configuration, is presented.

The dynamic formation flying system presented here is planned to be used in the following chapters of this thesis to simulate attitude maneuvers under normal and abnormal PPT's conditions. These simulations provide the required data for developing and testing our proposed FDI scheme.

Chapter 4

Spacecraft Fault Diagnosis Analysis

Fault detection and isolation (FDI) of critical control systems have been widely investigated during the past two decades. Systems such as autonomous spacecraft and formation of autonomous spacecraft demand detection and isolation of faulty components (e.g.: sensors and actuators) as early as possible to avoid fatal failures. The accuracy and precision of FDI schemes are strongly dependent on the availability of mathematical models. Developing precise models for complex nonlinear systems can be quite difficult and availability of mathematical models for all components is not always possible. Due to these limitations, in this chapter we propose a learning-based FDI scheme.

According to [73], [103], [104] and [105], neural networks has the capability to learn the component model from past input-output data and generate an analytical model. Standard multilayer perceptron networks can be used to model static nonlinear systems. To introduce dynamic properties to the network, we will employ dynamic neurons. The dynamic neuron can be constructed by adding an Infinite Impulse Response (IIR) filter to a static neuron. This will ensure that the activation of a neuron depends on its internal states [103].

In this chapter, a dynamic neural network is employed as a modeling tool for a Pulsed Plasma Thruster (PPT) actuator employed in the ACS of a spacecraft in a formation flying mission. Using this neural network model we will generate residual signals to detect the existence of a fault in the actuators. An important advantage of this FDI scheme is that only data from the electrical circuit of the PPT is needed to detect deviations in the amount of thrust produced.

4.1 Framework of the Proposed Fault Diagnosis

The simulations performed in this thesis have been implemented in Matlab and Simulink. Using the electromechanical model presented in Chapter 3 we simulate the PPT behavior for the generated pulses. Each simulated pulse has a duration of 30 msec with a sampling time of 0.01 msec. At t = 0, there is an initial capacitor voltage of 910 V which generates a nominal force of 100 μN. The six-independent PPT configuration includes three pairs of thrusters with a common capacitor per each pair of thrusters.

For practical operation of PPTs only electrical variables and temperatures are measured and monitored. Therefore, unplanned variations in the amount of thrust cannot be measured directly. Malfunctions in the PPT thruster can be introduced due to different sources. Based on material fatigue, waste accumulation and results that are discussed in [106] - [108], the following faulty cases are considered in this thesis:

- **Faulty Case 1 (Mass Fault Reduction):** Due to the reduction in the amount of propellant's mass that is utilized during the generation of the pulse, the amount of thrust generated by the pulse is also reduced. This propellant mass reduction can be produced due to the loss of elasticity of the thruster's spring. Under this undesirable condition, the fuel bar is not properly positioned and therefore the amount of propellant mass available is less than under normal conditions.
- **Faulty Case 2 (Faulty Ablation Process):** The ablation process transforms the solid propellant into the exhaust plasma, but small portions of the propellant may not be transformed, resulting in particles which are added to the inner face of the electrodes. After several pulses, the amount of particles added to the electrodes may become significant and potentially can be ablated and ionized during the generation of a new pulse resulting in an

augmentation in the amount of thrust generated by that pulse.

- **Faulty Case 3 (Conductivity Fault Reduction):** Due to wear and tear, conductivity of the wires, capacitor and electrodes may decrease. As a consequence of this, the amount of discharge current produced during the generation of the pulses is reduced resulting in a reduction of the amount of thrust.

To develop our proposed FDI system a data set composed of the following variables are generated:

- Capacitor Voltage $v(t)$,
- Thrust $y_1(t)$, and
- Discharge Current $y_2(t)$.

To represent a realistic situation Gaussian noise is added to the above measurements. It should be noted that a PPT pulse is considered healthy if the Thrust produced is within the interval Ω that is given by (4.1). Otherwise, the pulse is considered as being faulty, where

$$\begin{aligned} y_{1min} &= (1-0.15)\, y_{1nominal} \\ y_{1max} &= (1+0.15)\, y_{1nominal} \\ \Omega &= [y_{1min}, y_{1max}] \end{aligned} \tag{4.1}$$

and $y_{1nominal}$ is the nominal Thrust (100 μN).

4.2 Simulations for the PPT Operations

In this section we present a simulated data set for a PPT actuator working under both healthy and faulty conditions. For the healthy case, the resulting capacitor voltage, thrust and discharge current correspond to the nominal case. In the case of faulty scenarios, we obtain the behavior of the above signals for the three types of faults that were described in the previous section.

4.2.1 PPT Operation Under Healthy Scenario

A PPT acting under healthy conditions generates a force within the interval that is defined in equation (4.1). Figures 4.1 (a)-(c) show the behavior of capacitor voltage, thrust and discharge current for an initial capacitor voltage of 910 V (applied at time t = 0).

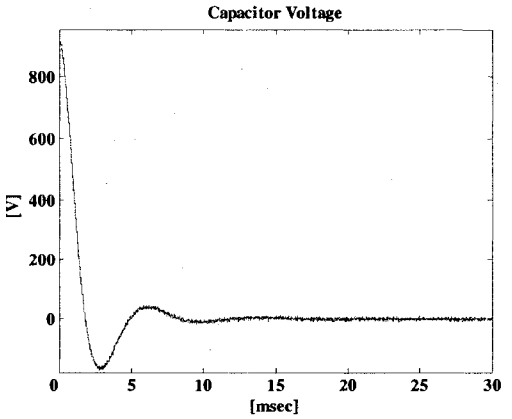

Figure 4.1. (a) Capacitor Voltage with Measurement Noise (Healthy Scenario).

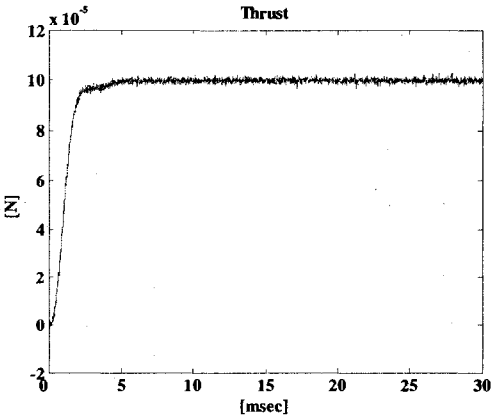

Figure 4.1. (b) Thrust with Measurement Noise (Healthy Scenario).

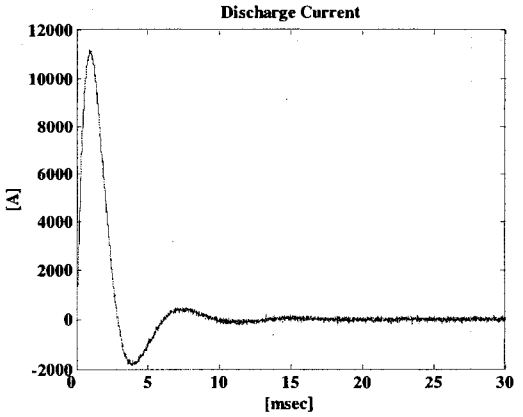

Figure 4.1. (c) Discharge Current with Measurement Noise (Healthy Scenario).

Table 4.I shows the initial, minimum, maximum and final value of the simulated data set as well as the settling time.

Variable	initial value	final value	max.	min.	t_s [msec]
$v(t)$	910 [V]	0 [V]	918.24 [V]	-172.21 [V]	12.50
$y_1(t)$	0 [N]	1e-4 [N]	1.03e-4 [N]	0 [N]	7.60
$y_2(t)$	0 [A]	0 [A]	1.11e4 [A]	-1965.5 [A]	15.40

Table 4.I. Number of Pulses Generated by S/C_{f1} and S/C_{f2} Thrusters (Healthy Scenario).

4.2.2 PPT Operation Under Faulty Scenario 1

Mass fault reduction decreases the amount of propellant (m_0) consumed during each pulse. Under healthy conditions, m_0 = 2.58e-8 kg but under this faulty condition, a value of m_0 = 3.00e-9 kg is used. Figures 4.2 (a) – (b) show the resulting simulated responses.

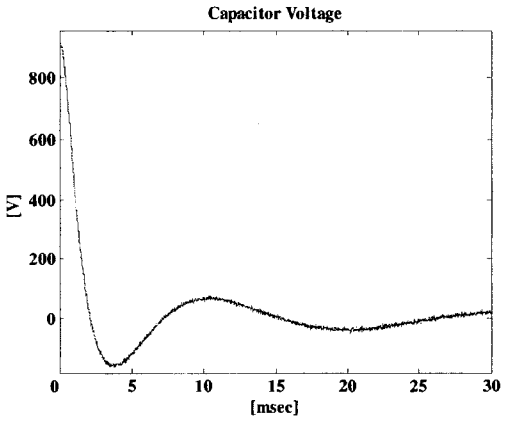

Figure 4.2. (a) Capacitor Voltage with Measurement Noise (Faulty Scenario 1).

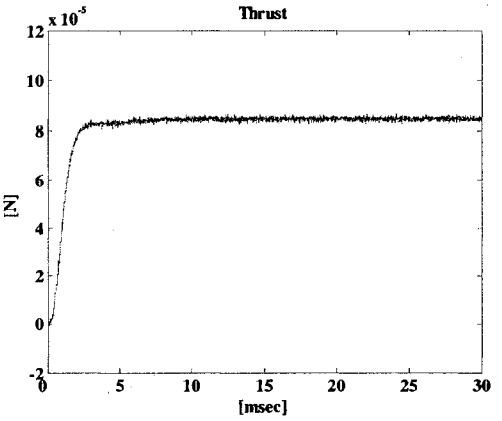

Figure 4.2. (b) Thrust with Measurement Noise (Faulty Scenario 1).

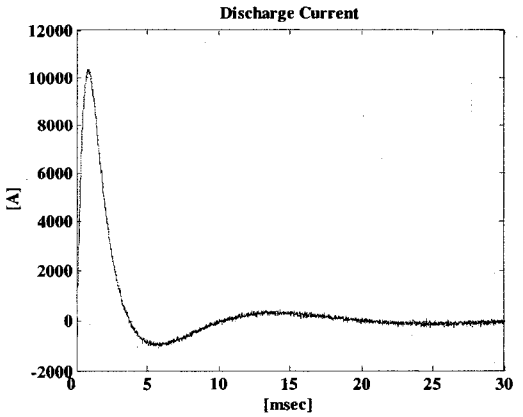

Figure 4.2. (c) Discharge Current with Measurement Noise (Faulty Scenario 1).

Table 4.II shows the initial, minimum, maximum and final value for the simulated data set where the settling time is also included. Under this condition, the PPT generates a force of 85 μN which is 15% less than the nominal value and is just bellow the lower limit that is defined by equation (4.1).

Variable	initial value	final value	max.	min.	t_s [msec]
$v(t)$	910 [V]	20 [V]	916.50 [V]	-160.94 [V]	26.00
$y_1(t)$	0 [N]	0.85e-4 [N]	0.87e-4 [N]	0 [N]	9.00
$y_2(t)$	0 [A]	50 [A]	1.04e4 [A]	-1094.5 [A]	25.60

Table 4.II. Number of Pulses Generated by S/C_{f1} and S/C_{f2} Thrusters (Faulty Scenario 1).

4.2.3 PPT Operation Under Faulty Scenario 2

Sedimentation (particles of propellant) added to the inner face of electrodes can generate thrust levels beyond the acceptable range as shown by equation (4.1). To simulate this faulty scenario, the width of the electrodes w = 0.0254 m is changed to w = 0.02195 m. For this faulty scenario, the resulting responses are shown in Figures 4.3 (a) – (c).

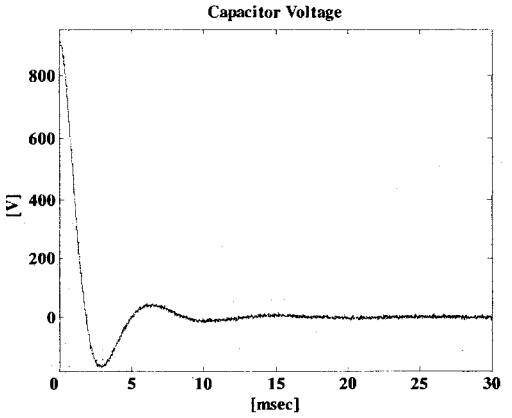

Figure 4.3. (a) Capacitor Voltage with Measurement Noise (Faulty Scenario 2).

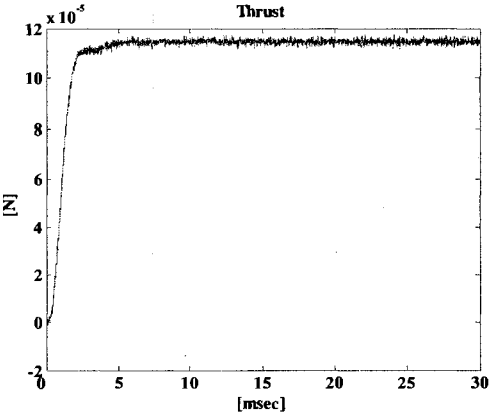

Figure 4.3. (b) Thrust with Measurement Noise (Faulty Scenario 2).

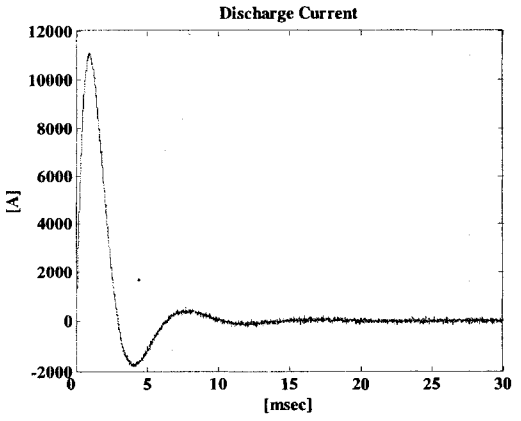

Figure 4.3. (c) Discharge Current with Measurement Noise (Faulty Scenario 2).

Table 4.III shows the initial, minimum, maximum and final value for the simulated data set where the settling time is also included. Under this condition, the PPT generates a force of 1.15

μN which is 15% more than the nominal value and is just bellow the lower limit that is defined by equation (4.1).

Variable	initial value	final value	max.	min.	t_s [msec]
$v(t)$	910 [V]	3 [V]	912.54 [V]	-169.79 [V]	18.50
$y_1(t)$	0 [N]	1.15e-4 [N]	1.18e-4 [N]	0 [N]	6.30
$y_2(t)$	0 [A]	0 [A]	1.11e4 [A]	-1829 [A]	17.70

Table 4.III. Number of Pulses Generated by S/C_{f1} and S/C_{f2} Thrusters (Faulty Scenario 2).

4.2.4 PPT Operation Under Faulty Scenario 3

Conductivity of the electrical components (wires, capacitor, electrodes, etc.) may be affected due to their usage. This loss of conductivity may generate faulty levels of thrust. To simulate this faulty scenario, the resistance of the electrodes R_{pe} = 0.00 Ω is changed to R_{pe} = 0.008 Ω. Figures 4.4 (a) – (c) show the corresponding responses.

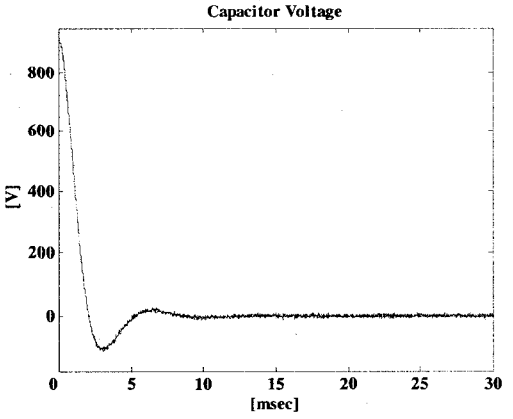

Figure 4.4. (a) Capacitor Voltage with Measurement Noise (Faulty Scenario 3).

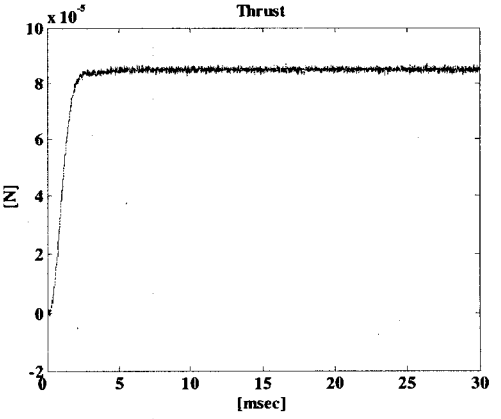

Figure 4.4. (b) Thrust with Measurement Noise (Faulty Scenario 3).

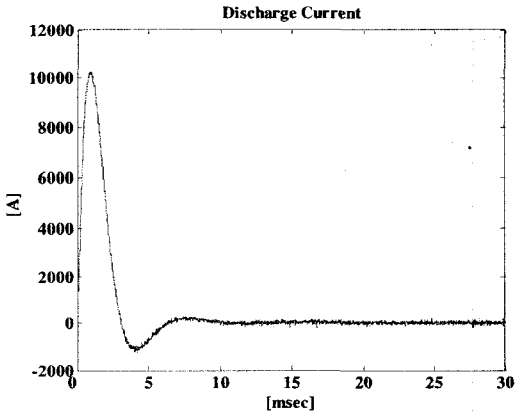

Figure 4.4. (c) Discharge Current with Measurement Noise (Faulty Scenario 3).

Table 4.IV shows the initial, minimum, maximum and final value for the simulated data set where the settling time is also included. Under this condition, the PPT generates a force of 85 μN which is 15% less than the nominal value and is just bellow the lower limit that is defined by equation (4.1).

Variable	initial value	final value	max.	min.	t_s [msec]
$v(t)$	910 [V]	1 [V]	918.25 [V]	-115.25 [V]	10.80
$y_1(t)$	0 [N]	0.85e-4 [N]	0.87e-4 [N]	0 [N]	0.55
$y_2(t)$	0 [A]	0 [A]	1.03e4 [A]	-1289 [A]	11.70

Table 4.IV. Number of Pulses Generated by S/C_{f1} and S/C_{f2} Thrusters (Faulty Scenario 3).

The simulations for the above three faulty scenarios generate faults with severity of 15%. Faulty scenarios 1 and 3 generate a reduction in the thrust from 100 μN to 85 μN meanwhile the faulty scenario 2 produces an increase from the nominal thrust to the value of 115 μN. According to the definitions that are given by equation (4.1), this corresponds to the minimum level of fault (low severity fault).

4.3 Neural Network FDI Scheme

Precise attitude control subsystem is a strongly important issue for all formation flying systems, especially for interferometer missions such as Terrestrial Planet Finder (TPF) or DARWIN ([2], [14], [15], [23], [88], [109] and [110]). Faulty actuators (e.g. PPTs) affect the attitude control subsystem of the spacecraft and then, the performance of the formation flying system. Under this undesirable condition, recovery actions (i.e. at actuator, spacecraft or formation flying levels) are needed and then, the necessity of fault detection and isolation systems becomes evident.

As mentioned in Section 4.1, for practical operations of PPTs, only electrical variables and temperatures are measured and monitored therefore, the amount of thrust produced by the PPTs cannot be measured and then, cannot be used for detecting and isolating faults. On the other hand, due to the complexity of the PPT dynamic system, it is reasonable to assume that precise mathematical model are not available and then, model-based FDI schemes cannot satisfy the accuracy and precision required.

Neural networks technique is a history-based approach capable of learning models of nonlinear systems from past input-output data. Application of neural networks technique for fault diagnosis purposes has been successfully applied for various type of systems such as robotics ([111]-[113]), industrial processes ([114]-[117]), among others ([118]-[122]). In the case of spacecraft systems, literature provides interesting examples of neural network-based FDI schemes ([123]-[127]).

Our proposed neural network-based FDI system uses a special multilayer perceptron networks which is called Dynamic Neural Network (DNN) due to the utilization of dynamic neurons [103]. The construction of our proposed neural network-based FDI system can be divided into four consecutive steps:

Neural Network Training Phase: In this phase the parameters of the DNN are adjusted until the required modeling accuracy is achieved. As discussed in [126], the network scheme used during the training phase is the series-parallel identification model that is shown in Figure 4.5, where $u_{norm}(k)$ and $y_{2norm}(k)$ are the normalized representation of the capacitor voltage and delayed discharge current, respectively. Output $y_{2norm}(k+1)$ represents the normalized discharge current.

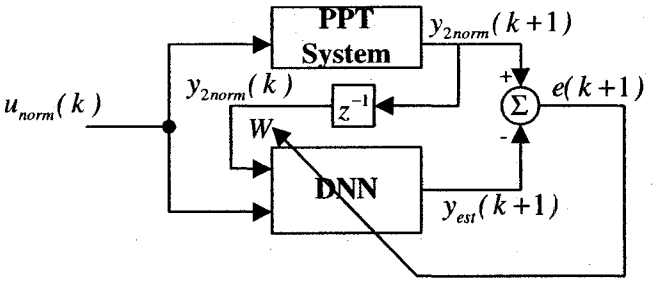

Figure 4.5. Series-parallel identification model during the training phase.

To adjust the network parameters of the dynamic neural network (input weights and filter coefficients), pairs of healthy input/output data set is used. By comparing the network output with the estimated network output, the error $e(k+1)$ is calculated and back-propagated through various layers updating the network parameters W.

Neural Network Validation Phase: The DNN is tested with new data sets to prove that the modeling accuracy of the network is valid for data used during the training phase as well as for different healthy data sets. During the validation phase, a modified architecture as depicted in Figure 4.6 is applied ([126]). This is motivated by the observation that after the training phase, one can assume that the difference between the actual output $y_{2norm}(k+1)$ and its estimated value $y_{est}(k+1)$ is sufficiently small. Therefore can employ $y_{est}(k+1)$ instead of $y_{2norm}(k+1)$ as an input to the network.

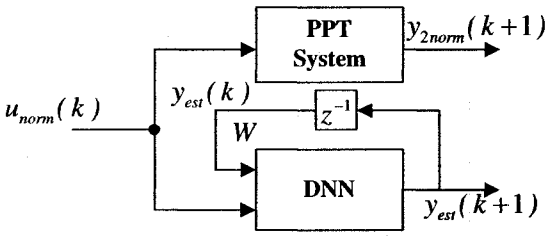

Figure 4.6. Series-parallel identification model during the validation phase.

For testing the identification and representation performance capabilities of our proposed DNN, various healthy pairs of input/output data sets must be presented. If the difference between $y_{est}(k+1)$ and $y_{2norm}(k+1)$ is considered acceptable, the validation phase is considered ended.

Threshold Determination: Comparing the actual and estimated outputs (i.e. system and DNN's output, respectively), the health status of the system can be evaluated. The *Threshold* determines if the data set presented to the network corresponds to a *healthy* or *faulty* scenario. The *Threshold* value is calculated by using collected healthy data. To calculate this constant, a mathematical expression based on the mean and standard deviation is used. This expression is given by (4.2)

$$Threshold = \frac{\sum_{i=1}^{n} MAE(i)}{n} + \sigma\left(max(MAE)_{i=1}^{n} - \frac{\sum_{i=1}^{n} MAE(i)}{n} \right) \tag{4.2}$$

where, $MAE(i)$ is the Mean Absolute Error of the data set $i=1,2,...,n$. The coefficient σ is a constant which is used to adjust the sensitivity of our FDI scheme.

FDI Scheme Implementation: The implementation of the entire FDI system is the final step. At this stage, the FDI scheme is ready to be used and is connected to the system. Our proposed DNN based FDI scheme is shown in Figure 4.7. The voltage $v(k)$ and the estimated current $y_{est}(k)$ are normalized before being presented to the DNN. Using the actual output $y_2(k+1)$ and the output of the network $y_{est}(k+1)$ the Decision Making Block calculates the *MAE* for the entire data set (corresponding to a single pulse of the thruster). The *MAE* is compared with the *Threshold* to detect if the pulse is healthy or faulty. The classification signature is called *Health Status*.

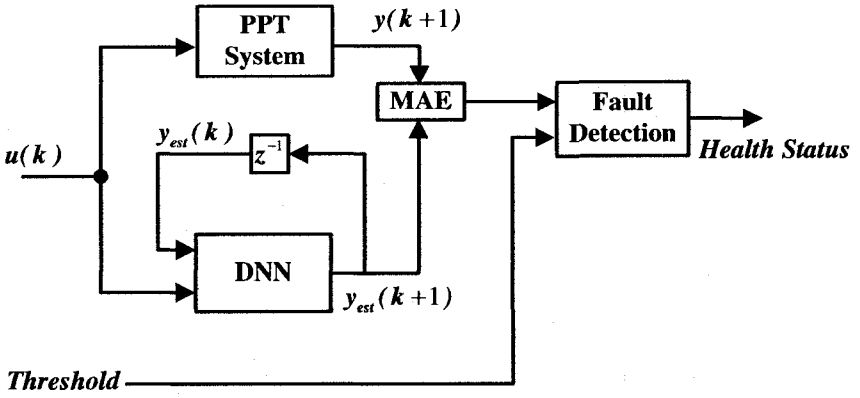

Figure 4.7. FDI scheme for a PPT system.

The neural network considered in this thesis is a multilayer perceptron network whit neurons having internal feedbacks. As presented in [105], [122]-[128], these special neurons allow the network to achieve dynamics properties. Figure 4.8 shows the general structure of the so-called Dynamic Neuron Model (DNM) [103], [105].

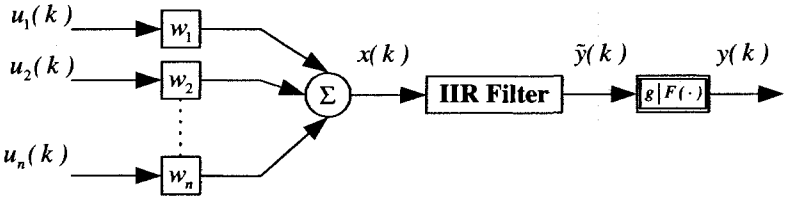

Figure 4.8. Structure of the DNM with *n* inputs.

The set $U(k) = [u_1(k), u_2(k),\ldots\ldots, u_n(k)]^T$ and $W = [w_1, w_2,\ldots\ldots, w_n]^T$ are the input and weight vectors, respectively. An Infinite Impulse Response (IIR) Filter is introduced to generate dynamics in the neuron such that activation of a neuron depends on its internal states [130], [103]-[105], [128], [129]. The block $g|F(\cdot)$ is the activation function of the neuron. Parameter g,

is the slope of the nonlinear activation function $F(\cdot)$.

The dynamic model of the above neuron is described by the following set of equations:

$$
\begin{aligned}
x(k) &= \sum_{i=1}^{n} w_i u_i(k) \\
\tilde{y}(k) &= -\sum_{i=1}^{r} a_i \tilde{y}(k-i) + \sum_{i=0}^{r} b_i x(k-i) \\
y(k) &= F\left(g \cdot \tilde{y}(k)\right)
\end{aligned}
\tag{4.3}
$$

where the signal $x(k)$ represents the input to the filter, the coefficients a_i, $i = 1,2,....,r$ and b_i, $i = 0,1,....,r$ are the feedback and feed-forward filter parameters, respectively, and r is the order of the filter. Finally, $\tilde{y}(k)$ represents the output of the filter which is the input to the activation function. Table 4.V shows a detail characteristic of the dynamic neural network.

Structure of the Network	2 – 10 – 1
IIR- Filter order	2nd order
***F(·)* (hidden layer):**	Hyperbolic Tangent Sigmoid
***F(·)* (output layer):**	Linear

Table 4.V. Dynamic Neural Network Specifications.

Among others training algorithm ([128]-[132]), the training algorithm used here is the Extended Dynamic Back Propagation (EDBP) algorithm ([105]). The training phase is performed until a termination criterion (*t.c.*) is satisfied. For *t.c.* we used the mean square error (*mse*) criterion. The *mse* for the entire data set is calculated and when $mse \leq t.c.$ the training is stopped. The termination criterion used is $mse = 1x10^{-4}$. Figure 4.9 shows the actual output of the PPT electromechanical model and the estimated output generated by the dynamic neural network.

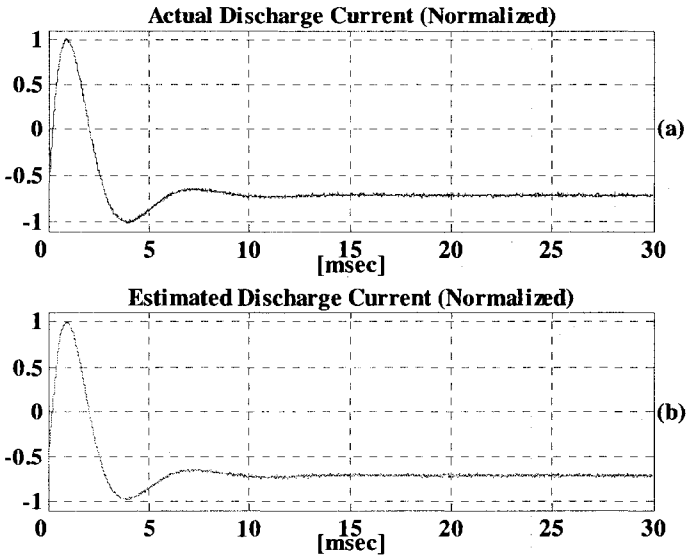

Figure 4.9. (a) Actual Discharge Current (Normalized) and (b) Estimated Discharge Current (Normalized).

To validate the modeling capabilities of our proposed DNN, we utilized 120 healthy data sets. To simulate these pulses, the capacitor voltage was initiated at different values (from 857 V to 980 V). Based on the healthy interval Ω (refer to equation (4.1)) and the nominal Thrust (100 μN), the upper and lower bounds of Ω are 115 μN and 85 μN, respectively. Details are shown in Table 4.VI.

	MINIMUM	MAXIMUM
Capacitor Voltage (t = 0.0)	857 [V]	980 [V]
Generated Thrust	89.1 [μN]	114.9 [μN]
Bounds	85 [μN]	115 [μN]

Table 4.VI. Healthy Maximum and Minimum Capacitor Voltage and Thrust.

Figure 4.10 shows the 120 healthy pulses utilized to validate the DNN model and to define a valid *Threshold* value. After the calculation of the *MAE* value for each of the 120 pulses, we calculated the *Threshold* value using the definition given by Equation (4.3).

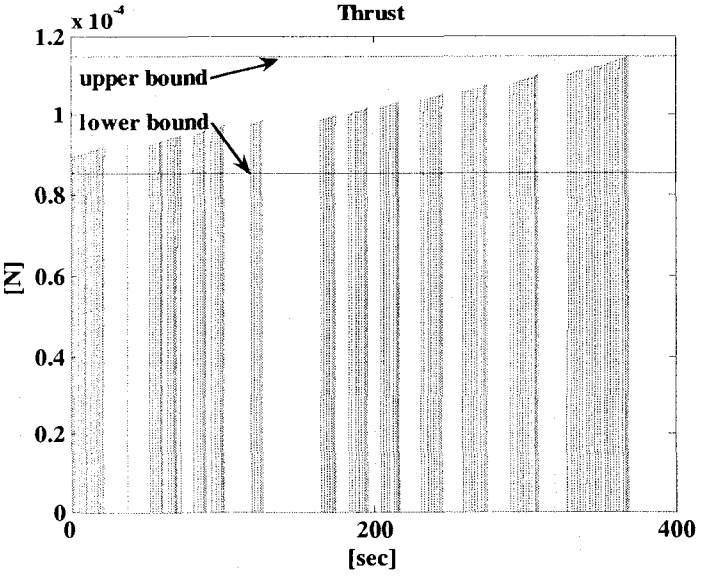

Figure 4.10. Healthy Pulses Set.

The coefficient σ was fixed at 1.15. Finally, we obtain a fix *Threshold* value of 0.0371. As shown in Figure 4.11, the obtained *MAE* factors are bellow the *Threshold* which implies that all these pulses are considered as healthy pulses.

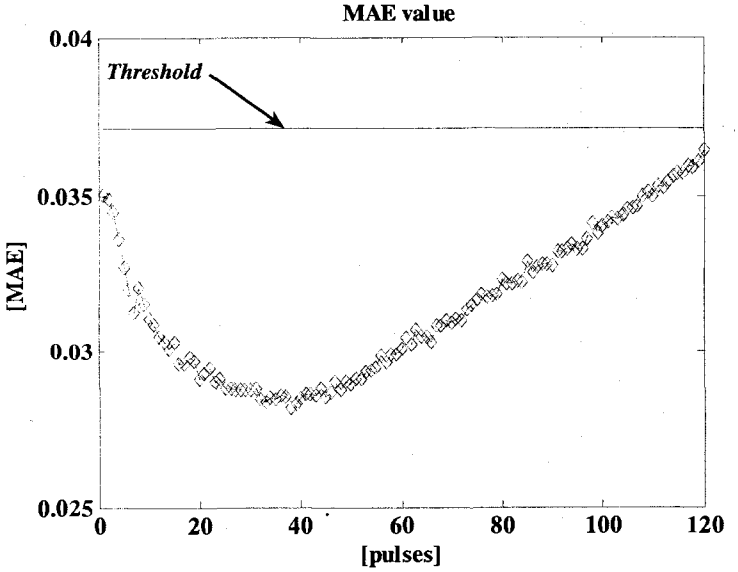

Fig. 4.11. Fixed Threshold Value.

4.4. The FDI Simulation Results

Generally, a six-independent configuration PPT system is composed of three clusters of two thrusters sharing the same capacitor. Our proposed FDI scheme can be implemented by applying one DNN to each cluster. In this way, we not only can detect a fault, but also can identify (isolate) the faulty thruster. As described in Chapter 3, pair of thrusters, which share the same capacitor, are positioned in opposite directions and together provide the attitude control force and torque for one of the axes of a three-axis stabilized spacecraft.

For the sake of simplification, we present the results concerned with thrusters PPT_3 and PPT_4 which generate the rotation around the pitch angle. The parameters for both thrusters are shown in Table 4.VII.

Max. Thrust:	100 [μN]
Capacitor Voltage (t = 0 [sec])	910 [V]
Max. Discharge Current:	11090 [A]

Table 4.VII. Parameters for PPT_3 and PPT_4.

The fault types described in Section 4.2 are utilized to investigate the performance of our proposed FDI scheme. Three faulty scenarios are considered as described bellows:

Faulty Scenario 1: A decrease in the amount of thrust, due to mass fault reduction of PPT_3 is simulated. The mass m_0 = 2.58*e*-8 kg is linearly decreased until it reaches m_0 = 2.00*e*-10 kg. This progressive reduction in the amount of mass is modeled by equation (4.4).

$$m_0 = 2.58\times10^{-8} - i\left(0.04\times10^{-8}\right); \quad i = 1,2,3,.....64 \tag{4.4}$$

Figure 4.12 shows the FDI results that are obtained by utilizing the proposed neural network scheme. According to this figure, the behavior of the PPT_3 is considered healthy for the first 46 pulses and faulty for the last 18 pulses. Our FDI scheme does not detect faults in any of the pulses that are generated by the PPT_4.

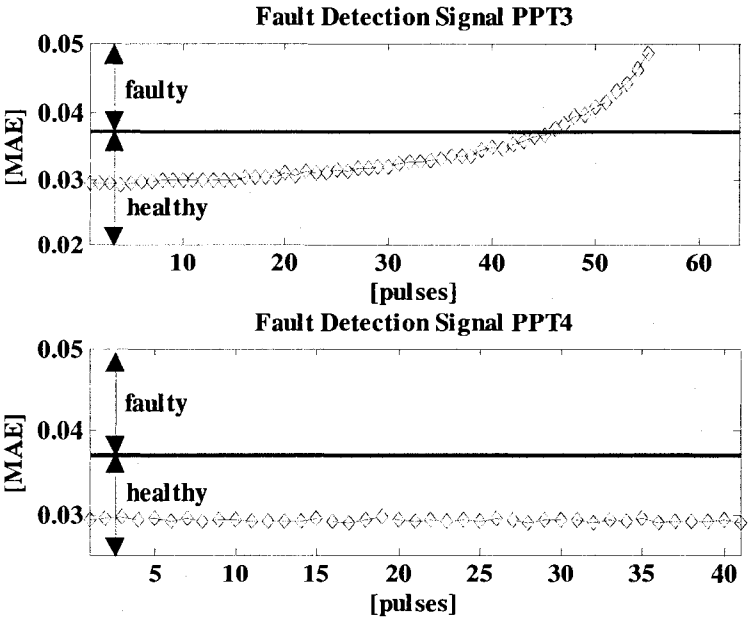

Figure 4.12. FDI Results for the PPT_3 and the PPT_4 Under Faulty Scenario 1.

The actual pulses generated by the pair of thrusters are shown in Figure 4.13. The first 56 pulses generated by the PPT_3 are inside the healthy interval as defined by equation (4.1), meanwhile the remaining 8 pulses are classified as faulty. On the other hand, all the pulses that are generated by the PPT_4 are correctly classified as healthy pulses. Table 4.VIII contains the details of the results obtained under this faulty scenario.

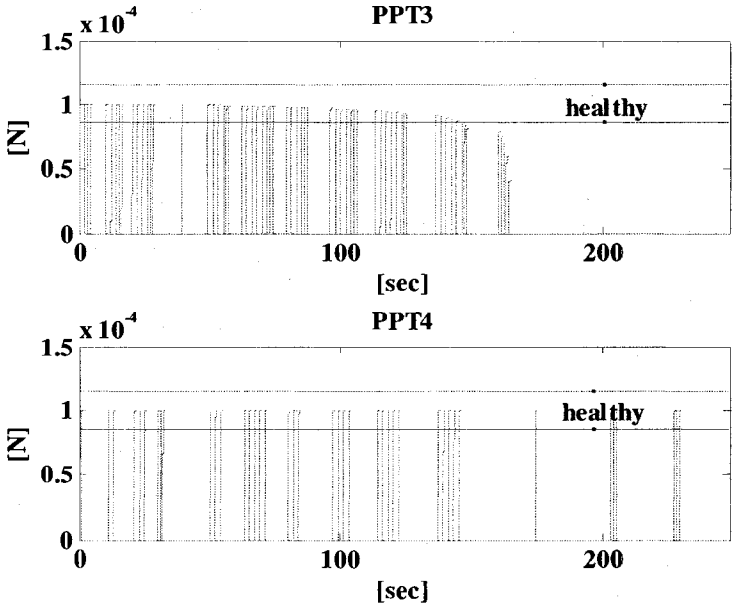

Figure 4.13. Actual Thrust Generated by the PPT_3 and the PPT_4 Under Faulty Scenario 1.

	ACTUAL HEALTHY PULSES	ACTUAL FAULTY PULSES	HEALTHY PULSES (FDI SCHEME)	FAULTY PULSES (FDI SCHEME)
PPT_3	56	08	46	18
PPT_4	41	00	41	00

Table 4.VIII. Actual and Detected Condition of the Generated Pulses (Faulty Scenario 1).

Faulty Scenario 2: A variation of the amount of thrust, due to the particles being added to the inner face of electrodes of the PPT_4 is simulated. The width of the electrode w = 0.0254 m is linearly decreased according to equation (4.5), that is

$$w = 0.0254 - i(0.0004); \quad i = 1,2,3,.....41 \tag{4.5}$$

Figure 4.14 shows the FDI results that are obtained by utilizing the proposed neural network scheme. According to this figure, the behavior of the PPT_3 is considered healthy for all the 64 pulses generated. In the case of the PPT_4, our FDI scheme classifies the first 28 pulses as healthy and the last 13 pulses as faulty.

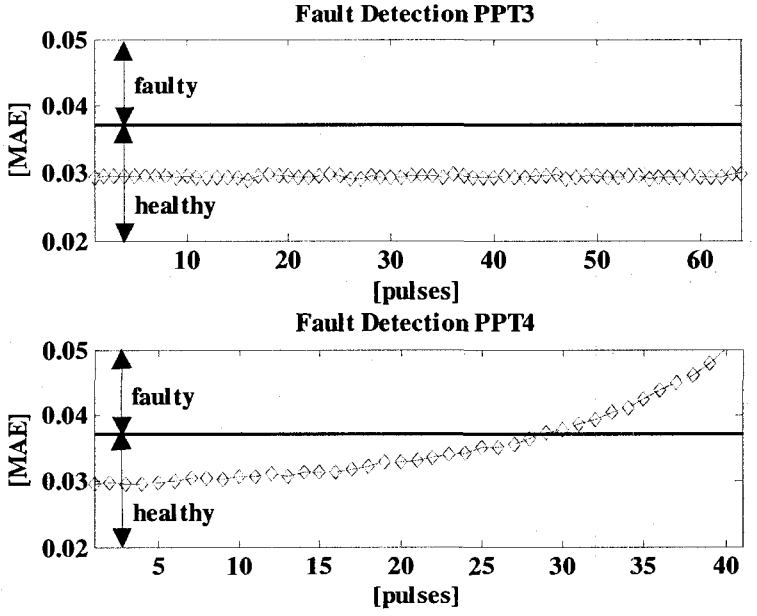

Figure 4.14. FDI results for PPT_3 and PPT_4 Under Faulty Scenario 2.

The actual pulses that are generated by the pair of thrusters are shown in Figure 4.15. The complete set of pulses generated by the PPT_3 is within the healthy interval (85 – 115) μN. On the

other hand, only the first 8 pulses that are generated by the PPT_4 are healthy. The other 33 pulses are classified as faulty pulses. Table 4.IX shows the actual healthy and faulty pulses and the classification that is obtained by using our FDI scheme.

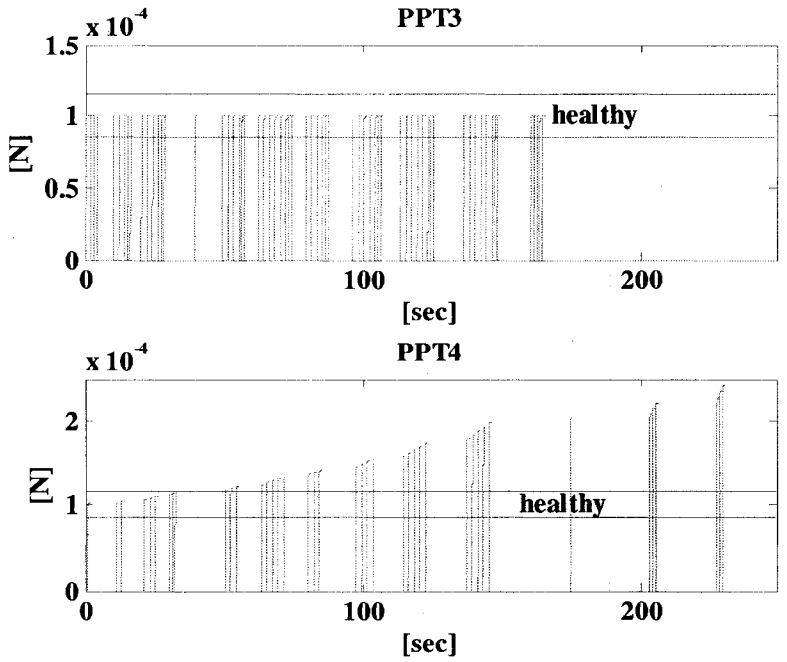

Figure 4.15. Actual Thrust Generated by the PPT_3 and the PPT_4 Under Faulty Scenario 2.

	ACTUAL HEALTHY PULSES	ACTUAL FAULTY PULSES	HEALTHY PULSES (FDI SCHEME)	FAULTY PULSES (FDI SCHEME)
PPT_3	64	00	64	00
PPT_4	8	33	28	13

Table 4.IX. Actual and Detected Condition of the Generated Pulses (Faulty Scenario 2).

Faulty Scenario 3: Change in the conductivity of the electrical components of the thruster affects the generation of the thrust. This faulty scenario is simulated by injecting faults to the thruster PPT_3. The resistance of the electrode R_{pe} = 0.00 Ω is gradually increased according to equation (4.6), that is

$$R_{pe} = 0.00 - i(0.00015); \quad i = 1,2,3,.....64 \tag{4.6}$$

Figure 4.16 shows the classification of the pulses that are generated by the PPT_3 and the PPT_4. In the case of PPT_3, the first 51 pulses are classified as healthy pulses while the following

13 pulses are classified as faulty pulses. The 41 pulses generated by the PPT_4 are classified as healthy pulses.

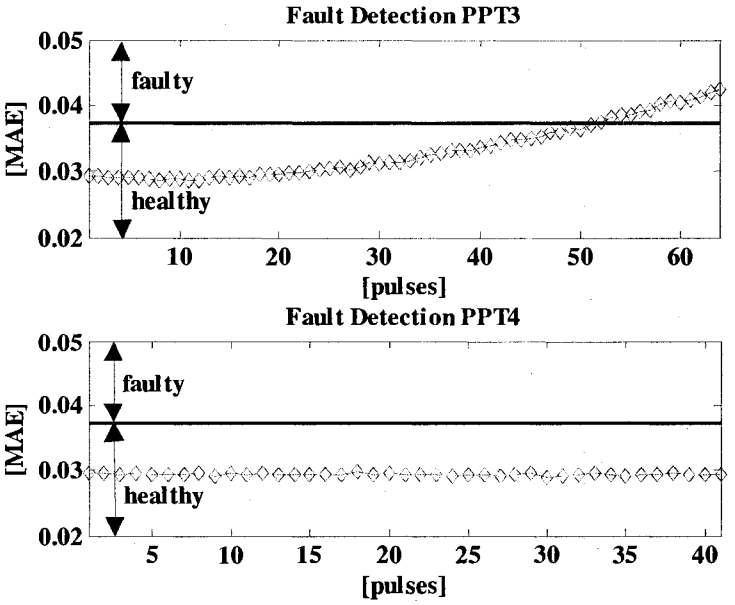

Figure 4.16. FDI Results for the PPT_3 and the PPT_4 Under Faulty Scenario 3.

The pulses that are generated by the PPT_3 and the PPT_4 are shown in Figure 4.17. PPT_3 generated a total of 64 pulses where the first 46 are considered as healthy pulses and the remaining 18 are considered as faulty pulses. For the case of PPT_4 the 41 pulses generated are within the healthy interval. As in the previous scenarios, the results are shown in Table 4.X.

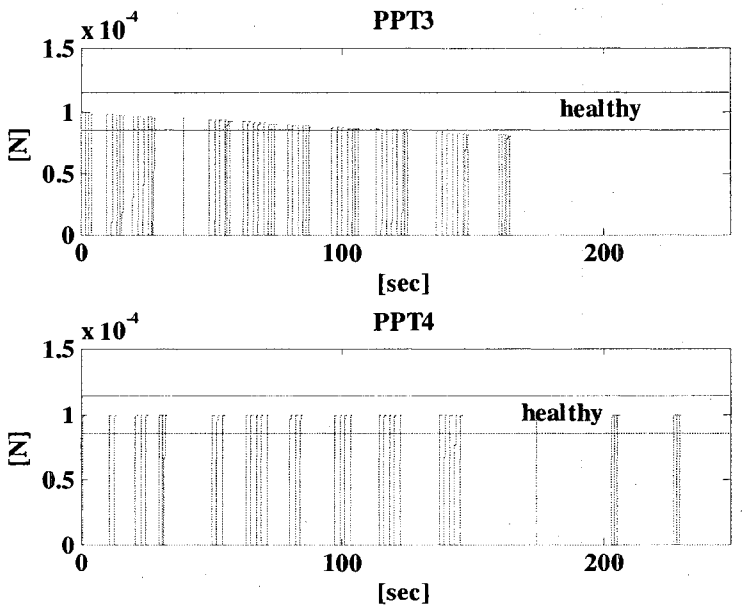

Figure 4.17. Actual Thrust Generated by PPT_3 and PPT_4 Under Faulty Scenario 3.

	ACTUAL HEALTHY PULSES	ACTUAL FAULTY PULSES	HEALTHY PULSES (FDI SCHEME)	FAULTY PULSES (FDI SCHEME)
PPT_3	46	18	51	13
PPT_4	41	00	41	00

Table 4.X. Actual and Detected Condition of the Generated Pulses (Faulty Scenario 3).

To evaluate the performance of our proposed FDI scheme, we use the Confusion Matrix approach ([133]). Equation (4.7) shows the structure of this matrix. The specific evaluation terms shown in equations 4.8 (a)–(f) are: *Accuracy*, *True Healthy*, *False Healthy*, *True Faulty*, *False Faulty* and *Precision*, respectively.

		PREDICTED	
		faulty	healthy
ACTUAL	faulty	A	B
	healthy	C	D

(4.7)

$$Accuracy = \frac{A+D}{A+B+C+D} \tag{4.8a}$$

$$True\ Healthy = \frac{D}{C+D} \tag{4.8b}$$

$$False\ Healthy = \frac{B}{A+B} \tag{4.8c}$$

$$True\ Faulty = \frac{A}{A+B} \tag{4.8d}$$

$$False\ Faulty = \frac{C}{C+D} \tag{4.8e}$$

$$Precision = \frac{D}{B+D} \tag{4.8f}$$

From the total amount of pulses generated for the pair of thrusters, we obtain the following values: $A = 34$, $B = 25$, $C = 10$ and $D = 246$. The results given by the Confusion Matrix are shown

in the following table:

Accuracy	:	88.89 [%]
True Healthy	:	96.09 [%]
False Healthy	:	42.37 [%]
True Faulty	:	57.63 [%]
False Faulty	:	3.90 [%]
Precision	:	66.67 [%]

Table 4.XI. Confusion Matrix Results.

These results indicate that the proposed FDI scheme is capable of correctly classify the 96.09% of the healthy pulses and the 57.63% of the faulty pulses. The accuracy level (88.89%) and the amount of healthy pulses misclassified as faulty (3.90%) are acceptable. The drawback and negative results include a poor level of precision, which we only could reach a level of 66.67%, and a large percentage of misclassification of faulty pulses (42.37%).

4.5. Conclusions

A dynamic neural network-based fault detection and isolation scheme is developed to autonomously detect faults in a PPT system of a spacecraft. Our proposed FDI scheme requires data from the electrical circuit of thrusters avoiding a need for direct measurement of the thrust. According to the simulation results presented it can be concluded that the proposed FDI scheme is not properly capable of correctly classifying all of the faulty pulses that are generated during the experimental operations. The utilization of a fixed *Threshold* has resulted in inadequate capability for detecting faults under the three different faulty scenarios. Using a Confusion Matrix evaluation criteria we have demonstrated a high level of accuracy but the precision level is below what is expected. Furthermore, the data set presented to the proposed scheme requires a sampling time of the order of milliseconds. For on-line fault diagnosis proposes, this amount of computation load may not be acceptable.

Independent of the fault's source, the desirable scheme must be capable of detecting faults in

a more reliable fashion and must perform it with a minimum amount of computational effort. In the following chapter, the health status of the formation flying system is investigated. The data that is extracted from the formation flying attitude control subsystem is then investigated to design an alternative fault diagnosis and health monitoring system.

Chapter 5

A Formation Flying Fault Diagnosis System

The idea of a formation of small spacecraft that can perform the same duties of a single large spacecraft is valid only when the coordination of those small spacecraft fulfills the mission's requirements. Terrestrial Planet Finder (TPF) and Darwin (refer to [2], [14], [15], [23], [88], [109] and [110]) are examples of formation flying missions where the success of the mission depends on the accuracy of the formation flying attitude and orbital controls. It is evident that detection of malfunctioning sensors and actuators which could result in loss of coordination is highly desirable.

In Chapter 4 we have developed an FDI system that was based on dynamic neural networks for health monitoring PPT actuators of a spacecraft. We have studied the FDI system performance for a PPT under three faulty scenarios. Confusion matrix results showed that although the accuracy is acceptable (88.89%), the precision is below expectation (66.67%). The development of an alternative or a complementary FDI system is desirable.

In this chapter a new FDI approach is developed. Dynamic neural networks theory is employed to model the relative attitude of a follower spacecraft with respect to the leader spacecraft in a formation flying mission. Using this neural network model, residual signals are generated for detecting the existence of faults in the actuators of the followers. An important advantage of this FDI scheme is that only data from the follower's ACS is used to detect abnormalities in the actuators.

5.1 Development of a Formation Flying Simulation Environment

The simulations that are performed below have been implemented in Matlab and Simulink. Orbital and attitude parameters, environmental disturbances and generated torque magnitudes

have been extracted from the simulation parameters provided in [84]. The force generated by each PPT is 100 μN and the magnitudes of the parameters for the electromechanical PPT model are provided in [134]. Table 5.I shows the geometry of the small spacecraft of our formation flying system defined in Section 3.4.2.

Geometry	:	$10\times10\times10\ \text{cm}^3$
Mass	:	1 kg
Inertia Matrix	:	$I=\begin{pmatrix}0.00198 & 0 & 0\\ 0 & 0.00210 & 0\\ 0 & 0 & 0.00188\end{pmatrix}\text{kg}\cdot\text{m}^2$

Table 5.I. Spacecraft Parameters.

The geometry (i.e. dimensions) of the spacecraft are used to calculate the Torque generated by the six-independent PPT configuration that is presented in Section 3.3 (refer to equation (3.35)). Therefore, the position vectors $^{b}\vec{r}_{th}$ that are presented in Table 3.III can now be rewritten as follows:

Thruster	Position vector $^{b}\vec{r}_{th}$	Thrust vector $^{b}\vec{e}_{th}$
PPT_1	$(0\ \ 0\ \ -0.05)^T$	$(0\ \ 1\ \ 0)^T$
PPT_2	$(0\ \ 0\ \ -0.05)^T$	$(0\ \ -1\ \ 0)^T$
PPT_3	$(0\ \ 0\ \ -0.05)^T$	$(-1\ \ 0\ \ 0)^T$
PPT_4	$(0\ \ 0\ \ -0.05)^T$	$(1\ \ 0\ \ 0)^T$
PPT_5	$(-0.05\ \ 0\ \ 0)^T$	$(0\ \ -1\ \ 0)^T$
PPT_6	$(-0.05\ \ 0\ \ 0)^T$	$(0\ \ 1\ \ 0)^T$

Table 5.II. Position and Thrust Vectors for the Formation Flying Spacecraft.

On the other hand, Table 5.I shows the values of the inertial matrix I that is defined in equation (3.11) and that are used in the nonlinear state space model for the formation flying spacecraft's rotational movement (refer to equations (3.16)-(3.18)).

The Table 5.III shows the values of the gain matrices that are presented in equations (3.21) and (3.28) and that are used by the Quaternion Error Vector Command Laws that are implemented in the formation flying spacecraft.

$\mathbf{K_d}$ ($s/c_1 = s/c_{f1} = s/c_{f2}$)	=	$\begin{pmatrix} 5.33e-2 & 0 & 0 \\ 0 & 5.486e-2 & 0 \\ 0 & 0 & 5.193e-2 \end{pmatrix}$
$\mathbf{K_p}$ ($s/c_1 = s/c_{f1} = s/c_{f2}$)	=	$\begin{pmatrix} 2.865e-4 & 0 & 0 \\ 0 & 2.865e-4 & 0 \\ 0 & 0 & 2.865e-4 \end{pmatrix}$

Table 5.III. Control Law Gain Matrices.

Table 5.IV shows the state vectors $\vec{x} = \left[\omega_x \omega_y \omega_z \, q_0 \, q_1 \, q_2 \, q_3\right]^T$ of the nonlinear state space model for the formation flying spacecraft's rotational movement (refer to equations (3.16)-(3.18)) at time t = 0.

Initial Conditions	s/c_1	s/c_{f1}	s/c_{f2}
ω_x	>0.0001	>0.0001	>0.0001
ω_y	>0.0001	>0.0001	>0.0001
ω_z	>0.0001	>0.0001	>0.0001
q_0	1	1	1
q_1	0	0	0
q_2	0	0	0
q_3	0	0	0

Table 5.IV. Initial States for the Formation Flying Spacecraft.

By means of Magnetometers, Gyroscopes and Autonomous Formation Flying (AFF) sensors, spacecraft s/c_{f1} and s/c_{f2} can measure all the variables needed for the formation flying attitude control system. The number of pulses generated by each PPT and the instant (time) when pulses are generated is recorded by each spacecraft. This operational register is a three-state signal where "+1" represents a pulse generated in the positive direction of the *i-th* axis and "-1" represents a pulse in the negative direction. No pulses are represented by state "0". Table 5.V shows the set of signals used by our approach.

${}^{follower,j}_{leader}q_1$	:	angular rotation about the x-axis ($s/c_{f,j}$ w.r.t. s/c_l)
${}^{follower,j}_{leader}q_2$	:	angular rotation about the y-axis ($s/c_{f,j}$ w.r.t. s/c_l)
${}^{follower,j}_{leader}q_3$	:	angular rotation about the z-axis ($s/c_{f,j}$ w.r.t. s/c_l)
${}^{follower,j}_{leader}\Delta\omega_x$	:	angular velocity about the x-axis ($s/c_{f,j}$ w.r.t. s/c_l)
${}^{follower,j}_{leader}\Delta\omega_y$	:	angular velocity about the y-axis ($s/c_{f,j}$ w.r.t. s/c_l)
${}^{follower,j}_{leader}\Delta\omega_z$	:	angular velocity about the z-axis ($s/c_{f,j}$ w.r.t. s/c_l)
${}^{follower,j}_{leader}T_{PPT1/PPT2}$	:	sequence of pulses about the x-axis ($s/c_{f,j}$ w.r.t. s/c_l)
${}^{follower,j}_{leader}T_{PPT3/PPT4}$	:	sequence of pulses about the y-axis ($s/c_{f,j}$ w.r.t. s/c_l)
${}^{follower,j}_{leader}T_{PPT5/PPT6}$	:	sequence of pulses about the z-axis ($s/c_{f,j}$ w.r.t. s/c_l)

Table 5.V. Data Set for the Formation Flying FDI System.

From the control point of view, the goal of formation flying control law defined in Section 3.4.1 is that the angular rotations and velocities of the spacecraft s/c_{f1} and s/c_{f2} track a set of angular rotations and velocities reference values. Table 5.VI shows the expected t_s and e_{track} values that are used to evaluate the performance of the formation flying control law. The simulations that are performed in this chapter have a final simulation time (t_{final}) of 3000 sec.

Variable	Settling Time (t_s)	Tracking Error ($e_{track}(t_{final})$)
${}^{follower,1}_{leader}q_1$	< 1000 sec	6.00e-3
${}^{follower,1}_{leader}q_2$	< 1000 sec	6.00e-3
${}^{follower,1}_{leader}q_3$	< 1000 sec	6.00e -3
${}^{follower,1}_{leader}\Delta\omega_x$	< 1000 sec	6.00e -5
${}^{follower,1}_{leader}\Delta\omega_y$	< 1000 sec	6.00e -5
${}^{follower,1}_{leader}\Delta\omega_z$	< 1000 sec	6.00e -5

Table 5.VI. Expected Settling Time and Tracking Error Values for s/c_{f1} and s/c_{f2}.

The faulty cases described in Chapter 4 are used to simulate different faulty scenarios although the actuator telemetry data such as discharge current and capacitor voltage are not included in our work.

5.2 Formation Flying Simulation Results

The set of initial and reference conditions as given by equation (5.1) are now used for simulations representing healthy and three faulty scenarios considered. In Euler angle representation, the maneuver considered implies that initially, s/c_{f1} and s/c_{f2} have the same attitude as the leader ([*roll*, *pitch*, *yaw*] = [0°, 0°, 0°]) and no angular velocities (${}^{follower,j}_{leader}\Delta\vec{\omega} = 0$) in any of the axes. After the maneuver, s/c_{f1} and s/c_{f2} must stop their rotations at [*roll*, *pitch*, *yaw*] = [20°, 30°, 40°]. In summary,

$$\left.\begin{aligned} &{}^{follower,j}_{leader}q_0 = 1 \\ &{}^{follower,j}_{leader}q_1 = {}^{follower,j}_{leader}q_2 = {}^{follower,j}_{leader}q_3 = 0 \\ &{}^{follower,j}_{leader}\Delta\omega_x = {}^{follower,j}_{leader}\Delta\omega_y = {}^{follower,j}_{leader}\Delta\omega_z = 0 \end{aligned}\right\} \textit{initial conditions}$$

$$\left.\begin{aligned} &{}^{follower,j}_{leader}q_0 = 0.9093;\ {}^{follower,j}_{leader}q_1 = 0.0704 \\ &{}^{follower,j}_{leader}q_2 = 0.2969;\ {}^{follower,j}_{leader}q_3 = 0.2831 \\ &{}^{follower,j}_{leader}\Delta\omega_x = {}^{follower,j}_{leader}\Delta\omega_y = {}^{follower,j}_{leader}\Delta\omega_z = 0 \end{aligned}\right\} \textit{reference conditions} \qquad (5.1)$$

5.2.1 Simulations for the Healthy Scenario

Healthy scenario implies that the six PPT thrusters of s/c_{f1} and s/c_{f2} are working properly during the commanded maneuver. Figures 5.1 (a)–(b) show the angular rotation, angular velocities and the sequence of pulses in the three axes of s/c_{f1}.

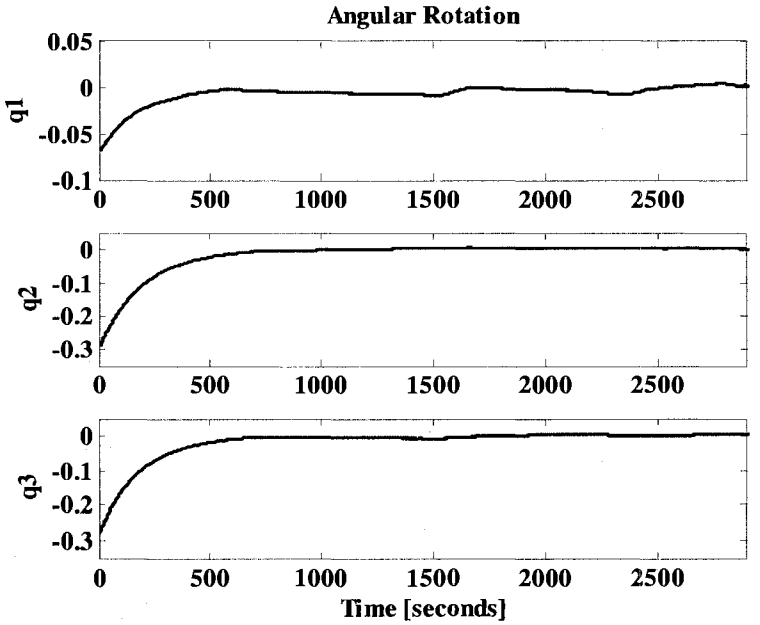

Figure 5.1. (a) Angular Rotation (in quaternion) of s/c_{f1} w.r.t. s/c_1 (Healthy Scenario).

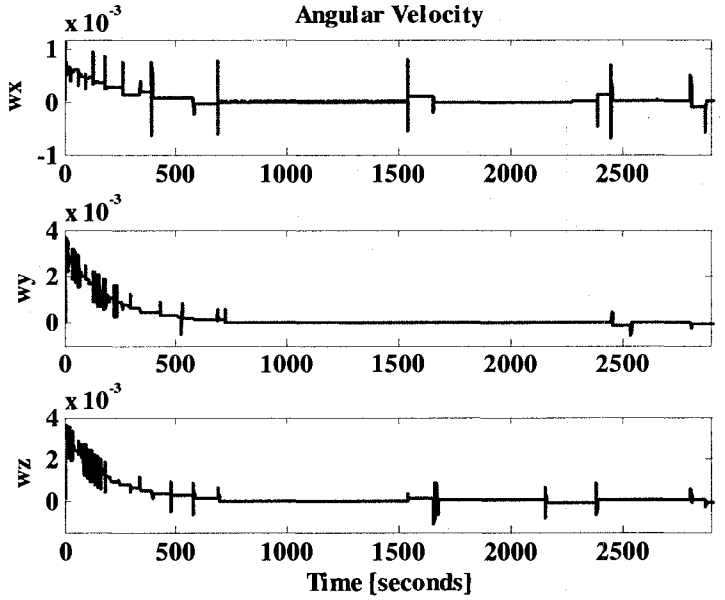

Figure 5.1. (b) Angular Velocity (in degree/seconds) of s/c_{f1} w.r.t. s/c_1 (Healthy Scenario).

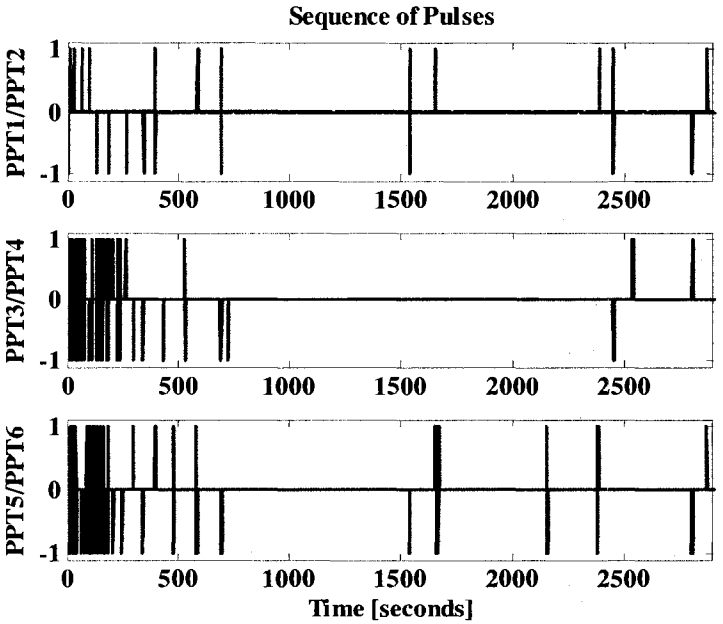

Figure 5.1. (c) Sequence of the Pulses (+1/0/-1 states) of s/c_{f1} w.r.t. s/c_l (Healthy Scenario).

Tracking errors, settling times and the number of generated pulses for s/c_{f1} are shown in Table 5.VII. Since s/c_{f1} and s/c_{f2} are identical spacecraft, the results of the above simulation are also valid for s/c_{f2}.

Variable	Settling Time	Tracking Error	Number of Pulses
${}^{follower,l}_{leader}q_1$	$t_s = 500$	$e_{track} = 1.55e\text{-}3$	N/A
${}^{follower,l}_{leader}q_2$	$t_s = 800$	$e_{track} = 1.30e\text{-}3$	N/A
${}^{follower,l}_{leader}q_3$	$t_s = 650$	$e_{track} = 2.00e\text{-}3$	N/A
${}^{follower,l}_{leader}\Delta\omega_x$	$t_s = 500$	$e_{track} = 2.80e\text{-}5$	N/A
${}^{follower,l}_{leader}\Delta\omega_y$	$t_s = 800$	$e_{track} = 3.50e\text{-}5$	N/A
${}^{follower,l}_{leader}\Delta\omega_z$	$t_s = 650$	$e_{track} = 1.85e\text{-}5$	N/A
${}^{follower,l}_{leader}T_{PPT1/PPT2}$	N/A	N/A	T_{PPT1}=26 / T_{PPT2}=31
${}^{follower,l}_{leader}T_{PPT3/PPT4}$	N/A	N/A	T_{PPT3}=78 / T_{PPT4}=68
${}^{follower,l}_{leader}T_{PPT5/PPT6}$	N/A	N/A	T_{PPT5}=57 / T_{PPT6}=76

Table 5.VII. Data Set for s/c_{f1} Under Healthy Scenario.

Based on the expected settling times and tracking errors (refer to Table 5.VI) and the results shown in Table 5.VII, one can conclude that the performance of the formation flying system fulfills the requirements of accuracy and precision.

5.2.2 Simulations for the Faulty Scenario 1

Due to the loss of elasticity in the spring of the thruster PPT_1, the amount of force produced by the actuator is reduced by 15 %. Figures 5.2 (a)–(c) show the results obtained from s/c_{f1} acting under this faulty scenario.

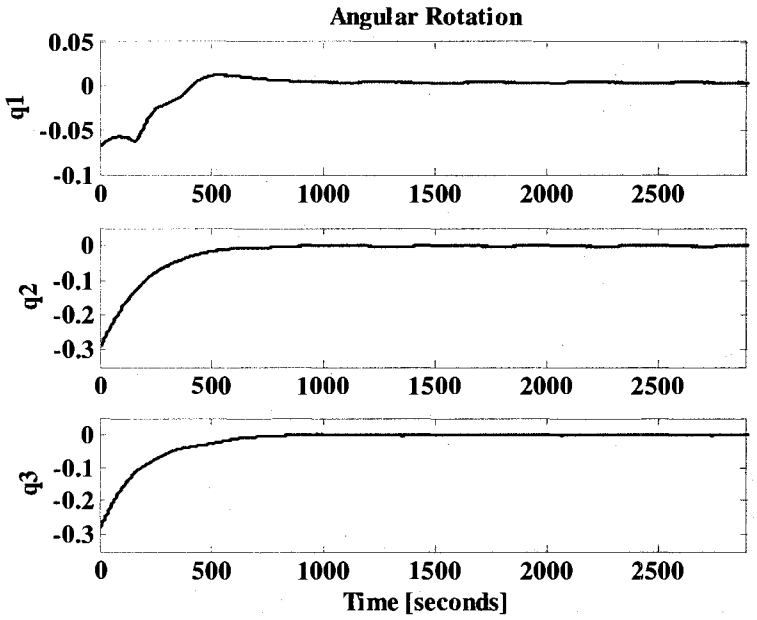

Figure 5.2. (a) Angular Rotation (in quaternion) of s/c_{f1} w.r.t. s/c_1 (Faulty Scenario 1).

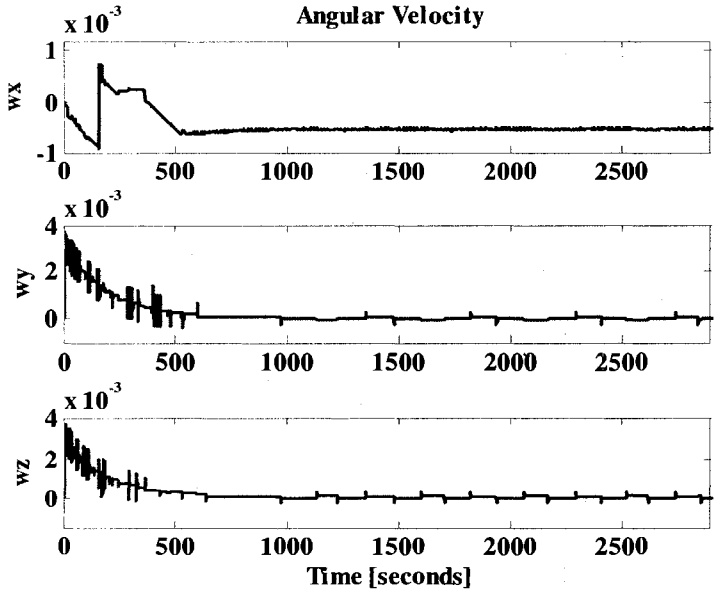

Figure 5.2. (b) Angular Velocity (in degree/seconds) of s/c_{f1} w.r.t. s/c_1 (Faulty Scenario 1).

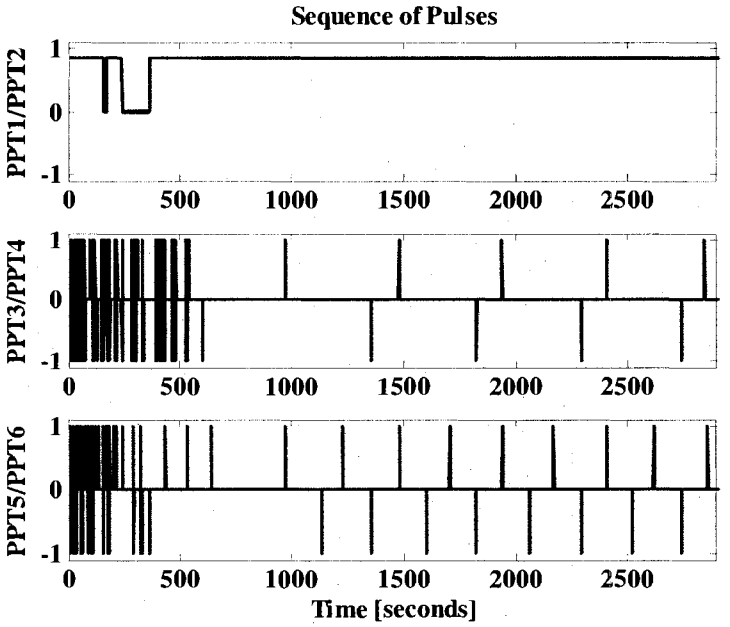

Figure 5.2. (c) Sequence of the Pulses (+1/0/-1 states) of s/c_{f1} w.r.t. s/c_l (Faulty Scenario 1).

Table 5.VIII shows the performance parameters for s/c_{f1} under the Faulty scenario 1 conditions. Follower s/c_{f2} is not subjected to a faulty actuator, therefore its results are the same as the healthy case (Table 5.VII).

Variable	Settling Time	Tracking Error	Number of Pulses
${}^{follower,1}_{leader}q_1$	$t_s = 900$	$e_{track} = 3.00e\text{-}3$	N/A
${}^{follower,1}_{leader}q_2$	$t_s = 1000$	$e_{track} = 2.00e\text{-}3$	N/A
${}^{follower,1}_{leader}q_3$	$t_s = 850$	$e_{track} = 0.50e\text{-}3$	N/A
${}^{follower,1}_{leader}\Delta\omega_x$	$t_s = 800$	$e_{track} = 5.25e\text{-}4$	N/A
${}^{follower,1}_{leader}\Delta\omega_y$	$t_s = 600$	$e_{track} = 3.00e\text{-}5$	N/A
${}^{follower,1}_{leader}\Delta\omega_z$	$t_s = 650$	$e_{track} = 5.50e\text{-}5$	N/A
${}^{follower,1}_{leader}T_{PPT1/PPT2}$	N/A	N/A	T_{PPT1}=3871 /T_{PPT2}=0
${}^{follower,1}_{leader}T_{PPT3/PPT4}$	N/A	N/A	T_{PPT3}=113 /T_{PPT4}=96
${}^{follower,1}_{leader}T_{PPT5/PPT6}$	N/A	N/A	T_{PPT5}=77 / T_{PPT6}=49

Table 5.VIII. Data Set for s/c_{f1} Under Faulty Scenario 1.

Based on the expected settling times and tracking errors (refer to Table 5.VI) and the results shown in Table 5.VIII, one can conclude that the performance of the formation flying system fulfills the requirements of accuracy and precision.

5.2.3 Simulations of the Faulty Scenario 2

For this faulty scenario we assume that in the case of PPT_1 the accumulation of particles (sedimentation) may produce force pulses 15% greater than the nominal values. Figures 5.3 (a)–(c) show the s/c_{f1} simulations for this case.

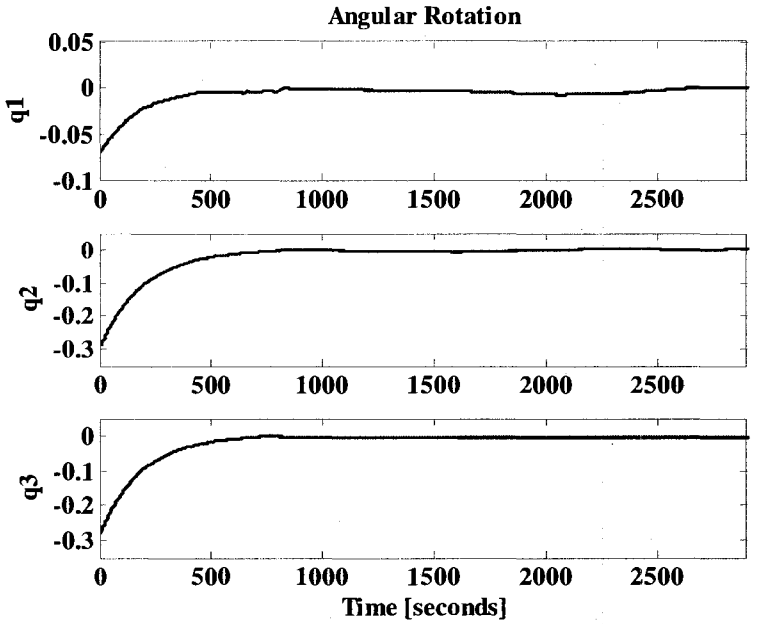

Figure 5.3. (a) Angular Rotation (in quaternion) of s/c_{f1} w.r.t. s/c_1 (Faulty Scenario 2).

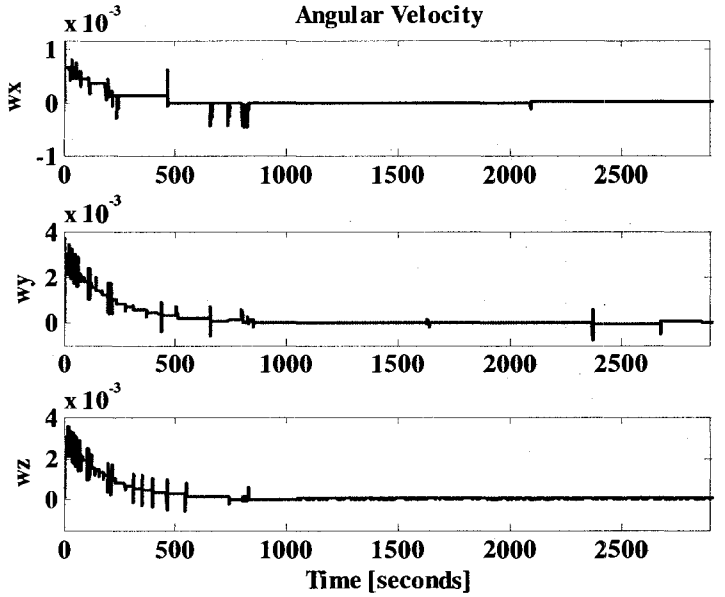

Figure 5.3. (b) Angular Velocity (in degree/seconds) of s/c_{f1} w.r.t. s/c_1 (Faulty Scenario 2).

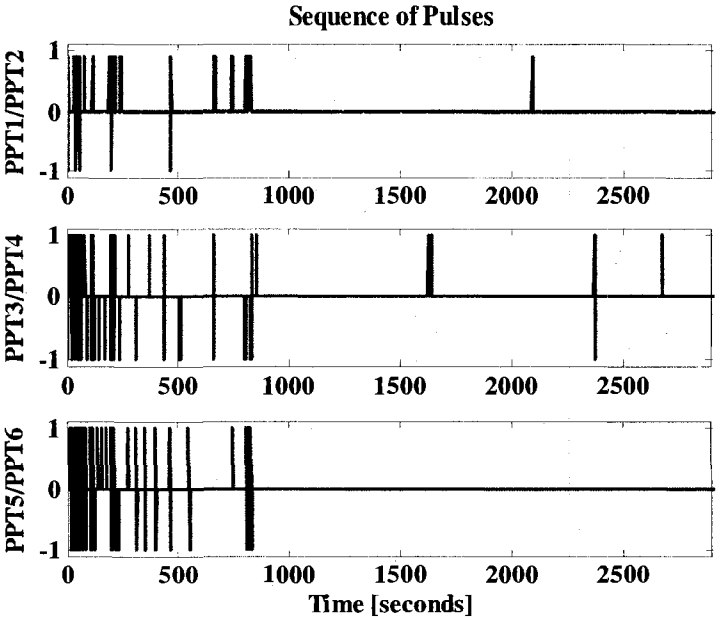

Figure 5.3. (c) Sequence of the Pulses (+1/0/-1 states) of s/c_{f1} w.r.t. s/c_l (Faulty Scenario 2).

The performance parameters for s/c_{f1} under the Faulty scenario 2 conditions are shown in Table 5.VIX. Since the follower s/c_{f2} is not subjected to faulty actuators therefore the results are the same as that of the healthy case (Table 5.VII).

Variable	Settling Time	Tracking Error	Number of Pulses
${}^{follower,l}_{leader}q_1$	$t_s = 830$	$e_{track} = 0.40e\text{-}3$	N/A
${}^{follower,l}_{leader}q_2$	$t_s = 850$	$e_{track} = 3.00e\text{-}3$	N/A
${}^{follower,l}_{leader}q_3$	$t_s = 950$	$e_{track} = 7.50e\text{-}3$	N/A
${}^{follower,l}_{leader}\Delta\omega_x$	$t_s = 470$	$e_{track} = 2.30e\text{-}5$	N/A
${}^{follower,l}_{leader}\Delta\omega_y$	$t_s = 850$	$e_{track} = 3.00e\text{-}5$	N/A
${}^{follower,l}_{leader}\Delta\omega_z$	$t_s = 745$	$e_{track} = 1.00e\text{-}5$	N/A
${}^{follower,l}_{leader}T_{PPT1/PPT2}$	N/A	N/A	T_{PPT1}=105 /T_{PPT2}=23
${}^{follower,l}_{leader}T_{PPT3/PPT4}$	N/A	N/A	T_{PPT3}=88 /T_{PPT4}=87
${}^{follower,l}_{leader}T_{PPT5/PPT6}$	N/A	N/A	T_{PPT5}=64 / T_{PPT6}=71

Table 5.VIX. Data Set for s/c_{f1} Under Faulty Scenario 2.

Based on the expected settling times and tracking errors (refer to Table 5.VI) and the results shown in Table 5.VIX, one can conclude that the performance of the formation flying system fulfills the requirements of accuracy and precision.

5.2.4 Simulations for the Faulty Scenario 3

The thruster's electric components may suffer from conductivity problems which could lead to a reduction in the amount of thrust produced. A conductivity fault in the thruster PPT_1 of s/c_{f1} which reduces the thrust by 15% is simulated. Figures 5.4 (a)–(c) show the simulation results.

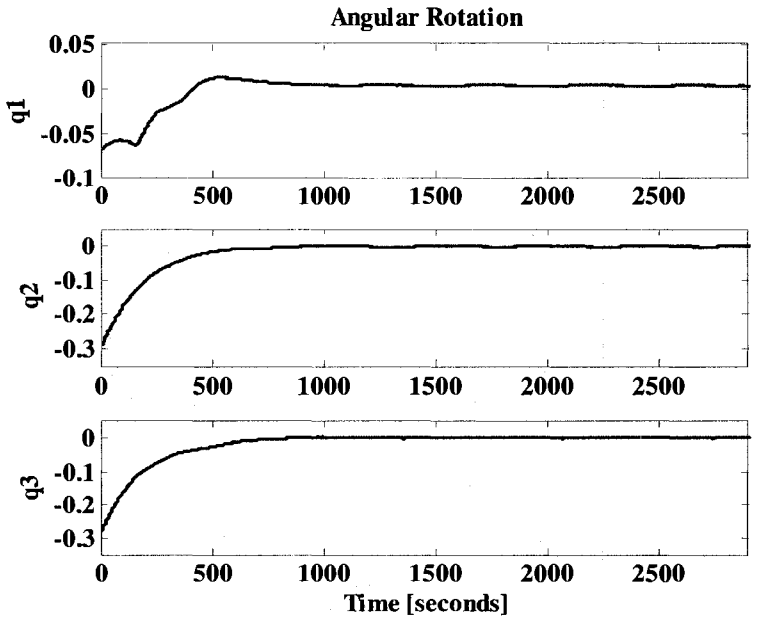

Figure 5.4. (a) Angular Rotation (in quaternion) of s/c_{f1} w.r.t. s/c_1 (Faulty Scenario 3).

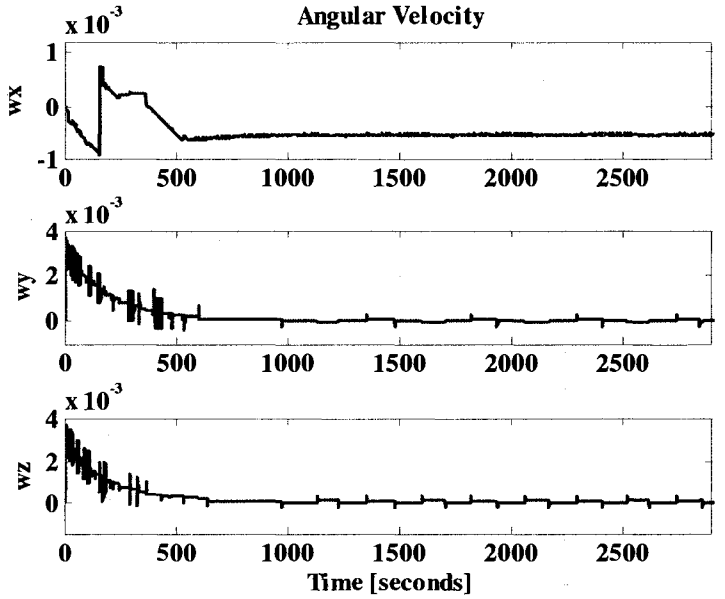

Figure 5.4. (b) Angular Velocity (in degree/seconds) of s/c_{f1} w.r.t. s/c_1 (Faulty Scenario 3).

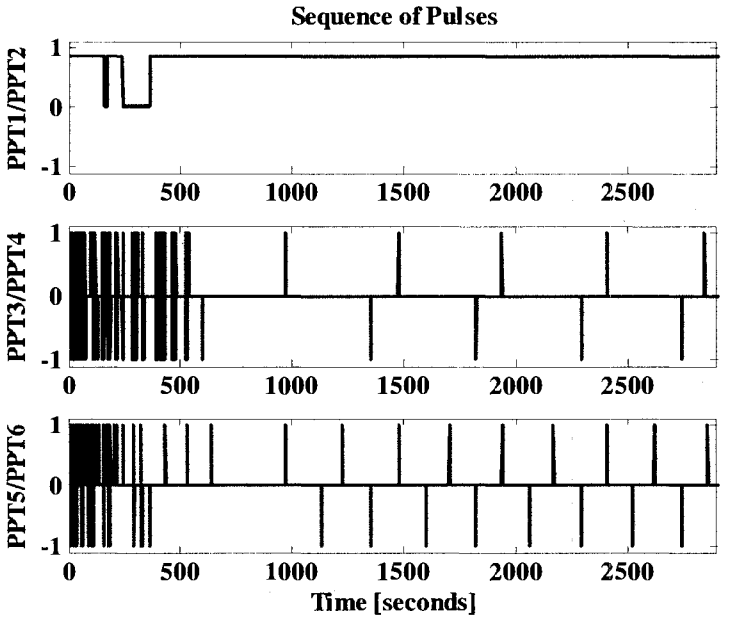

Figure 5.4. (c) Sequence of the Pulses (+1/0/-1 states) of s/c_{fl} w.r.t. s/c_l (Faulty Scenario 3).

Table 5.VX shows the performance parameters for s/c_{fl} under the Faulty scenario 3 condition.

Variable	Settling Time	Tracking Error	Number of Pulses
${}^{follower,l}_{leader}q_1$	$t_s = 900$	$e_{track} = 3.00e\text{-}3$	N/A
${}^{follower,l}_{leader}q_2$	$t_s = 1000$	$e_{track} = 2.00e\text{-}3$	N/A
${}^{follower,l}_{leader}q_3$	$t_s = 850$	$e_{track} = 0.50e\text{-}3$	N/A
${}^{follower,l}_{leader}\Delta\omega_x$	$t_s = 800$	$e_{track} = 5.25e\text{-}4$	N/A
${}^{follower,l}_{leader}\Delta\omega_y$	$t_s = 600$	$e_{track} = 3.00e\text{-}5$	N/A
${}^{follower,l}_{leader}\Delta\omega_z$	$t_s = 650$	$e_{track} = 5.50e\text{-}5$	N/A
${}^{follower,l}_{leader}T_{PPT1/PPT2}$	N/A	N/A	T_{PPT1}=3871 /T_{PPT2}=0
${}^{follower,l}_{leader}T_{PPT3/PPT4}$	N/A	N/A	T_{PPT3}=113 /T_{PPT4}=96
${}^{follower,l}_{leader}T_{PPT5/PPT6}$	N/A	N/A	T_{PPT5}=77 / T_{PPT6}=49

Table 5.X. Data set for s/c_{fl} Under Faulty Scenario 3.

Based on the expected settling times and tracking errors (refer to Table 5.VI) and the results shown in Table 5.VX, one can conclude that the performance of the formation flying system fulfills the requirements of accuracy and precision.

From the above four simulations we can conclude the following:

- Low severity faults (~ 15%) do not affect the performance of the formation flying system,

meaning that although there is a faulty thruster, the precision that are required can be achieved by increasing the number of pulses generated by the thrusters. This characteristic suggests that the number of pulses generated by each thruster is a relevant variable.

- Although the fault scenarios 1 and 3 are different (different fault causes) the results shown in the figures and the tables provided are the same. The reason being that from relative attitude control point of view the cause of the faulty actuator is not observable. What actually matters is the effect (reduction in the amount of thrust) that the fault produces.
- From the three faulty scenarios we can observe that a spacecraft with an actuator suffering a low severity fault (15%) can still perform corrective maneuvers, and the reference relative attitude can still be reached but with different tracking errors and settling times in all the attitude variables. The faulty actuator produces changes in the number and the sequence of the generated pulses in the six thrusters.

5.3 Design of the Neural Network FDI Scheme

Following the motivations that have been explained in Chapter 4 and due to the promising results obtained in that chapter, dynamic neural networks are used as engine of our proposed FDI system based on the formation flying relative attitude control subsystem. Details on the structure of the dynamic neural model, the neuron's dynamic model and the Extended Dynamic Back Propagation (EDBP) training algorithm are given in Section 4.3. Specifically, we implement an FDI system that is composed of three Dynamic Neural Networks (DNNs). Figure 5.5 shows the schematic representation of the proposed DNN that is used for the roll angle during the training phase. This schematic representation also describes the proposed DNNs that are used for the pitch and yaw angles. The figure shows a three level system: Leader attitude control subsystem (ACS), follower 1 attitude control subsystem (ACS) and FDI scheme for the roll angle of the follower 1.

As explained in Chapter 3, Section 3.4.1, the leader spacecraft corrects its angular rotations and velocities according to a set of reference values (i.e. expected angular rotations and

velocities). On the other hand, the followers use the angular rotations and velocities of the leader to perform control attitude actions. The proposed FDI scheme for the followers uses relative angular rotations and velocities.

Each DNN has a 4-10-1 structure (four neurons in the input layer, ten neurons in the hidden layer and one neuron in the output layer) with second order Infinite Impulse Response (IIR) filters and hyperbolic tangent sigmoid and linear activation functions for the neurons in the hidden and output layers, respectively. Table 5.XI contains the details regarding the three networks.

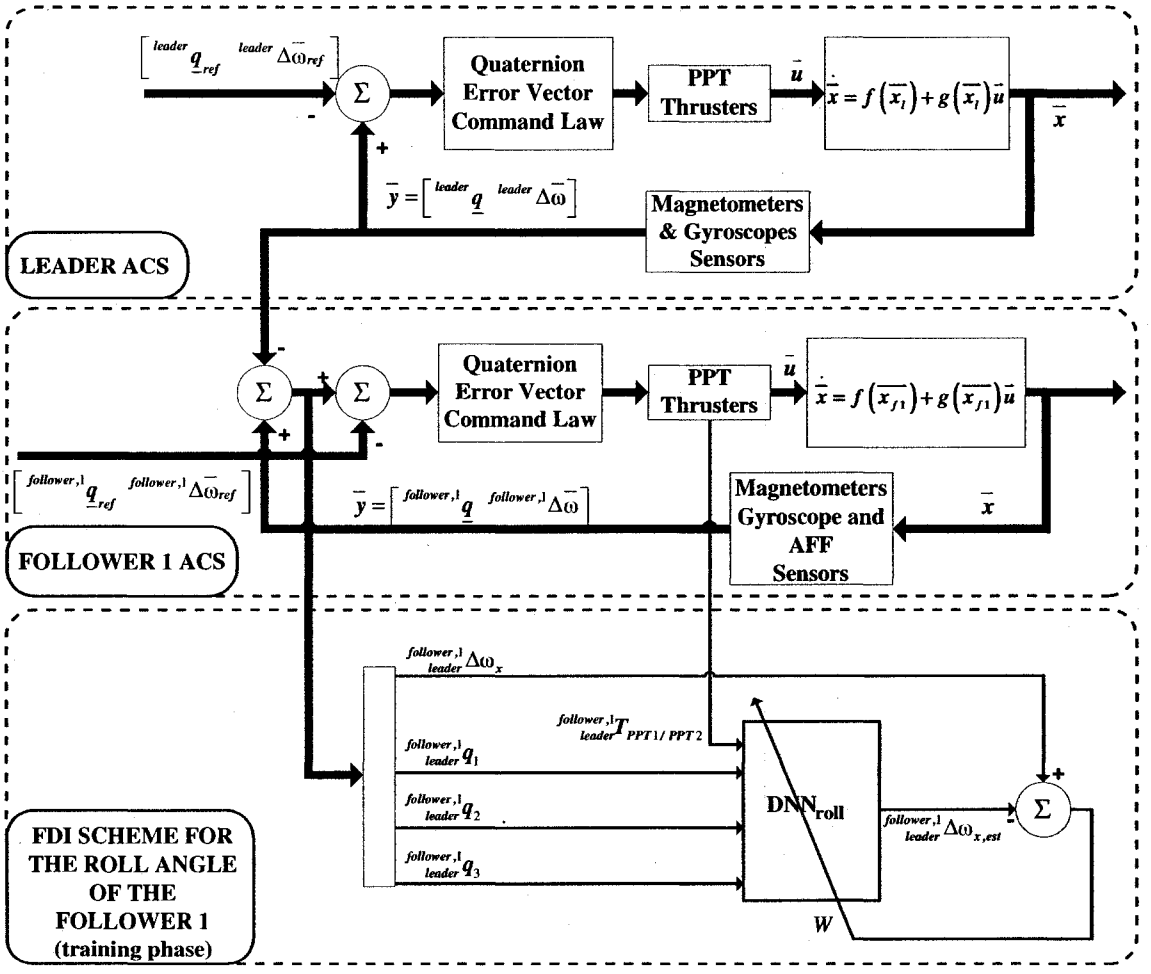

Figure 5.5. Identification Model During the Training Phase.

DNN_{roll} (Roll)	DNN_{pitch} (Pitch)	DNN_{yaw} (Yaw)
u_1: ${}^{follower,j}_{leader}T_{PPT1/PPT2}$	u_1: ${}^{follower,j}_{leader}T_{PPT3/PPT4}$	u_1: ${}^{follower,j}_{leader}T_{PPT5/PPT6}$
u_2: ${}^{follower,j}_{leader}q_1$	u_2: ${}^{follower,j}_{leader}q_1$	u_2: ${}^{follower,j}_{leader}q_1$
u_3: ${}^{follower,j}_{leader}q_2$	u_3: ${}^{follower,j}_{leader}q_2$	u_3: ${}^{follower,j}_{leader}q_2$
u_4: ${}^{follower,j}_{leader}q_3$	u_4: ${}^{follower,j}_{leader}q_3$	u_4: ${}^{follower,j}_{leader}q_3$
y_{est}: ${}^{follower,j}_{leader}\Delta\omega_{x,est}$	y_{est}: ${}^{follower,j}_{leader}\Delta\omega_{y,est}$	y_{est}: ${}^{follower,j}_{leader}\Delta\omega_{z,est}$

Table 5.XI. Input/Output Data Set for the Three Networks.

From Table 5.VXI one can see that each DNN estimates the angular velocity of one of the three axes of the spacecraft, specifically DNN_{roll}, DNN_{pitch} and DNN_{yaw} estimate the angular velocity in the *x-axis*, *y-axis* and *z-axis*, respectively. For training purposes, we collect data from three different simulated missions. Starting with the same initial conditions as shown in equation (5.1), the simulated missions require the followers to rotate until they reach the following desirable attitude, namely the first mission is ([25°, 40°, 55°]), the second mission is ([20°, 45°, 60°]), and the third mission ([35°, 45°, 55°]). Table 5.XII shows the references that are expressed in quaternions.

Mission 1	Mission 2	Mission 3
$q_0 = 0.8479$	$q_0 = 0.8212$	$q_0 = 0.8347$
$q_1 = 0.02622$	$q_1 = -0.0495$	$q_1 = 0.0779$
$q_2 = 0.3901$	$q_2 = 0.4066$	$q_2 = 0.452$
$q_3 = 0.358$	$q_3 = 0.3974$	$q_3 = 0.3048$

Table 5.XII. References (in Quaternion Representation) for the Missions 1, 2 and 3.

Each DNN is trained until a termination criterion is fulfilled. In this case, the termination criterion (*t.c.*) that is used is the mean square error (*mse*) criterion. Figures 5.6 and 5.7 show the actual angular velocities and the corresponding estimations that are generated by the DNNs subject to mission 1 requirements.

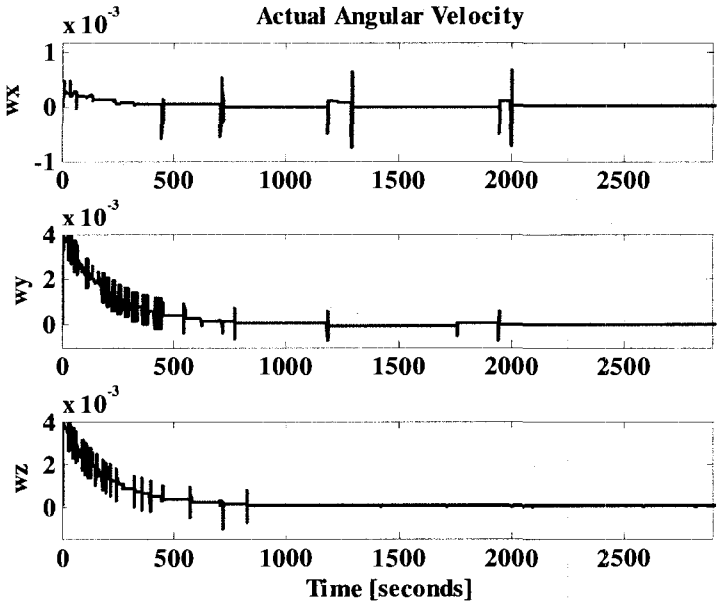

Figure 5.6. Actual Angular Velocity During Mission 1.

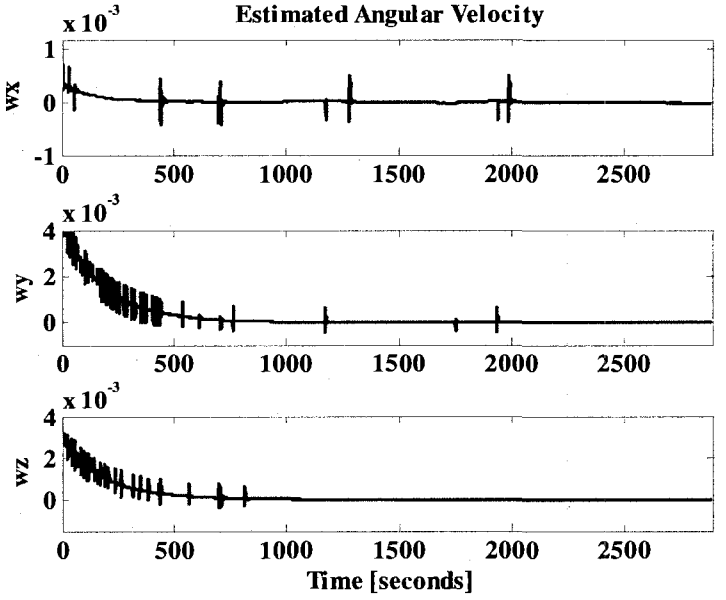

Figure 5.7. Estimated Angular Velocity During Mission 1.

After the training phase is completed, the parameters of the dynamic neural networks are fixed and the validation phase is initiated. A set of data is applied to the DNNs and their modeling performance is studied. Figure 5.8 shows the architecture of the DNN used for the roll angle during the validation phase.

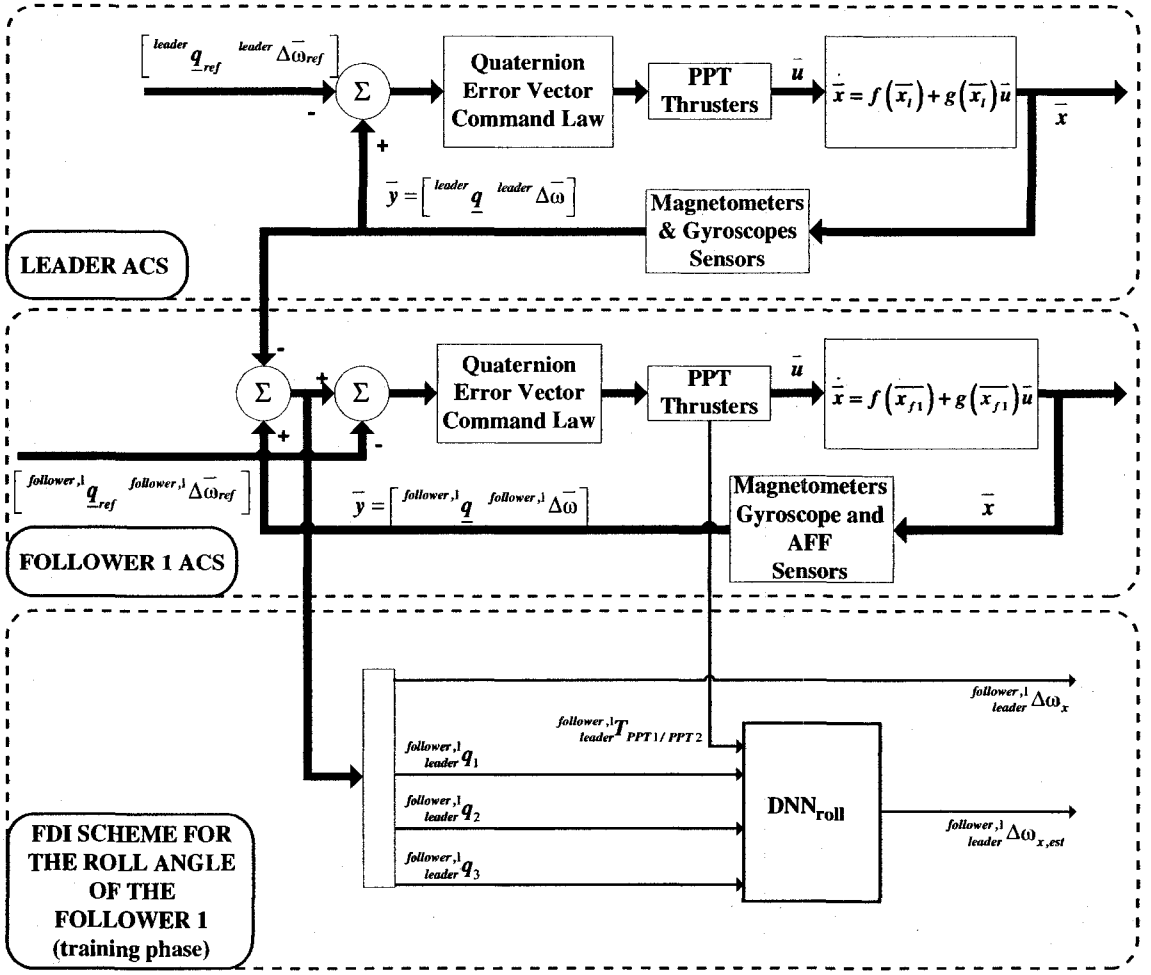

Figure 5.8. Identification Model During the Validation Phase.

Similar to the procedure performed in the training phase, in the validation phase we simulate three missions. According to the initial conditions (equation (5.1)) the followers must rotate until they reach the following desirable attitudes: for the fourth mission ([30°, 40°, 50°]), for the fifth mission ([30°, 45°, 55°]), and for the sixth mission ([35°, 50°, 60°]). Table 5.XIII shows the references that are expressed in the quaternions.

Mission 4	Mission 5	Mission 6
$q_0 = 0.86$	$q_0 = 0.8373$	$q_0 = 0.8121$
$q_1 = 0.0808$	$q_1 = 0.04142$	$q_1 = 0.03449$
$q_2 = 0.4022$	$q_2 = 0.4383$	$q_2 = 0.4853$
$q_3 = 0.3034$	$q_3 = 0.3242$	$q_3 = 0.3221$

Table 5.XIII. References (in Quaternion Representation) for the Missions 4, 5 and 6.

The modeling capability of our DNN approach is illustrated in Figures 5.9 – 5.10. In these figures we depict the actual angular velocity and the corresponding estimation that is achieved by

the neural networks for the mission case 5.

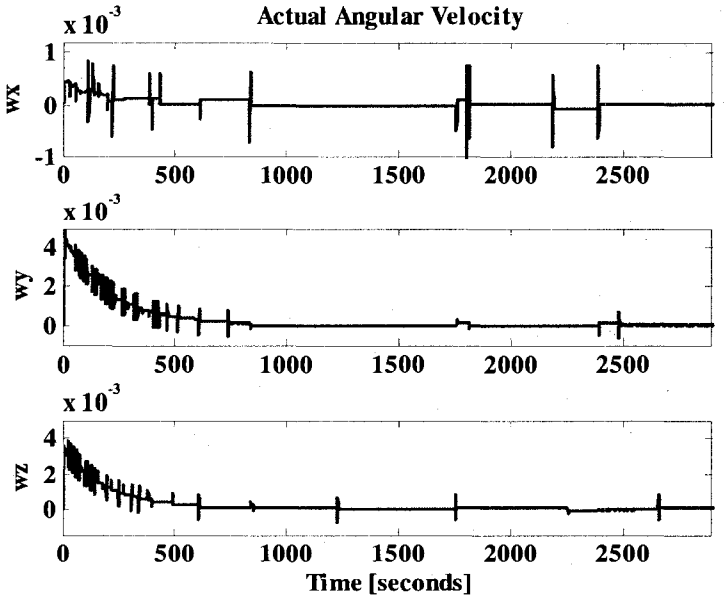

Figure 5.9. Actual Angular Velocity During Mission 5.

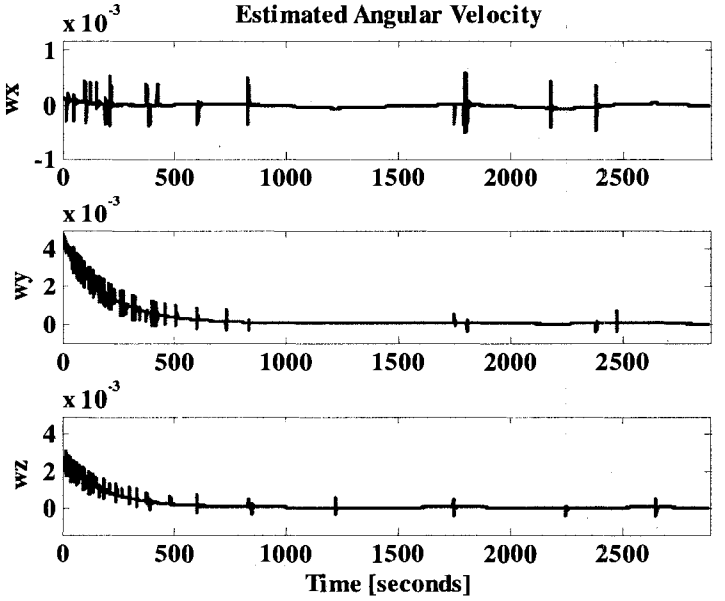

Figure 5.10. Estimated Angular Velocity During Mission 5.

The data set generated from the missions 1–6 include only the healthy data, therefore the selection of a fixed *Threshold* value is achieved according to these data. Similar to our FDI approach in the previous chapter, the *Threshold* is used to determine the health condition of the spacecraft during the maneuvers in a mission. For the complete FDI system we need three different *Thresholds*, one for each DNN. Consequently, each DNN with a fixed *threshold* can

determine the behavior of a pair of thrusters as being healthy or faulty. The calculation of the *threshold* (refer to equation (4.2)) that is used by the FDI scheme proposed in Chapter 4, utilizes the Mean Absolute Error (*MAE*). As shown in equation (5.2), the proposed FDI scheme utilizes the Sum of Absolute Error (*SAE*) from the expected settling time (t_s) to the final time (t_{final}).

$$SAE_{roll} := \sum_{k=t_s}^{t_{final}} \left(\left| {}^{follower,1}_{leader}\Delta\omega_x(k) - {}^{follower,1}_{leader}\Delta\omega_{x,est}(k) \right| \right); \quad t_s = 1000, \quad t_{final} = 3000 \tag{5.2}$$

By using equation (5.3), the $Threshold_{roll}$ value for DNN_{roll} is determined. The coefficient σ_{roll} is a constant which is used to adjust the healthy/faulty classification for the DNN_{roll}.

$$Threshold_{roll} = \frac{\sum_{l=1}^{6} SAE_{roll}(l)}{6} + \sigma_{roll} \left(max(SAE_{roll}(l))_{l=1}^{6} - \frac{\sum_{l=1}^{6} SAE_{roll}(l)}{6} \right) \tag{5.3}$$

where *l* represents the *l-th* mission (i.e. for the calculation of the Threshold values, the *SAE* values of the six missions were utilized). The procedure for determining the *Threshold* value for the other two DNN (i.e. DNN_{pitch} and DNN_{yaw}) is the same than the one used for DNN_{roll}. Table 5.XIV shows the values for σ and the *Threshold* for each DNN.

	DNN_{roll}	DNN_{pitch}	DNN_{yaw}
σ_i	1.208	2.450	1.032
Threshold	135.00	50.00	76.00

Table 5.XIV. Threshold Fixed Values for Our Proposed FDI approach.

The health status of the actuators during a mission is represented by *SAE*. If this value exceeds the Threshold, the corresponding pair of thrusters is considered as being faulty. On the other hand, if *SAE* does not exceeds the Threshold, the pair is considered as a healthy pair. The schematic of our proposed DNN based FDI scheme is now shown in Figure 5.11. The input data set $\left[u_1^i \; u_2^i \; u_3^i \; u_4^i\right]^T$ is normalized before being presented to the DNN. Using the normalized actual output $y_{i,actual}(k+1)$ and the output of the network $y_{i,est}(k+1)$, the decision making block compares the *SAE* with the corresponding *Threshold* to detect the health status of the pair of PPTs.

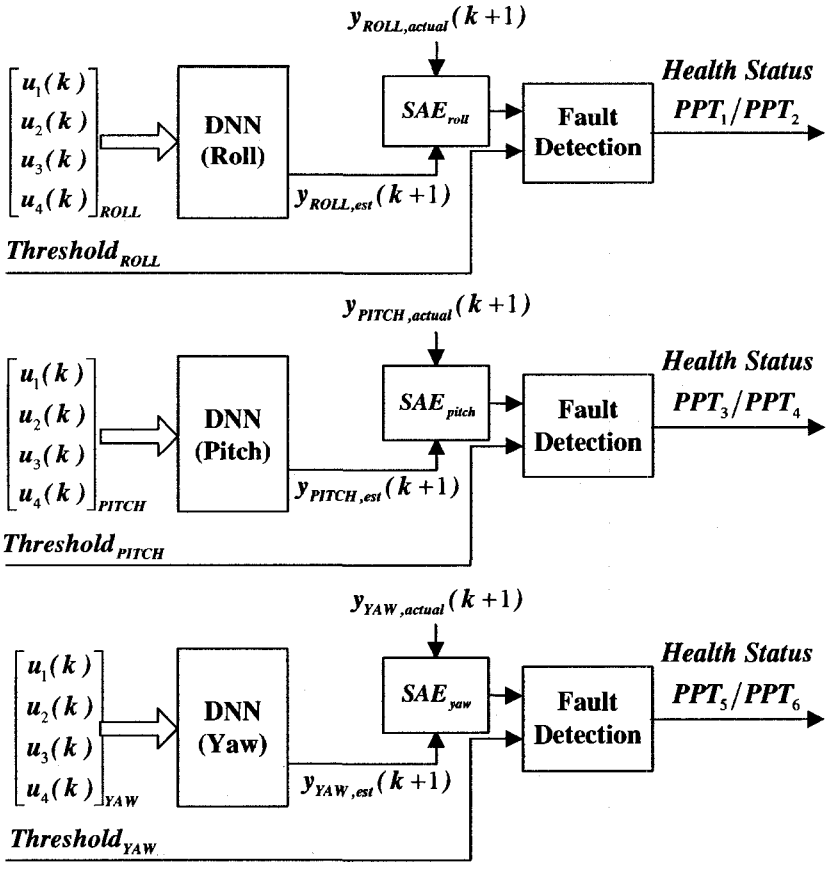

Figure 5.11. FD Scheme for a Follower Spacecraft in a Formation Flying.

5.4. Simulations for the FDI

Our proposed FDI scheme can detect faults which affect the behavior of the relative attitude control. The utilization of three DNN, allows us to identify which pair of the PPT thrusters is the source of a fault.

To investigate the performance of our proposed FDI scheme, we simulate the formation flying system as described in Section 5.2 performing three different rotational maneuvers. The three different fault scenarios considered are the following:

Faulty Scenario 1: From the initial conditions shown in equation (5.1), a desirable angular rotation of [25°, 30°, 40°] must be reached by s/c_{f1} and s/c_{f2}. A mass fault reduction of the thruster PPT_2 of s/c_{f1} is injected at time $t = 0$ seconds (see Faulty Scenario 1 in Section 4.2.2). Equation (5.4) shows the structural changes that are introduced in the experimental system, where

$$m_{0,PPT_1} = \begin{cases} 2.58\times10^{-8} kg; & t \le 0 \\ 3.00\times10^{-9} kg; & t > 0 \end{cases} \tag{5.4}$$

Figure 5.12 shows the real effect that this fault produces on the thruster PPT_2 and Table 5.XV presents the results that are obtained by using our proposed FDI scheme.

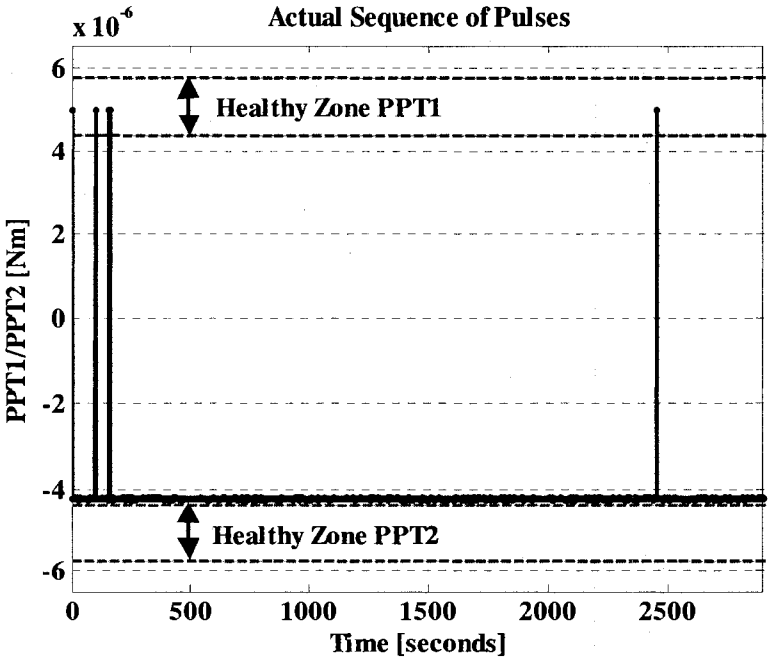

Figure 5.12. Actual Sequence of Pulses Generated by PPT_1/ PPT_2 (Faulty Scenario 1).

The number of pulses that are generated by PPT_1 and PPT_2 are 10 and 2890, respectively. Figure 5.12 shows that the torque produced by PPT_1 is within the healthy zone (~ 5*e*-6 [Nm]), meanwhile PPT_2 generates 2890 faulty pulses (~ 4.7*e*-6 [Nm]). As explained in Chapter 3, Section 3.3.2, PPT_1 and PPT_2 generate torques in the $+x$ and $-x$ axes, respectively.

	SAE_i	$Threshold_i$	$Health\ Status_i$
DNN_{Roll}	**382.12**	135.00	Faulty
DNN_{Pitch}	41.53	50.00	Healthy
DNN_{Yaw}	45.16	76.00	Healthy

Table 5.XV. Health Analysis Results Obtained by Our Proposed FDI Approach Under Faulty Scenario 1.

Additional information can be extracted from the above results. In this case, when the thruster PPT_2 generates less torque than expected, the amount of pulses generated by that actuator is "considerably" higher than the amount of pulses generated by the other actuator (PPT_1).

Faulty Scenario 2: From the initial conditions shown in equation (5.1), a desirable angular rotation of [20°, 35°, 45°] must be reached by s/c_{f1} and s/c_{f2}. A fault due to the accumulation of particles in the inner face of the electrodes of the PPT_3 thruster of s/c_{f1} is injected at time $t = 0$ seconds (see Faulty Scenario 2 in Section 4.2.3). Equation (5.5) shows the structural changes that are introduced in the experimental system, where

$$w_{PPT_3} = \begin{cases} 0.0254m; & t \leq 0 \\ 0.02195m; & t > 0 \end{cases} \tag{5.5}$$

Figure 5.13 shows the real effect that this fault produces on the thruster PPT_3 and Table 5.XVI presents the results that are obtained by using our proposed FDI scheme.

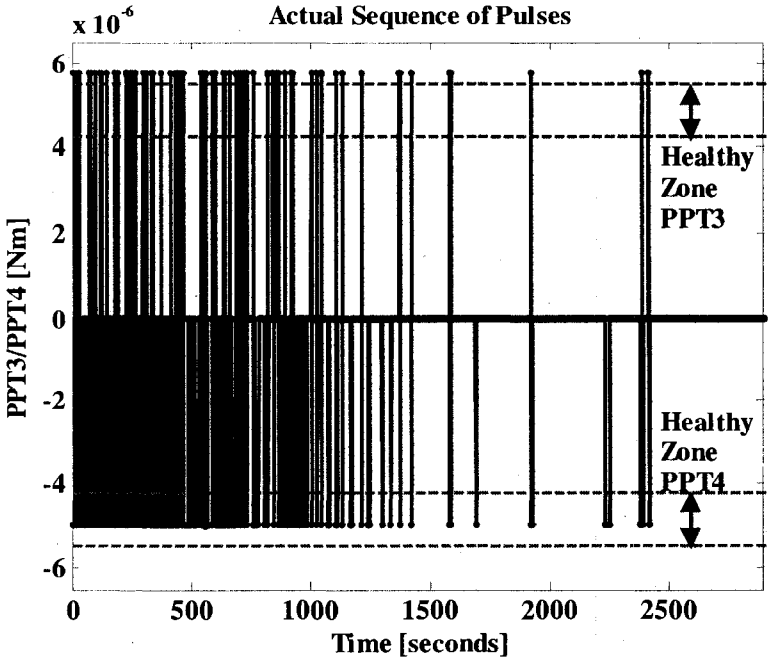

Figure 5.13. Actual Sequence of Pulses Generated by PPT_3/ PPT_4 (Faulty Scenario 2).

The number of pulses that are generated by PPT_3 and PPT_4 are 104 and 577, respectively. Figure 5.13 shows that 104 pulses produced by PPT_3 are faulty (~ 5.8*e*-6 [Nm]), meanwhile the 577 pulses generated by PPT_4 are within the healthy zone (~ 5*e*-6 [Nm]). PPT_3 and PPT_4 generate torques in $+y$ and $-y$ axes, respectively (see Chapter 3, Section 3.3.2).

Based on the results shown in Table 5.XVI, we detect the presence of a fault in the pair of thrusters PPT_3/PPT_4. The other two pairs of thrusters are identified as healthy.

	SAE_i	$Threshold_i$	$Health\ Status_i$
DNN_{Roll}	100.21	135.00	Healthy
DNN_{Pitch}	**57.88**	50.00	Faulty
DNN_{Yaw}	39.75	76.00	Healthy

Table 5.XVI. Health Analysis Results Obtained by Our Proposed FDI Approach Under Faulty Scenario 2.

In this case, a similar analysis to the one conducted for the previous case can also be performed. When the thruster PPT_3 generates more torque than expected, the amount of pulses generated by that actuator is 'considerably' less than the amount of pulses generated by the other actuator (PPT_4).

Faulty Scenario 3: From the initial conditions that are shown in Equation (5.1), a desirable angular rotation of [25°, 35°, 45°] must be reached by s/c_{f1} and s/c_{f2}. Loss of conductivity of electrical components of the PPT_6 thruster of s/c_{f1} generates a fault which is injected at time $t = 0$ seconds (see Faulty Scenario 3 in Section 4.2.4). Equation (5.6) shows the structural changes that are introduced in the experimental system, where

$$R_{pe,PPT_6} = \begin{cases} 0.00\,\Omega; & t \leq 0 \\ 0.08\,\Omega; & t > 0 \end{cases} \tag{5.6}$$

Figure 5.14 shows the real effect that this fault produces on the thruster PPT_6 and Table 5.XVII presents the results that are obtained by using our proposed FDI scheme.

The number of pulses that are generated by PPT_5 and PPT_6 are 2523 and 13, respectively. Figure 5.14 shows that PPT_5 generates 2523 faulty pulses (~ 4.7*e*-6 [Nm]). On the other hand PPT_4 generates 13 healthy pulses (~ 5*e*-6 [Nm]). PPT_5 and PPT_6 generate torques in the $+z$ and $-z$ axes, respectively (see Chapter 3, Section 3.3.2).

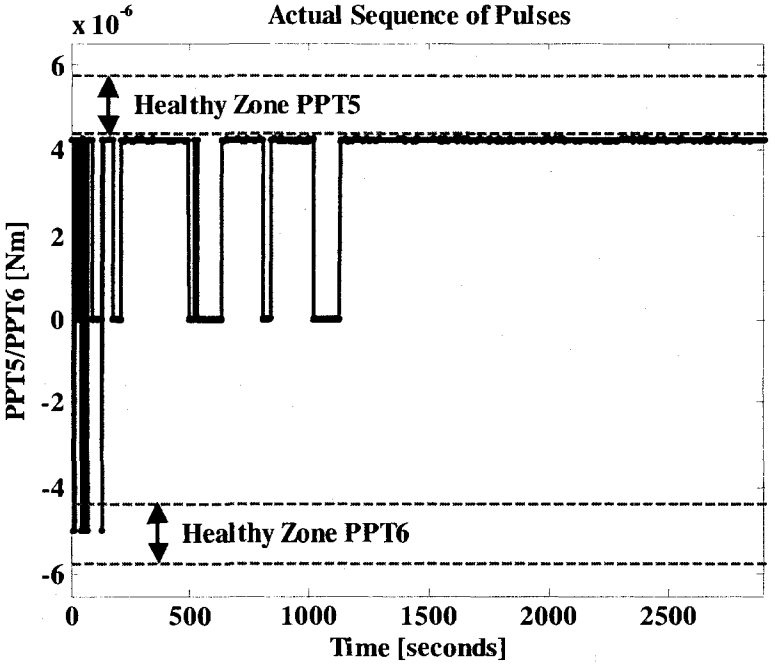

Figure 5.14. Actual Sequence of Pulses Generated by PPT_5/ PPT_6 (Faulty Scenario 3).

Based on the results shown in Table 5.XVII, we detect the presence of a fault in the pair of thrusters PPT_3/PPT_4. The other two pairs of thrusters are identified as healthy.

	SAE_i	$Threshold_i$	$Health\ Status_i$
DNN_{Roll}	132.84	135.00	Healthy
DNN_{Pitch}	38.40	50.00	Healthy
DNN_{Yaw}	**279.98**	76.00	Faulty

Table 5.XVII. Health Analysis Results Obtained by Our Proposed FDI Approach Under Faulty Scenario 3.

Finally, from this simulated faulty scenario, we can see that when thruster PPT_5 generates less torque than expected, the amount of pulses generated by this actuator is 'considerably' higher than the amount of pulses generated by the other actuator (PPT_6).

Based on the number of pulses that are generated by the faulty pair of thrusters in the three cases simulated above we can infer the following cause-effect relationships:

- In the case of a faulty pair of thrusters, one of the thrusters generates more pulses than the other and that difference is "considerable".
- If the faulty thruster is the one which generates more pulses, then we can infer that the fault produces a reduction in the amount of thrust generated by each pulse.

- If the faulty thruster is the one which generates fewer pulses, then we can infer that the fault produces an augmentation in the amount of thrust produced by each pulse.

5.5. Conclusions

A dynamic neural network-based fault detection and isolation scheme is developed to detect faults in the actuators of a follower spacecraft in a formation flying mission. The implemented attitude control subsystem uses a leader/follower architecture. Our proposed FDI scheme requires data from the attitude control subsystem of the follower. According to the simulation results, our proposed FDI scheme can detect the pair of thrusters which is faulty. Based on the number of pulses generated by the faulty pair, a second step analysis is performed. Using this analysis and depending on which thruster is faulty, one can identify if the fault produces an increase or a decrease in the amount of thrust produced.

The proposed scheme does not require exhaustive computational load. With only three dynamic neural networks one can monitor the health status of the complete set of actuators. It represents a promising detection capability, however as far as the isolation purposes are concerned, it does not work properly. Another characteristic of this approach is that the health monitoring analysis must be performed after the termination of the mission, implying that the fault detection cannot be performed in real-time.

Chapter 6

An Integrated Fault Detection and Isolation Scheme

Accurate coordination of the spacecraft in a formation flying mission is one of the most important requirements of the attitude control subsystem. Malfunctions in the spacecraft's components such as sensors and actuators may produce loss of coordination accuracy which may degenerate into fatal catastrophes. Detecting and isolating a faulty component allows the control subsystem to avoid the occurrence of failure by replacing the damaged component or make rearrangements (reconfiguration) in the control structure. Current literature presents a number of different FDI schemes for conventional single spacecraft. Despite the increased interest in the formation flying missions the lack of available FDI schemes is quite evident.

In Chapter 4 we have developed a "Low Level" or a "component level" FDI scheme based on dynamic neural networks for health monitoring PPT actuators of a spacecraft. The performance results obtained reveled that the use of a single fixed threshold to determine the health status of a thruster affects the precision of our FDI approach. In Chapter 5, dynamic neural networks are used again to develop an alternative "High Level" or "control level" FDI scheme for detecting behavioral deviations in the relative attitudes of the formation flying spacecraft. This second approach effectively can only detect faults and cannot determine which actuator is the faulty one and when the fault is injected. In this chapter, we take advantage of the strengths of the previous two FDI schemes and propose a new integrated FDI scheme. The complete structure of our proposed FDI scheme is presented and explained. In order to measure the capabilities of the proposed approach, experimental faulty scenarios are simulated and evaluated. Finally, some comments on our proposed FDI scheme are presented in the conclusion section.

6.1 Simulation Environment of the Integrated FDI

In Chapter 4, Section 4.1, we presented simulation environmental characteristics that are utilized to represent the electromechanical behavior of the pulsed-plasma thruster (PPT). The possible fault causes are also described and the data set needed by our "Low Level" FDI scheme was described. Chapter 5, Section 5.1, presented the simulated operational environment and spacecraft's characteristics that are valid for the simulated formation flying mission. We generated the data set that is needed by the "High Level" FDI scheme. All the above characteristics are also valid for the simulations that are performed in this chapter.

6.2 Integrated Neural Network FDI Scheme

The "Low Level" FDI scheme proposed in Chapter 4 is shown in Figure 6.1. This scheme is composed of three identical DNNs which analyze and determine the health status of the six PPT. The thrusters are grouped into pairs with a common capacitor implying that the pair of thrusters cannot be activated at the same time. Each DNN uses the capacitor voltage ($v_{x\text{-}axis}(k)$, $v_{y\text{-}axis}(k)$, $v_{z\text{-}axis}(k)$) to estimate its corresponding discharge current ($y_{x\text{-}axis,est}(k+1)$, $y_{y\text{-}axis,est}(k+1)$, $y_{z\text{-}axis,est}(k+1)$) produced during the activation of each thruster. The estimated discharge currents are compared with the actual discharge currents ($y_{x\text{-}axis}(k+1)$, $y_{y\text{-}axis}(k+1)$, $y_{z\text{-}axis}(k+1)$) and the residuals are generated (residuals are calculated using the mean absolute error *MAE*). If any residual is above or bellow a previously defined *Threshold* value (the three DNNs use the same fixed *Threshold*), the thruster under evaluation is considered as faulty or healthy, respectively.

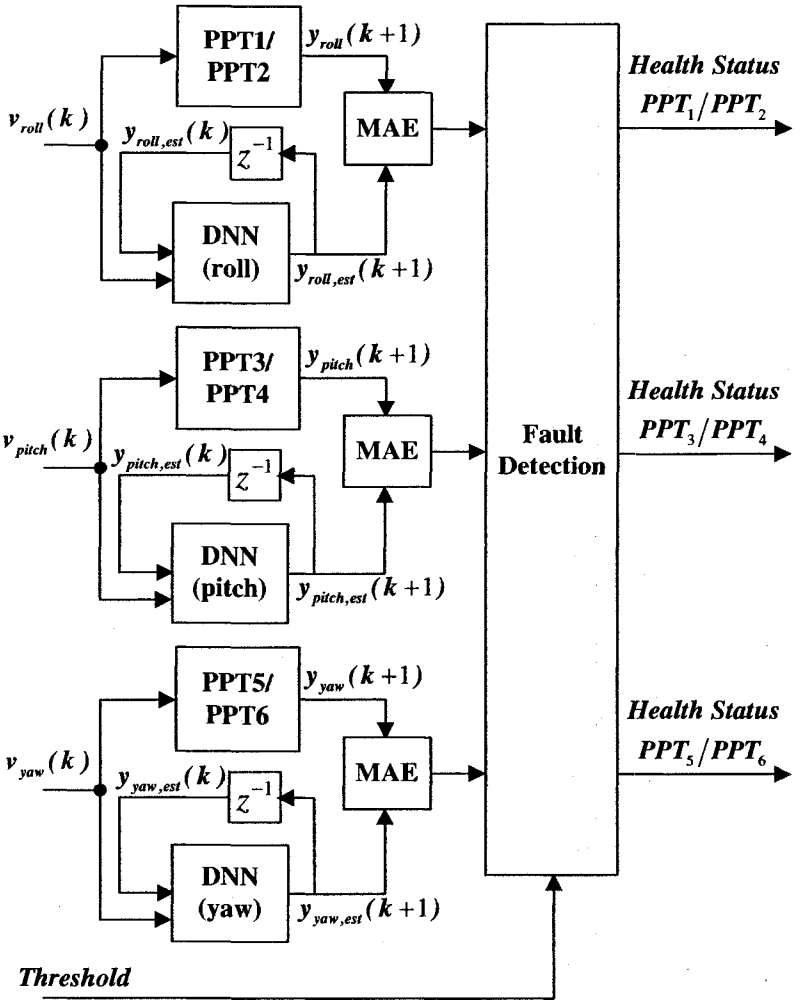

Figure 6.1. Proposed "Low Level" FDI Scheme.

Figure 6.2 shows the "High Level" FDI scheme that was proposed in Chapter 5 which is composed by three DNNs. As described in Chapter 5, Section 5.3, a set of three relative attitude variables and the sequence of pulses that are generated by the corresponding pair of thrusters ($\left[u_1^i\ u_2^i\ u_3^i\ u_4^i\right]^T$) are presented to each DNN (the three DNNs are not identical). The three components of the relative angular velocity are estimated ($y_{ROLL,est}(k+1)$, $y_{PITCH,est}(k+1)$, $y_{YAW,est}(k+1)$) and compared with the actual variables ($y_{ROLL,actual}(k+1)$, $y_{PITCH,actual}(k+1)$, $y_{YAW,actual}(k+1)$). Using equations (5.2) and (5.3) the three residual values are calculated ($E_{ROLL,abs}$, $E_{PITCH,abs}$, $E_{YAW,abs}$) and then compared with the corresponding $Threshold_i$ value (this approach uses different *Threshold* values for each DNN). If any residual exceeds its corresponding

threshold value, the pair of thrusters responsible for the rotational maneuvers around that axis is declared faulty.

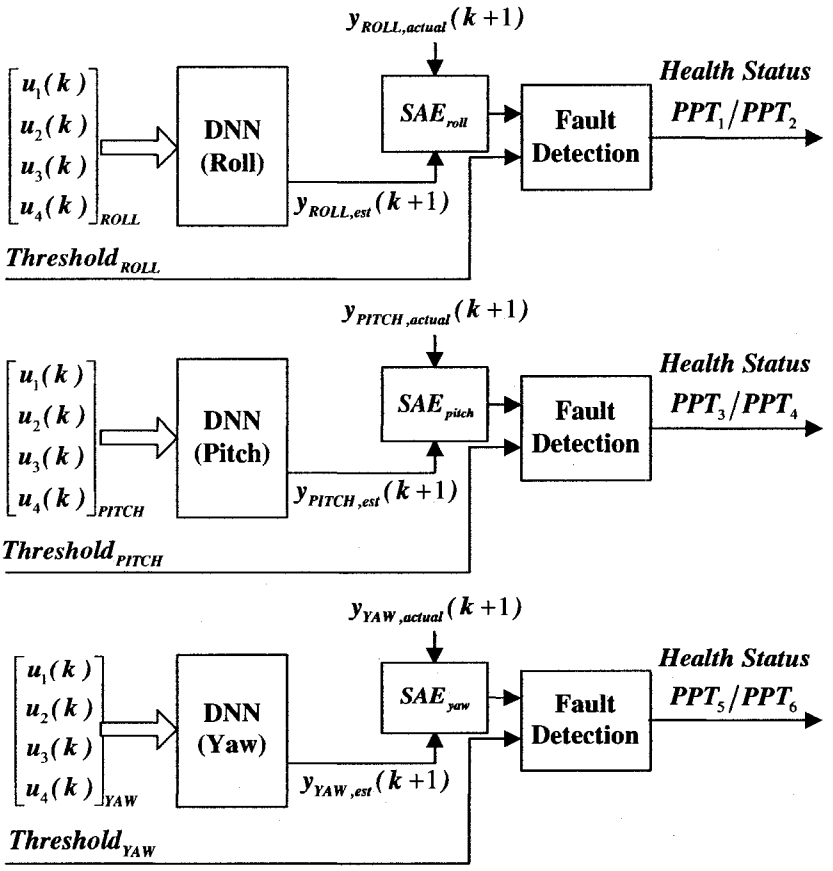

Figure 6.2. Proposed "High Level" FDI Scheme.

In the previous chapters we demonstrated that under the presence of a faulty actuator the "High Level" FDI scheme is an efficient fault detection tool. Using the relative attitude variables, we can detect abnormal spacecraft's behavior and can identify the pair of thrusters where the fault is located at. Furthermore, after the detection of the faulty pair and based on the number of pulses that are generated by the faulty pair, we can categorize the possible type of fault (e.g. an increase or a decrease in the amount of thrust) that is affecting each thruster. Unfortunately, the "High Level" FDI scheme cannot isolate the faulty actuator. On the other hand, the "Low Level" FDI scheme can analyze the health status of the six thrusters pulse by pulse. The difficulty is with the utilization of a single fixed *Threshold* value for determining the occurrence of a fault. Clearly, when the produced thrust is 15% less than the expected value (see Chapter 4, Sections 4.2.2 and

4.2.4), the required *Threshold* should be different from that when the produced thrust is 15% higher than the expected one (see Chapter 4, Sections 4.2.3).

By integrating the above FDI schemes one can take advantage of the strengths of each scheme and at same time reduce their individual weaknesses. The "Integrated" FDI scheme uses the "High Level" approach for detecting which pair of thrusters is healthy and which one is faulty. Once the faulty thruster pair is identified, the "Integrated" FDI scheme uses the "Low Level" approach to investigate which thruster is faulty one and, more specifically, which one of the generated pulses is faulty. For the sake of brevity, the variables that are defined in Tables 6.I-6.III are used to represent the faulty pair of thrusters that is detected by the "High Level" FDI scheme.

PPT_1/PPT_2 is detected as the faulty pair of thrusters		
$PPT(+)$	:	thruster PPT_1
$PPT(-)$	:	thruster PPT_2
${}^{follower,j}_{leader}T_{PPT(+)/PPT(-)}$	:	sequence of pulses about the x-axis ($s/c_{f,j}$ w.r.t. s/c_l)
$\#PPT(+)$	:	pulses that are generated by the thruster PPT_1
$\#PPT(-)$	:	pulses that are generated by the thruster PPT_2
v_i	:	capacitor voltage $v_{x\text{-}axis}$
$y_{i,est}$	:	estimated discharge current $y_{x\text{-}axis}$
$y_{i,(+)}$	:	discharge current of thruster PPT_1
$y_{i,(-)}$	:	discharge current of thruster PPT_2

Table 6.I. Definition of Variables used by the "Integrated" FDI Scheme when PPT_1/PPT_2 is the Faulty Pair of Thrusters.

PPT_3/PPT_4 is detected as the faulty pair of thrusters		
$PPT(+)$	:	thruster PPT_3
$PPT(-)$	:	thruster PPT_4
${}^{follower,j}_{leader}T_{PPT(+)/PPT(-)}$	:	sequence of pulses about the y-axis ($s/c_{f,j}$ w.r.t. s/c_l)
$\#PPT(+)$	:	pulses that are generated by the thruster PPT_3
$\#PPT(-)$	:	pulses that are generated by the thruster PPT_4
v_i	:	capacitor voltage $v_{y\text{-}axis}$
$y_{i,est}$	:	estimated discharge current $y_{y\text{-}axis}$
$y_{i,(+)}$	:	discharge current of thruster PPT_3
$y_{i,(-)}$	:	discharge current of thruster PPT_4

Table 6.II. Definition of Variables used by the "Integrated" FDI Scheme when PPT_3/PPT_4 is the Faulty Pair of Thrusters.

PPT_5/PPT_6 is detected as the faulty pair of thrusters		
$PPT(+)$	:	thruster PPT_5
$PPT(-)$	:	thruster PPT_6
${}^{follower,j}_{leader}T_{PPT(+)/PPT(-)}$	:	sequence of pulses about the z-axis (s/c_{fj} w.r.t. s/c_l)
$\#PPT(+)$	:	pulses that are generated by the thruster PPT_5
$\#PPT(-)$	:	pulses that are generated by the thruster PPT_6
v_i	:	capacitor voltage $v_{z\text{-}axis}$
$y_{i,est}$	:	estimated discharge current $y_{z\text{-}axis}$
$y_{i,(+)}$	:	discharge current of thruster PPT_5
$y_{i,(-)}$	:	discharge current of thruster PPT_6

Table 6.III. Definition of Variables used by the "Integrated" FDI Scheme when PPT_5/PPT_6 is the Faulty Pair of Thrusters.

From the results presented in Chapter 4, Section 4.5, it is evident that the precision of the scheme can be improved by utilization of two fixed *Threshold* values, a lower *Threshold* value for faulty scenarios where the actual amount of thrust is higher than expected value and a higher *Threshold* value for faulty scenarios where the actual amount of thrust is smaller than the expected value. Based on the number of pulses generated by the pair of thrusters that is declared as a faulty pair, in Chapter 5, Section 5.4, an important cause-effect relationship was established. This relationship allows the construction of a Logic Threshold Selection Block which is represented by the diagram that is shown in Figure 6.3 and is described below:

- After the detection of the faulty pair of thruster, the sequence of pulses ${}^{follower,j}_{leader}T_{PPT(+)/PPT(-)}$ is presented to the Logic Threshold Selection Block.
- The Logic Threshold Selection Block determines the number of pulses that were generated by each thruster (e.g. $\#PPT(+)$ and $\#PPT(-)$) and then determines which one of the thruster generated the biggest number of pulses.
- If the number of pulses generated by the thruster $PPT(+)$ (e.g. $\#PPT(+)$) is bigger than the number of pulses generated by the thruster $PPT(-)$ (e.g. $\#PPT(-)$) The "Low Level" FDI scheme must employ the *Upper Threshold* and the *Lower Threshold* for the health analysis of $PPT(+)$ and $PPT(-)$, respectively. The "Low Level" FDI scheme must employ the *Upper Threshold* and the *Lower Threshold* for the health analysis of $PPT(-)$ and $PPT(+)$,

respectively.

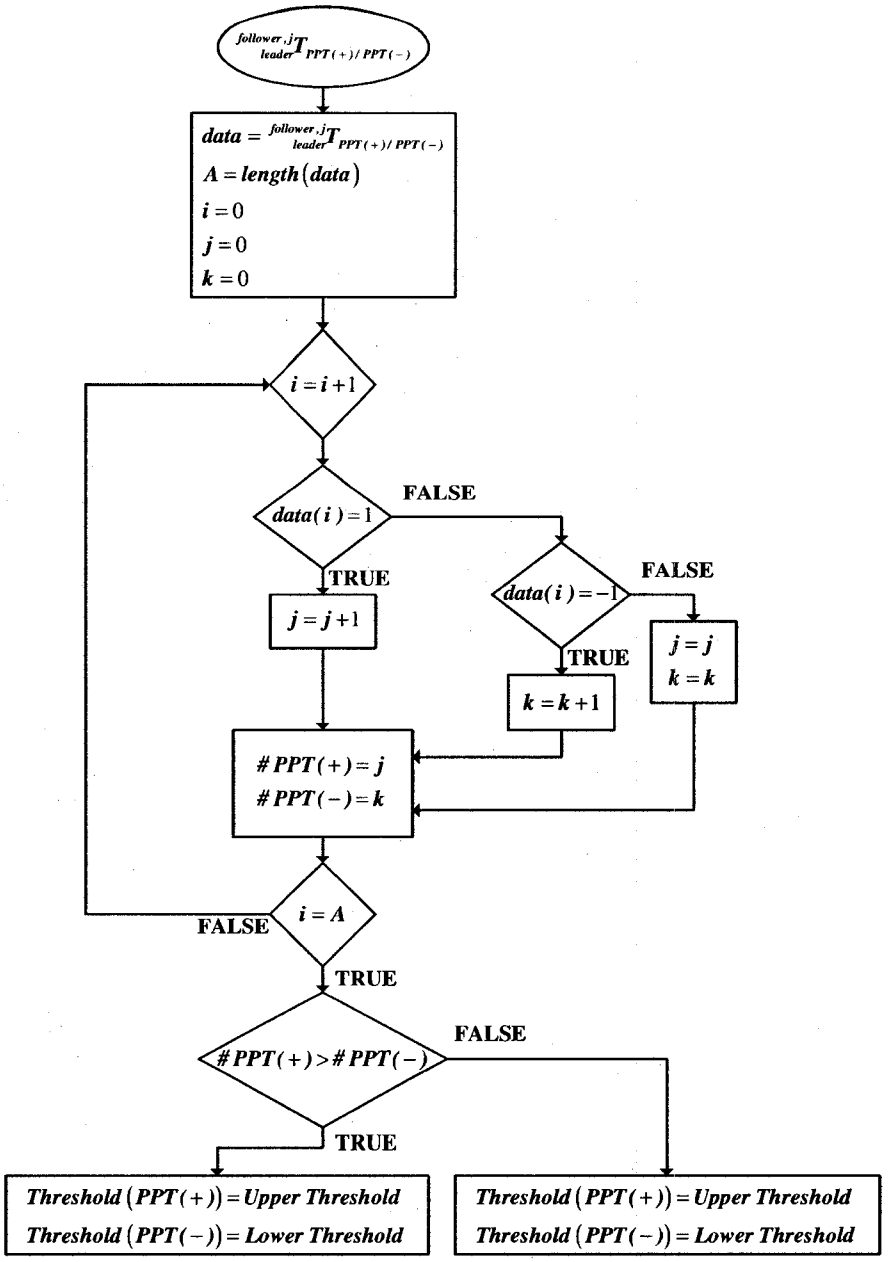

Figure 6.3. Representative Diagram of the Logic Threshold Selection.

Now, with the Logic Threshold Selection Block specified, the integrated FDI scheme is complete. Figure 6.4 shows our proposed FDI scheme. Using the three DNNs of the "High Level" FDI scheme, we detect if an abnormality occurs in the *roll*, *pitch* or *yaw* angles, and then identify the pair of thrusters that is responsible for the abnormality. Based on the number of pulses generated by the pair of thrusters identified in the "High Level" FDI scheme, the Logic Threshold

Selection Block selects a proper *Threshold* value for each thruster. A single DNN extracted from the "Low Level" FDI scheme is required. Using this DNN to model the pair of thrusters, the residuals (*MAE*) are generated and then using the corresponding *Threshold* values the health status of each pulse is determined.

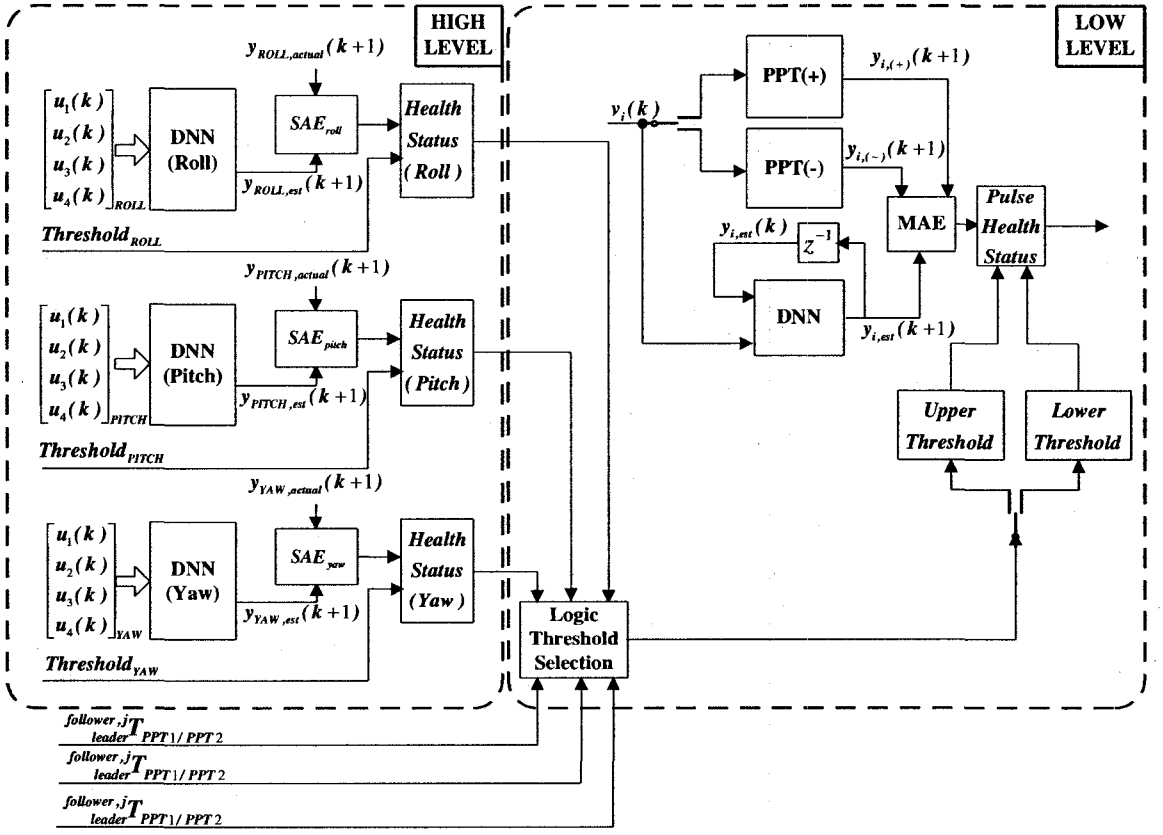

Figure 6.4. Proposed "Integrated" FDI Scheme.

Based on the results obtained in Chapter 4, Section 4.4, we fixed the *Lower* and the *Upper Thresholds* at 0.030 and 0.037, respectively.

6.3. Simulations Results for the Integrated FDI

To investigate the performance of our proposed "Integrated" FDI scheme we consider the following 3 faulty cases:

- **Fault Case 1:** Mass fault reduction is a type of fault that affects the production of thrust. With less amount of propellant mass available, the amount of particles ablated and ionized also decreases generating a reduction in the amount of thrust generated by the actuator.
- **Fault Case 2:** The ablation process transforms the solid propellant into the exhaust plasma, but small portions of the propellant may not be transformed, resulting in particles which are added to the inner face of the electrodes. After several pulses, this situation may lead to degradations of the PPT performance.
- **Fault Case 3:** Due to wear and tear, conductivity of the wires, capacitor and electrodes may decrease. As a consequence of this, the amount of thrust produced may be changed in an unpredictable manner.

To test our proposed "Integrated" FDI scheme, eight faulty scenarios are simulated and the details are shown in Table 6.IV. The injected faults are simulated by modifying the corresponding parameters of the faulty PPT as shown equations (6.1) – (6.4), namely

Faulty Scenario	Rotational Maneuver	Faulty Actuator	Type of Fault	Occurrence Time
1	[20°, 30°, 40°]	PPT_1	Faulty Case 1 (15 %)	t = 0 sec
2	[25°, 30°, 40°]	PPT_4	Faulty Case 1 (15 %)	t = 0 sec
3	[20°, 35°, 45°]	PPT_5	Faulty Case 2 (15 %)	t = 0 sec
4	[25°, 35°, 45°]	PPT_2	Faulty Case 2 (15 %)	t = 0 sec
5	[25°, 40°, 55°]	PPT_3	Faulty Case 3 (incremental)	t = 400 sec
6	[30°, 40°, 50°]	PPT_6	Faulty Case 3 (incremental)	t = 400 sec
7	[20°, 45°, 60°]	PPT_3	Faulty Case 2 (incremental)	t = 300 sec
8	[30°, 45°, 55°]	PPT_4	Faulty Case 2 (incremental)	t = 300 sec

Table 6.IV. Health Analysis Conditions Considered by Our Proposed "Integrated" FDI Approach.

Fault Scenario 1:

$$m_{0,PPT_1} = \begin{cases} 2.58\times10^{-8} kg; & t \le 0 \\ 3.00\times10^{-9} kg; & t > 0 \end{cases} \tag{6.1}$$

Fault Scenario 2:

$$m_{0,PPT_4} = \begin{cases} 2.58\times10^{-8} kg; & t \le 0 \\ 3.00\times10^{-9} kg; & t > 0 \end{cases}$$

Fault Scenario 3:

$$w_{PPT_5} = \begin{cases} 0.0254 m; & t \le 0 \\ 0.02195 m; & t > 0 \end{cases} \tag{6.2}$$

Fault Scenario 4:

$$w_{PPT_2} = \begin{cases} 0.0254 m; & t \le 0 \\ 0.02195 m; & t > 0 \end{cases}$$

Fault Scenario 5:

$$R_{pe,PPT_3} = \begin{cases} 0.0001\Omega; & t \le 400 \\ 1 - \left[\dfrac{\left(\dfrac{100}{1+0.009\times l} \right) - 85}{1750} + 0.9919 \right] \Omega; & t > 400, l = 1,2,3,.....,\infty \end{cases} \tag{6.3}$$

Fault Scenario 6:

$$R_{pe,PPT_6} = \begin{cases} 0.0001\Omega; & t \le 400 \\ 1 - \left[\dfrac{\left(\dfrac{100}{1+0.009\times l} \right) - 85}{1750} + 0.9919 \right] \Omega; & t > 400, l = 1,2,3,.....,\infty \end{cases}$$

Fault Scenario 7:

$$w_{PPT_3} = \begin{cases} 0.0254m; & t \le 300 \\ 1 - \left[\dfrac{\left(\dfrac{100}{1+0.0001 \times l} \right) - 115}{6400} + 0.9780 \right] m; & t > 300, l = 1,2,3,.....,\infty \end{cases} \tag{6.4}$$

Fault Scenario 8:

$$w_{PPT_4} = \begin{cases} 0.0254m; & t \le 300 \\ 1 - \left[\dfrac{\left(\dfrac{100}{1+0.0001 \times l} \right) - 115}{6400} + 0.9780 \right] m; & t > 300, l = 1,2,3,.....,\infty \end{cases}$$

Fault Scenario 1 Results: Figures 6.5 shows the actual reduction in the amount of torque that is generated by the thruster PPT_1 due to the injected fault. All the pulses generated by PPT_1 are outside the healthy zone. On the other hand, PPT_2 did not generate pulses during the entire rotational maneuver.

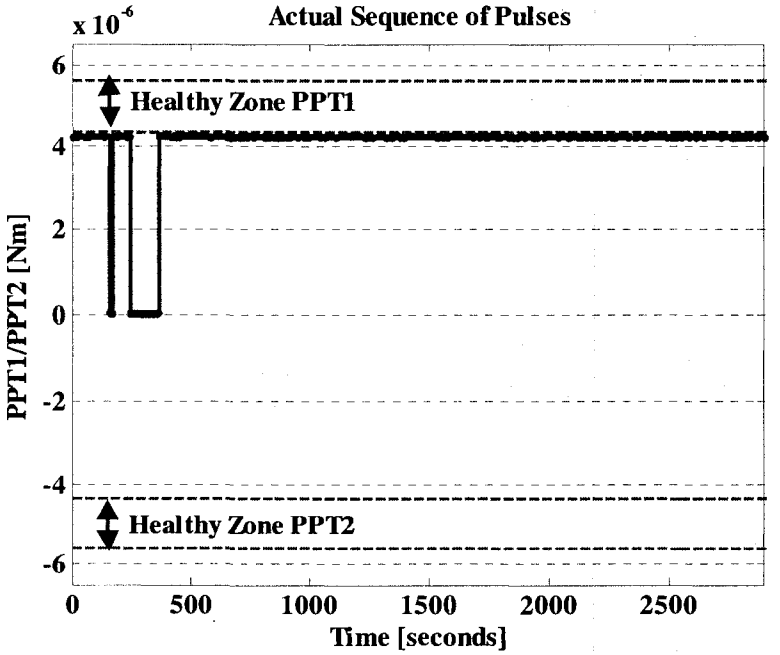

Figure 6.5. Actual Sequence of Pulses Generated by PPT_1/ PPT_2 for Fault Scenario 1.

As shown in Figure 6.6, the first stage of our proposed "Integrated" FDI scheme estimates

the three components of the angular velocity and then compares the estimates with the actual variables to generate the corresponding residuals (SAE_i). The results are shown in Table 6.V.

	SAE_i	$Threshold_i$	$Health\ Status_i$
DNN_{Roll}	**356.87**	135.00	Faulty
DNN_{Pitch}	36.77	50.00	Healthy
DNN_{Yaw}	59.54	76.00	Healthy

Table 6.V. Health Analysis Results Obtained by Our Proposed FDI Approach under Fault Scenario 1.

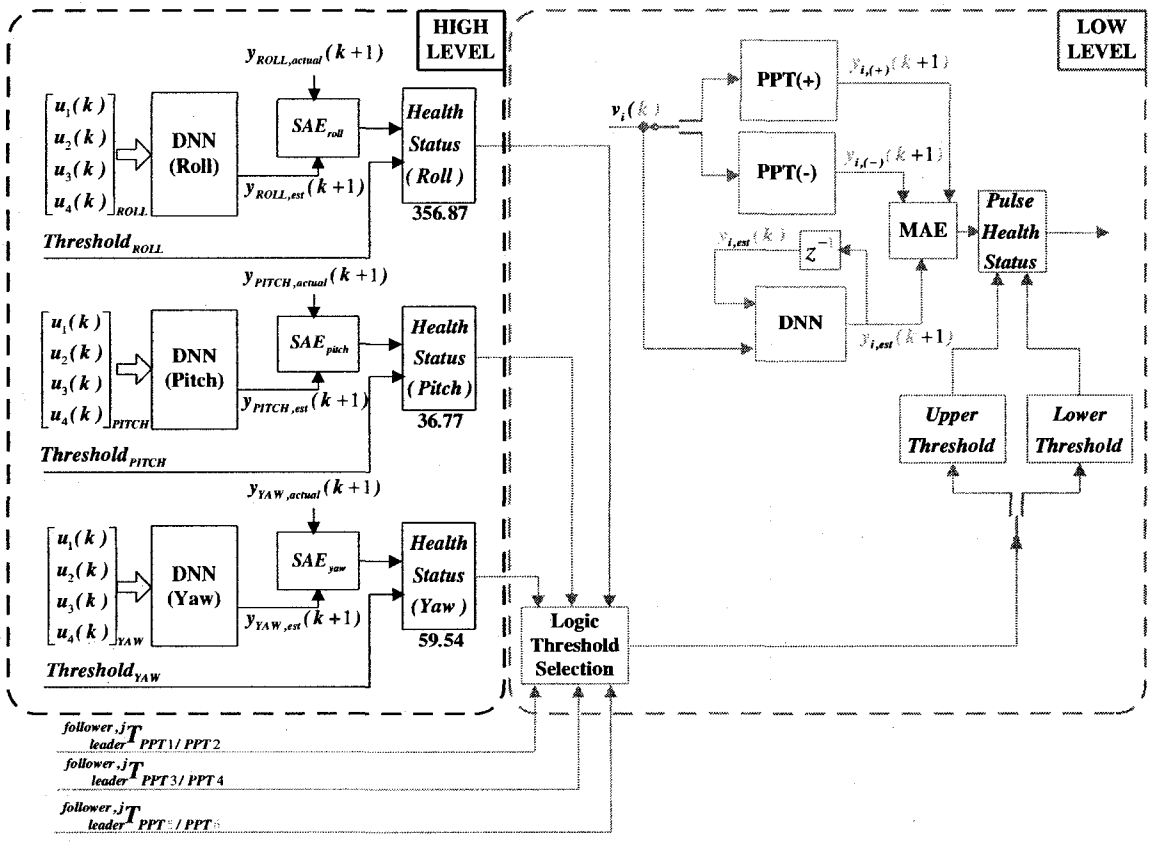

Figure 6.6. First Stage Analysis of the "Integrated" FDI Scheme for Fault Scenario 1.

The fault is declared in the pair of thrusters PPT_1/ PPT_2. Based on the number of pulses that are generated by the pair, the Logic Threshold Selection Block defines the *Threshold* value for both thrusters (Figure 6.7). Table 6.VI shows the resulting Thresholds. In this case, since the thruster PPT_2 does not produce any pulse it is evident that the faulty thruster must be PPT_1.

	Number of Pulses	*Threshold Value*
PPT_1	2770	0.0370 (Upper)
PPT_2	0	0.0300 (Lower)

Table 6.VI. Logic Threshold Selection under Fault Scenario 1.

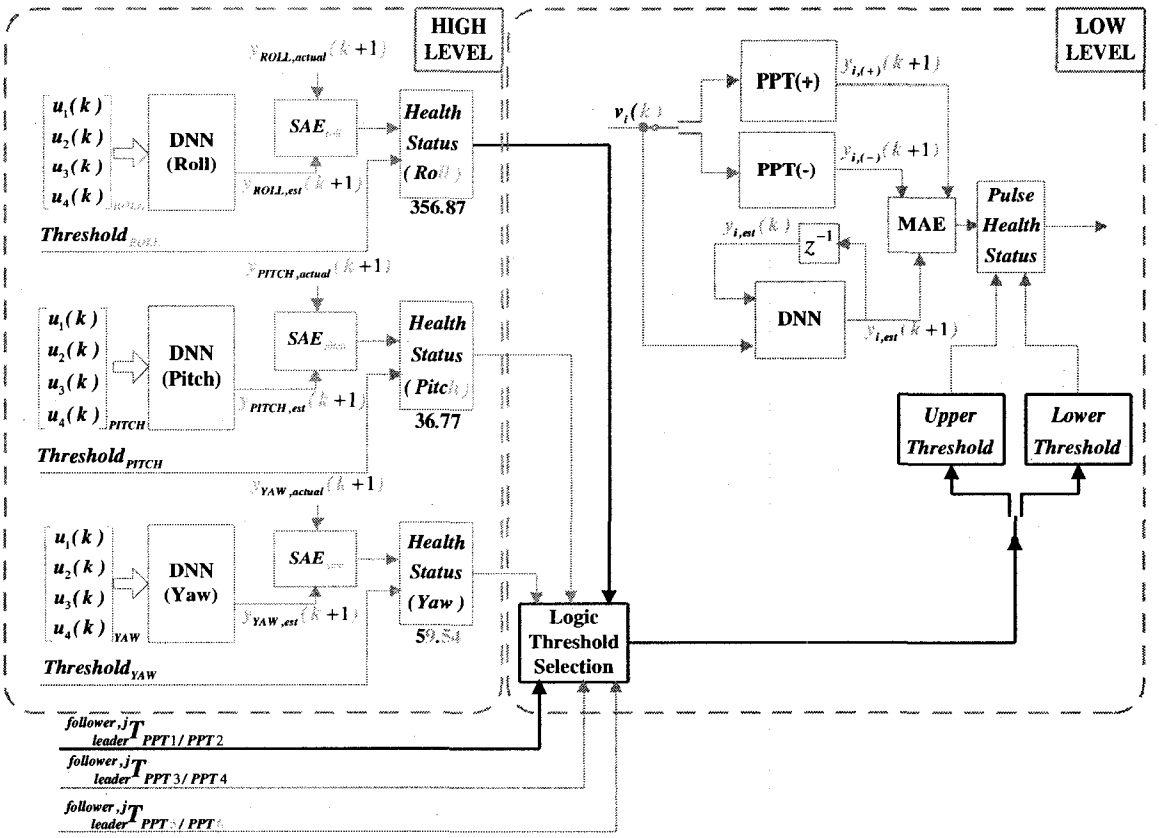

Figure 6.7. Logic Threshold Selection of the "Integrated" FDI Scheme for Fault Scenario 1.

Once the *Thresholds* are assigned, the proposed "Integrated" FDI scheme activates the second stage of the detection and isolation (Figure 6.8). Figure 6.9 shows the health status signal for PPT_1 and PPT_2 for all the simulated period. According to these status signals the entire set of pulses are generated by PPT_1. Since PPT_2 did not generate any pulse, no health status signal is produced. As shown in Figure 6.10, the first faulty pulse that is generated by PPT_1 is the pulse number 1. Table 6.VII shows the final health monitoring results that are obtained by using our proposed "Integrated" FDI scheme.

	Actual Healthy Pulses	Actual Faulty Pulses	Detected Healthy Pulses	Detected Faulty Pulses	Additional Information
PPT_1	0	2770	0	2770	Faulty Case 1 or 3
PPT_2	0	0	0	0	No fault detected

Table 6.VII. "Integrated" FDI Scheme Results for s/c_{f1} under Fault Scenario 1.

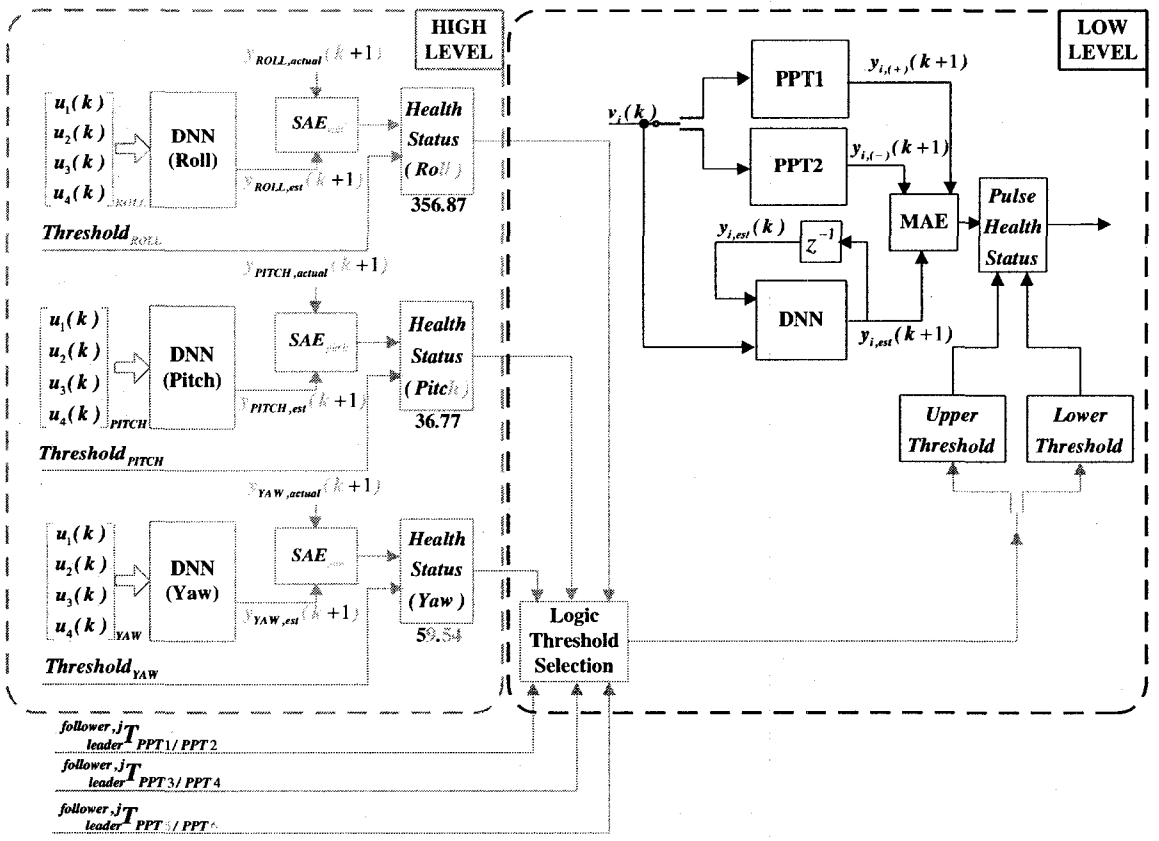

Figure 6.8. Second Stage Analysis of the "Integrated" FDI Scheme for Fault Scenario 1.

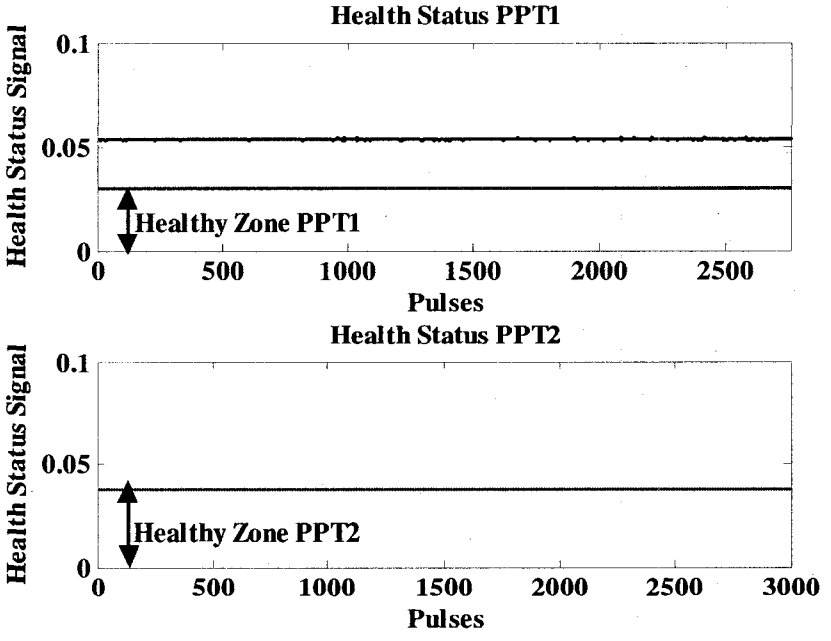

Figure 6.9. Health Status Signals for PPT_1/ PPT_2 for the Fault Scenario 1.

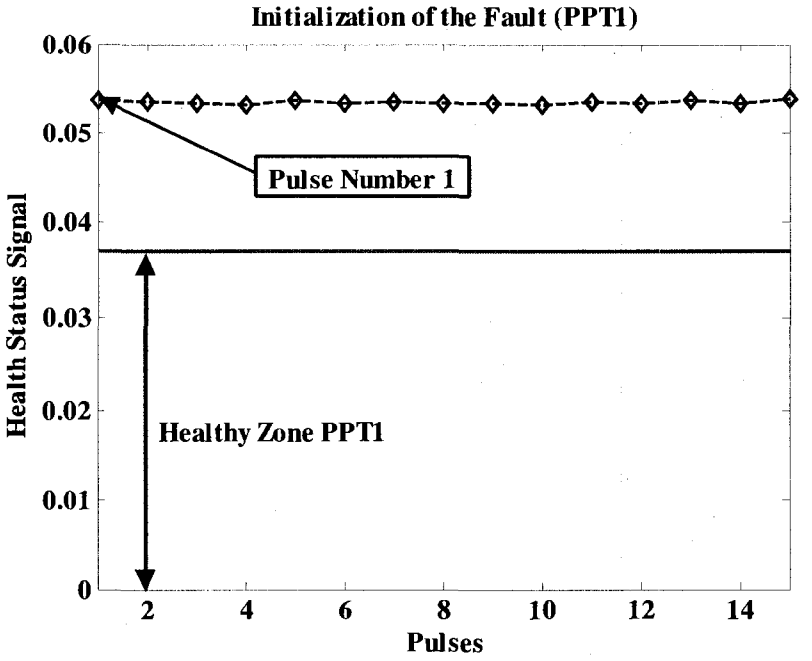

Figure 6.10. Initialization of the Fault which Affects PPT_1 for the Fault Scenario 1.

For the sake of brevity, figures such as Figures 6.6 to 6.8 are not shown for the following simulated seven faulty scenarios.

Fault Scenario 2 Results: Figure 6.11 shows the actual reduction in the amount of torque that is generated by the thruster PPT_4 due to the injected fault. All the pulses that are generated by PPT_4 are outside the healthy zone. On the other hand, PPT_3 generates only healthy pulses. The first stage of our proposed "Integrated" FDI scheme estimates the three components of the angular velocity and then compares the estimates with the actual variables to generate the corresponding residuals (SAE_i). The results are shown in Table 6.VIII.

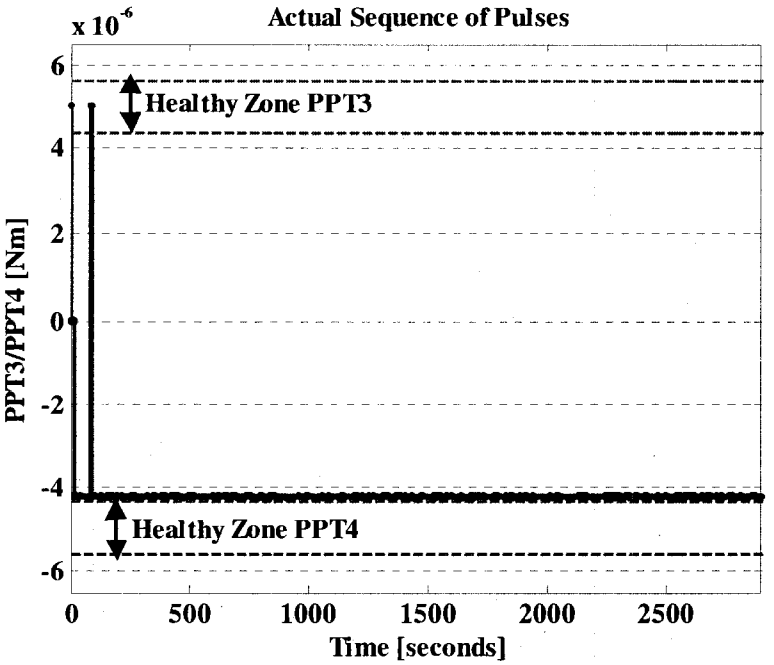

Figure 6.11. Actual Sequence of Pulses Generated by PPT_3/ PPT_4 for the Fault Scenario 2.

	SAE_i	$Threshold_i$	$Health\ Status_i$
DNN_{Roll}	133.14	135.00	Healthy
DNN_{Pitch}	**108.06**	50.00	Faulty
DNN_{Yaw}	64.52	76.00	Healthy

Table 6.VIII. Health Analysis Results Obtained by Our Proposed FDI Approach under Fault Scenario 2.

The fault is declared in the pair of thrusters PPT_3/ PPT_4. Based on the number of pulses generated by the pair, the Logic Threshold Selection Block especifies the *Threshold* values for both thrusters. Table 6.IX shows the resulting Thresholds.

	Number of Pulses	*Threshold Value*
PPT_3	5	0.0300 (Lower)
PPT_4	2883	0.0370 (Upper)

Table 6.IX. Logic Threshold Selection under Fault Scenario 2.

Once the *Thresholds* are assigned, the proposed "Integrated" FDI scheme activates the second stage of the detection and isolation. Figure 6.12 shows the health status signal for PPT_3 and PPT_4 for all the simulated period. According to these health status signals, the entire set of pulses generated by PPT_4 is faulty and the 5 pulses generated by PPT_3 are healthy. As shown in Figure 6.13, the first faulty pulse generated by PPT_4 is the pulse number 1. Table 6.X shows the final health monitoring results that are obtained by using our proposed "Integrated" FDI scheme.

	Actual Healthy Pulses	Actual Faulty Pulses	Detected Healthy Pulses	Detected Faulty Pulses	Additional Information
PPT_3	5	0	5	0	No fault detected
PPT_4	0	2883	0	2883	Faulty Case 1 or 3

Table 6.X. "Integrated" FDI Scheme Results for s/c_{f1} under Fault Scenario 2.

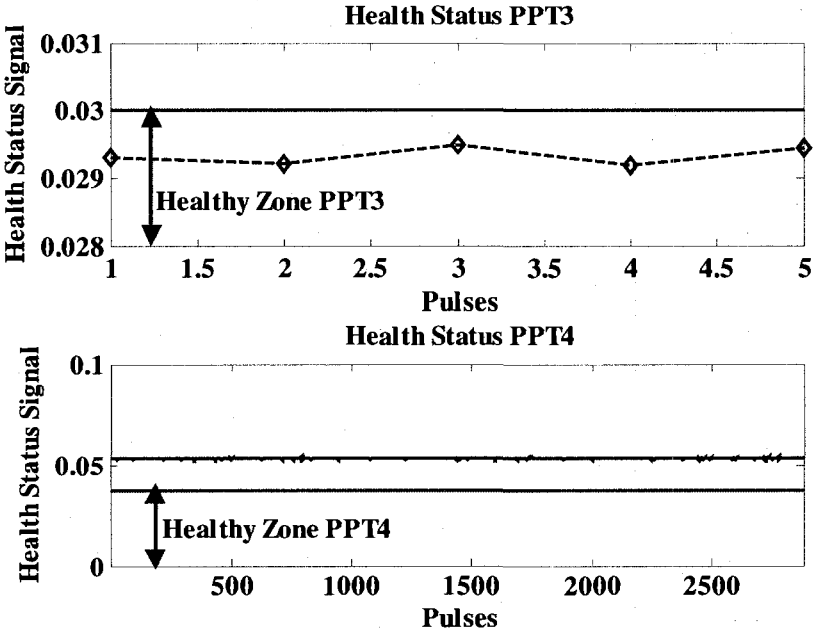

Figure 6.12. Health Status Signals for PPT_3/ PPT_4 (Fault Scenario 2).

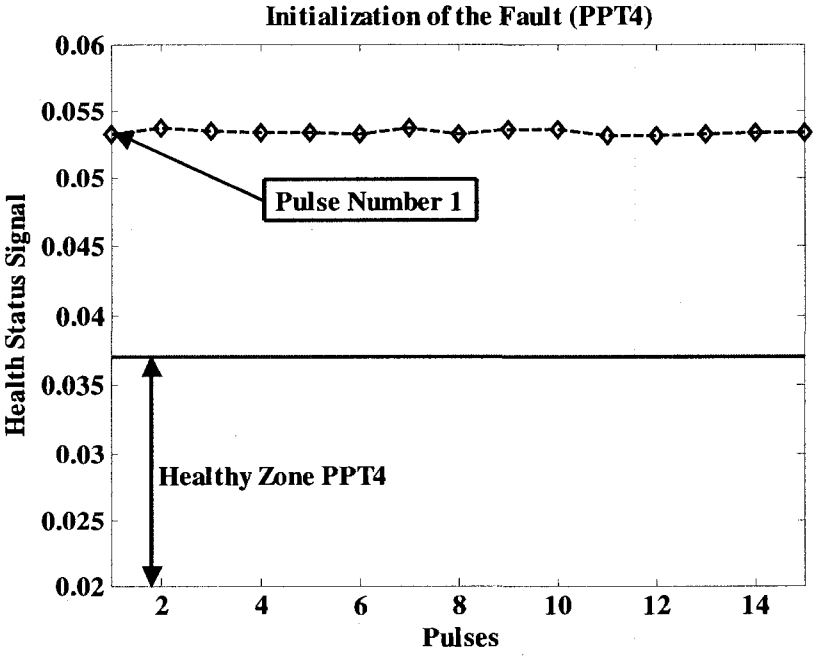

Figure 6.13. Initialization of the Fault which Affects PPT_4 (Fault Scenario 2).

Fault Scenario 3 Results: Figures 6.14 shows the actual augmentation in the amount of the torque that is generated by the thruster PPT_5 due to the injected fault. All the pulses generated by PPT_5 are outside the healthy zone. On the other hand, PPT_6 generates only healthy pulses. The first stage of our proposed "Integrated" FDI scheme estimates the three components of the angular velocity and then compares the estimates with the actual variables to generate the corresponding residuals (SAE_i). The results are shown in Table 6.XI.

	SAE_i	$Threshold_i$	$Health\ Status_i$
DNN_{Roll}	92.65	135.00	Healthy
DNN_{Pitch}	40.97	50.00	Healthy
DNN_{Yaw}	**100.91**	76.00	Faulty

Table 6.XI. Health Analysis Results Obtained by our Proposed FDI Approach for the Fault Scenario 3.

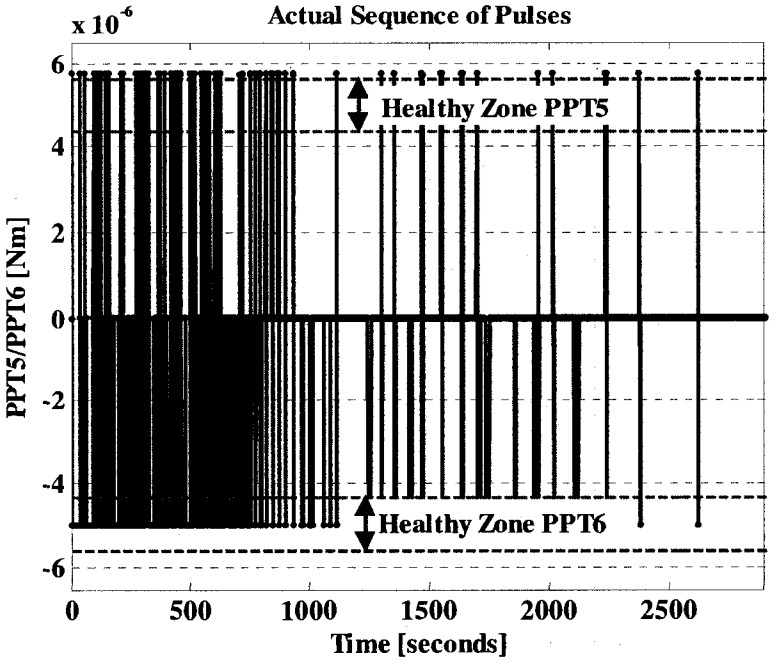

Figure 6.14. Actual Sequence of Pulses Generated by PPT_5/ PPT_6 for the Fault Scenario 3.

The fault is declared in the pair of thrusters PPT_5/ PPT_6. Based on the number of pulses generated by the pair, the Logic Threshold Selection Block especifies the *Threshold* values for both thrusters. Table 6.XII shows the resulting Thresholds.

	Number of Pulses	*Threshold Value*
PPT_5	115	0.0300 (Lower)
PPT_6	541	0.0370 (Upper)

Table 6.XII. Logic Threshold Selection under the Fault Scenario 3.

Once the *Thresholds* are assigned, the proposed "Integrated" FDI scheme activates the second stage of the detection and isolation. Figure 6.15 shows the health status signals for PPT_5 and PPT_6 during the simulated period. According to the health status signals, the entire set of pulses generated by PPT_5 is faulty meanwhile the pulses generated by PPT_6 are healthy. As shown in Figure 6.16, there are seven pulses that are generated by PPT_5 that were declared as healthy but actually, they were faulty (FALSE NEGATIVE). Table 6.XIII shows the final health monitoring results that are obtained by using our proposed "Integrated" FDI scheme.

	Actual Healthy Pulses	**Actual Faulty Pulses**	**Detected Healthy Pulses**	**Detected Faulty Pulses**	**Additional Information**
PPT_5	0	115	7	108	Faulty Case 2
PPT_6	541	0	541	0	No fault detected

Table 6.XIII. 'Combined' FDI Scheme Results for s/c_{f1} under Faulty Scenario 3 Conditions.

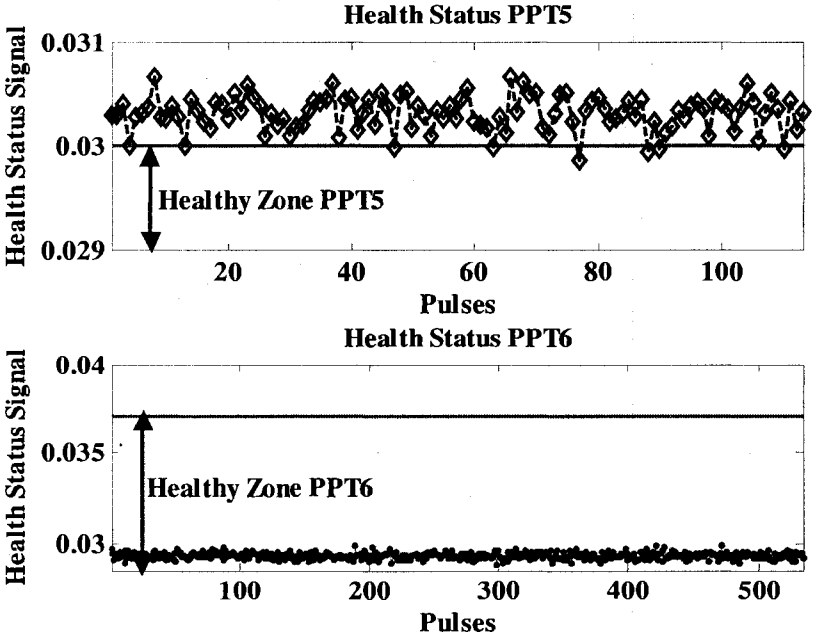

Figure 6.15. Health Status Signal for PPT_5/ PPT_6 (Fault Scenario 3).

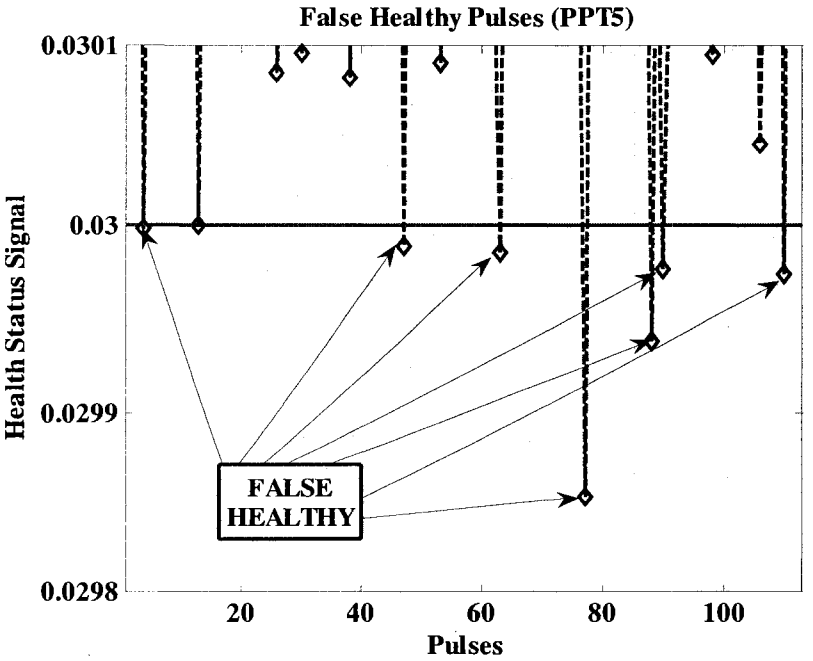

Figure 6.16. Misclassification of Pulses Generated by PPT_5 (Fault Scenario 3).

Fault Scenario 4 Results: Figures 6.17 shows the actual augmentation in the amount of the torque generated by the thruster PPT_2 due to the injected fault. All the pulses that are generated by PPT_2 are outside the healthy zone. On the other hand, PPT_1 generates only healthy pulses. The first stage of our proposed "Integrated" FDI scheme estimates the three components of the angular velocity and then compares the estimates with the actual variables to generate the corresponding residuals (SAE_i). The results are shown in Table 6.XIV.

	SAE_i	$Threshold_i$	$Health\ Status_i$
DNN_{Roll}	**152.35**	135.00	Faulty
DNN_{Pitch}	29.62	50.00	Healthy
DNN_{Yaw}	51.67	76.00	Healthy

Table 6.XIV. Health Analysis Results Obtained by our Proposed FDI approach for the Fault Scenario 4.

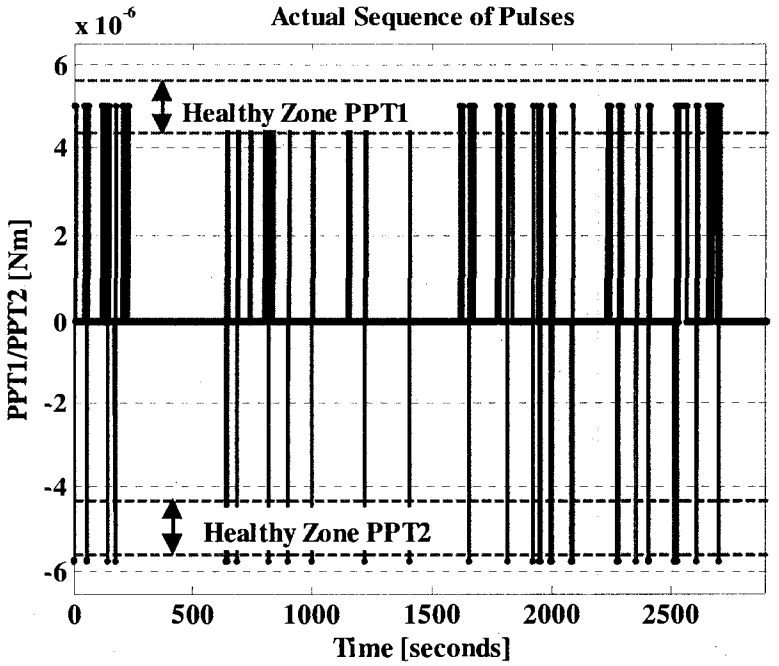

Figure 6.17. Actual Sequence of Pulses Generated by PPT_1/ PPT_2 for the Fault Scenario 4.

The fault is declared in the pair of thrusters PPT_1/ PPT_2. Based on the number of pulses that are generated by the pair, the Logic Threshold Selection Block defines the *Threshold* values for both thrusters. Table 6.XV shows the resulting Thresholds.

	Number of Pulses	*Threshold Value*
PPT_1	338	0.0370 (Upper)
PPT_2	44	0.0300 (Lower)

Table 6.XV. Logic Threshold Selection for the Fault Scenario 4.

Once the *Thresholds* are assigned, the proposed "Integrated" FDI scheme activates the second stage of the detection and isolation. Figure 6.18 shows the health status signal for PPT_1 and PPT_2 during the simulated period. According to the health status signals, the entire set of pulses generated by PPT_2 is faulty meanwhile the pulses generated by PPT_1 are healthy. Table 6.XVI shows the final health monitoring results that are obtained by using our proposed "Integrated" FDI scheme.

	Actual Healthy Pulses	Actual Faulty Pulses	Detected Healthy Pulses	Detected Faulty Pulses	Additional Information
PPT_1	338	0	338	0	No fault detected
PPT_2	0	44	0	44	Faulty Case 2

Table 6.XVI. "Integrated" FDI Scheme Results for s/c_{f1} for the Fault Scenario 4.

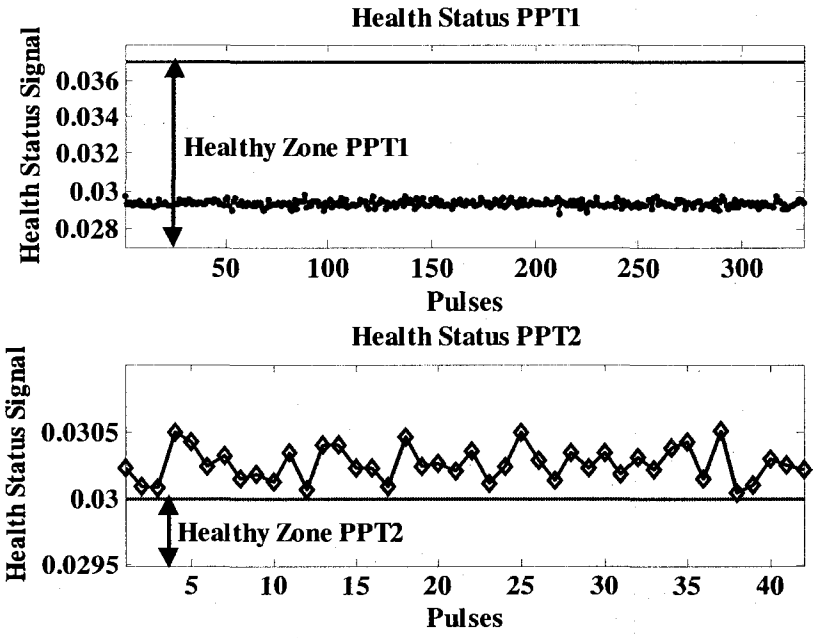

Figure 6.18. Health Status Signal for PPT_1/ PPT_2 (Fault Scenario 4).

Fault Scenario 5 Results: Figures 6.19 shows the actual reduction in the amount of the torque generated by the thruster PPT_3 due to the fault injected after t = 400 sec. Meanwhile, some of the pulses that are generated by PPT_3 are outside the healthy zone, and the pulses that are generated by PPT_4 are healthy. The first stage of our proposed "Integrated" FDI scheme estimates the three components of the angular velocity and then compares the estimates with the actual variables to generate the corresponding residuals (SAE_i). The results are shown in Table 6.XVII.

	SAE_i	$Threshold_i$	$Health\ Status_i$
DNN_{Roll}	85.05	135.00	Healthy
DNN_{Pitch}	**93.05**	50.00	Faulty
DNN_{Yaw}	47.89	76.00	Healthy

Table 6.XVII. Health Analysis Results Obtained by our Proposed FDI Approach for the Fault Scenario 5.

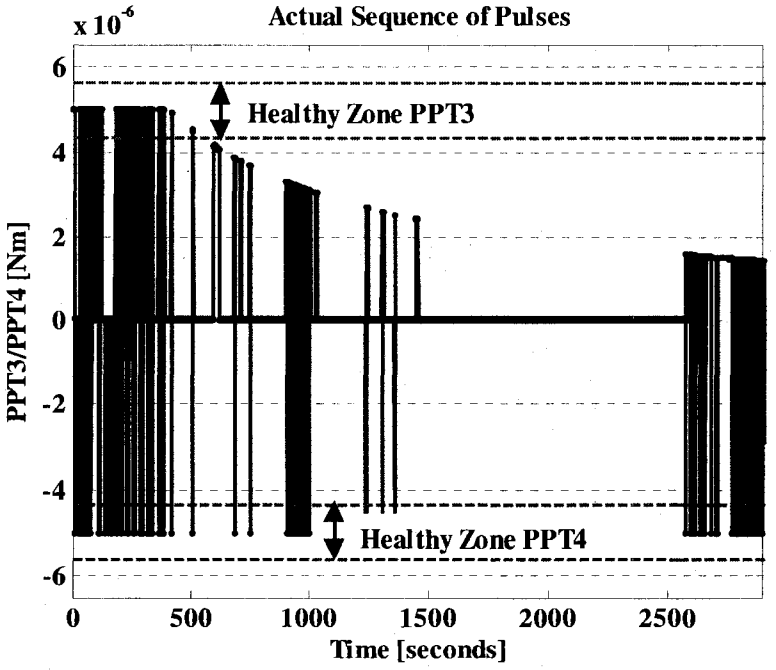

Figure 6.19. Actual Sequence of Pulses Generated by PPT_1/ PPT_2 for the Fault Scenario 5.

The fault is declared in the pair of thrusters *PPT_3/ PPT_4*. Based on the number of pulses that are generated by the pair, the Logic Threshold Selection Block defines the *Threshold* values for both thrusters. Table 6.XVIII shows the resulting Thresholds.

	Number of Pulses	*Threshold Value*
PPT_3	545	0.0370 (Upper)
PPT_4	153	0.0300 (Lower)

Table 6.XVIII. Logic Threshold Selection for the Fault Scenario 5.

Once the *Thresholds* are assigned, the proposed "Integrated" FDI scheme activates the second stage of the detection and isolation. Figure 6.20 shows the health status signal for *PPT_3* and *PPT_4* during the simulated period. According to the health status signals, the faulty pulses that are generated by *PPT_3* start with the pulse number 107, meanwhile all the pulses that are generated by *PPT_4* are healthy. Figure 6.21 shows the progressive increase of the fault severity in *PPT_3*. Table 6.XIX shows the final health monitoring results that are obtained by using our proposed "Integrated" FDI scheme.

	Actual Healthy Pulses	Actual Faulty Pulses	Detected Healthy Pulses	Detected Faulty Pulses	Additional Information
PPT_3	112	433	106	439	No fault detected
PPT_4	153	0	153	0	Faulty Case 1 or 3

Table 6.XIX. "Integrated" FDI Scheme Results for s/c_{f1} for the Fault Scenario 5.

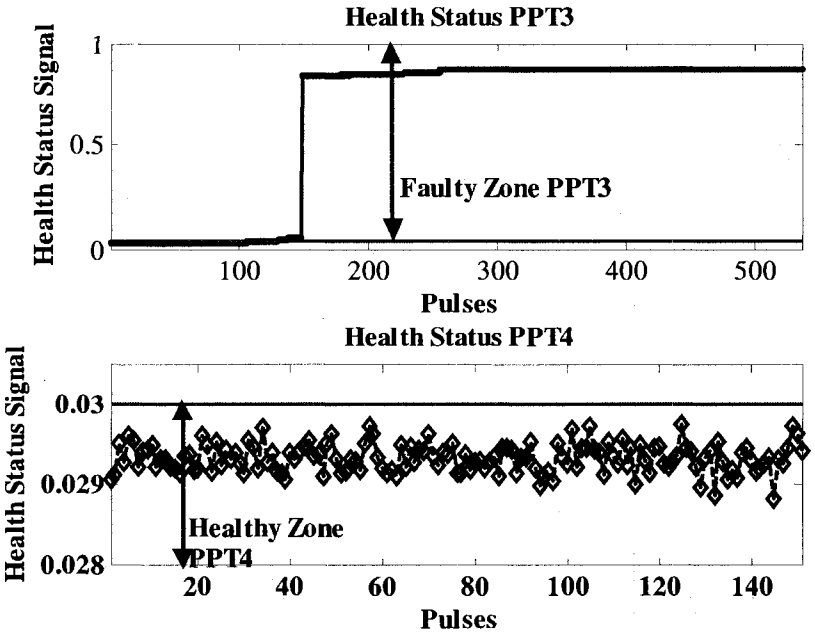

Figure 6.20. Health Status Signal for PPT_3/ PPT_4 (Fault Scenario 5).

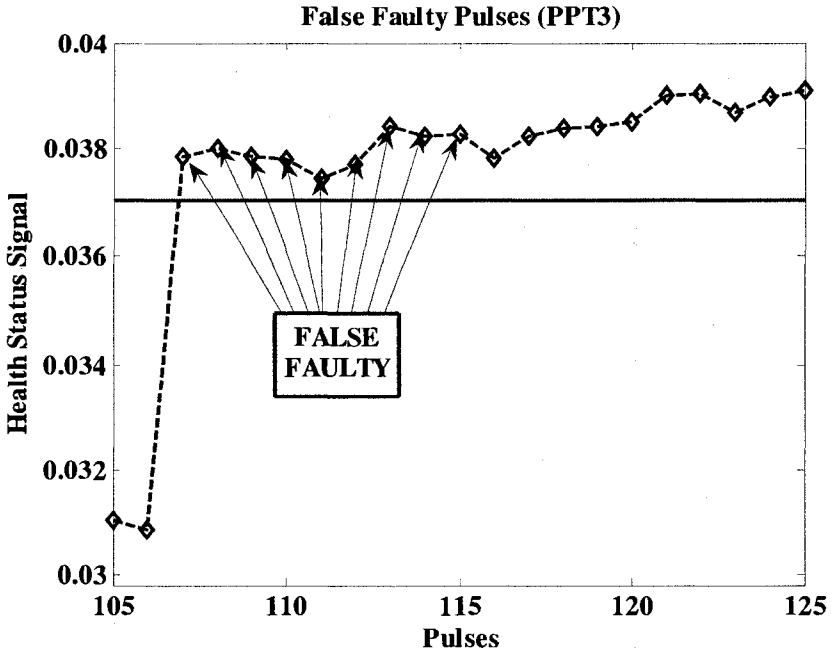

Figure 6.21. Misclassification of Pulses Generated by PPT_3 (Fault Scenario 5).

Fault Scenario 6 Results: Figures 6.22 shows the actual reduction in the amount of the torque that is generated by the thruster PPT_6 due to the fault that is injected after t = 400 sec. Meanwhile, some of the pulses that are generated by PPT_6 are outside the healthy zone, and all the pulses that are generated by PPT_5 are healthy. The first stage of our proposed "Integrated" FDI scheme estimates the three components of the angular velocity and then compares the estimates with the actual variables to generate the corresponding residuals (SAE_i). The results are shown in Table 6.XX.

	SAE_i	$Threshold_i$	$Health\ Status_i$
DNN_{Roll}	127.19	135.00	Healthy
DNN_{Pitch}	42.63	50.00	Healthy
DNN_{Yaw}	**160.73**	76.00	Faulty

Table 6.XX. Health Analysis Results Obtained by our Proposed FDI Approach for the Fault Scenario 6.

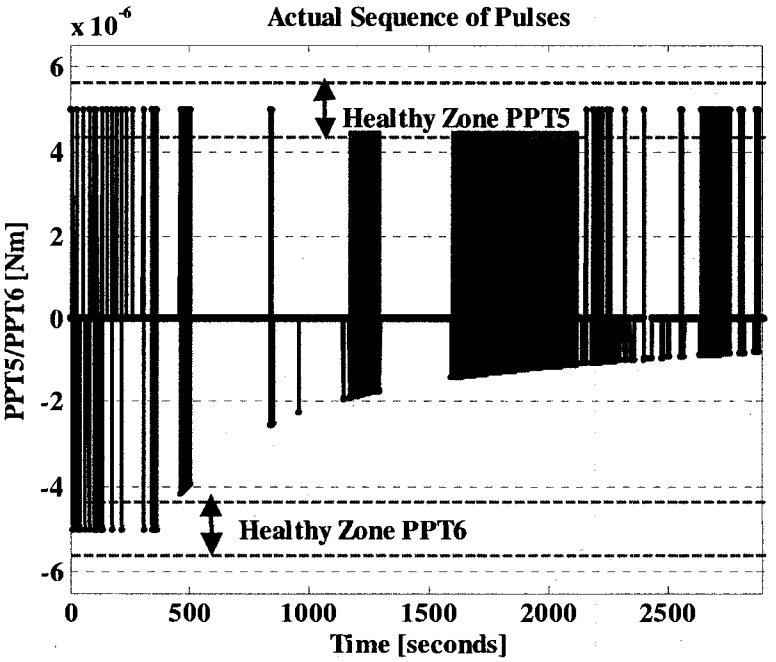

Figure 6.22. Actual Sequence of Pulses Generated by PPT_5/ PPT_6 for the Fault Scenario 6.

The fault is declared in the pair of thrusters PPT_5/ PPT_6. Based on the number of pulses that are generated by the pair, the Logic Threshold Selection Block defines the *Threshold* values for both thrusters. Table 6.XXI shows the resulting Thresholds.

	Number of Pulses	*Threshold Value*
PPT_5	256	0.0300 (Lower)
PPT_6	861	0.0370 (Upper)

Table 6.XXI. Logic Threshold Selection for the Fault Scenario 6.

Once the *Thresholds* are assigned, the proposed "Integrated" FDI scheme activates the second stage of the detection and isolation. Figure 6.23 shows the health status signal for PPT_5 and PPT_6 during the simulated period. According to the health status signals, the faulty pulses that are generated by PPT_6 start with the pulse number 41, meanwhile all the pulses that are generated by PPT_5 are healthy. Figure 6.24 shows the progressive increase of the fault severity in PPT_6. Table 6.XXII shows the final health monitoring results that are obtained by using our proposed "Integrated" FDI scheme.

	Actual Healthy Pulses	**Actual Faulty Pulses**	**Detected Healthy Pulses**	**Detected Faulty Pulses**	**Additional Information**
PPT_5	256	0	256	0	No fault detected
PPT_6	42	819	40	821	Faulty Case 1 or 3

Table 6.XXII. "Integrated" FDI Scheme Results for s/c_{f1} for the Fault Scenario 6.

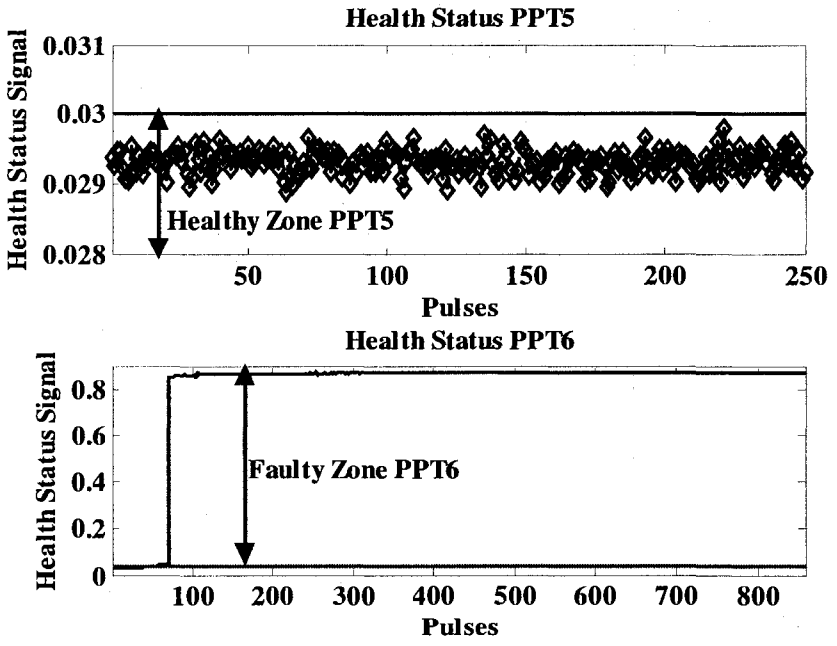

Figure 6.23. Health Status Signal for PPT_5/ PPT_6 (Fault Scenario 6).

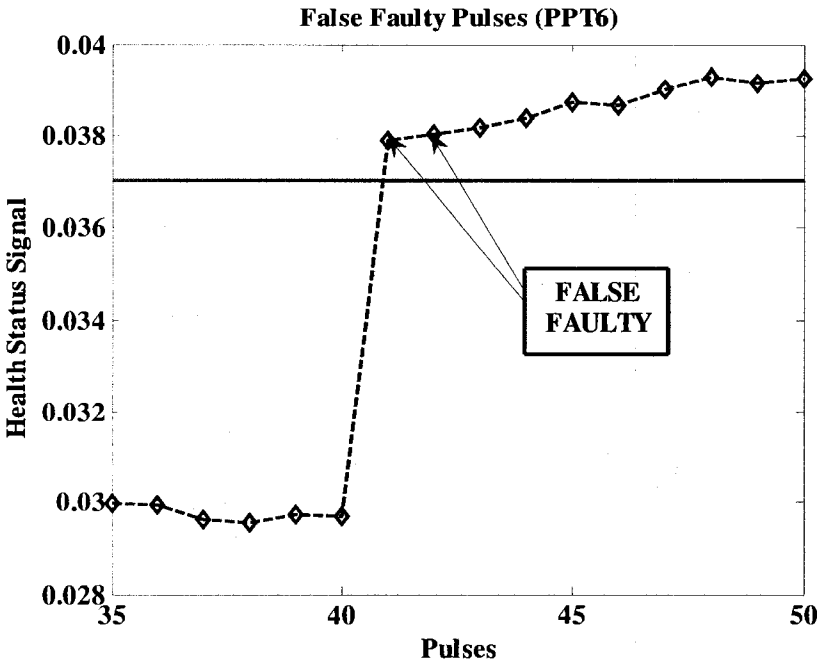

Figure 6.24. Misclassification of Pulses Generated by PPT_6 (Fault Scenario 6).

Fault Scenario 7 Results: Figures 6.25 shows the actual augmentation in the amount of the torque that is generated by the thruster PPT_3 due to the fault injected after t = 300 sec. Meanwhile, some of the pulses that are generated by PPT_3 are outside the healthy zone, and all the pulses that are generated by PPT_4 are healthy. The first stage of our proposed "Integrated" FDI scheme estimates the three components of the angular velocity and then compares the estimates with the actual variables to generate the corresponding residuals (SAE_i). The results are shown in Table 6.XXIII.

	SAE_i	$Threshold_i$	$Health\ Status_i$
DNN_{Roll}	123.31	135.00	Healthy
DNN_{Pitch}	**82.60**	50.00	Faulty
DNN_{Yaw}	45.60	76.00	Healthy

Table 6.XXIII. Health Analysis Results Obtained by our Proposed FDI Approach for the Fault Scenario 7.

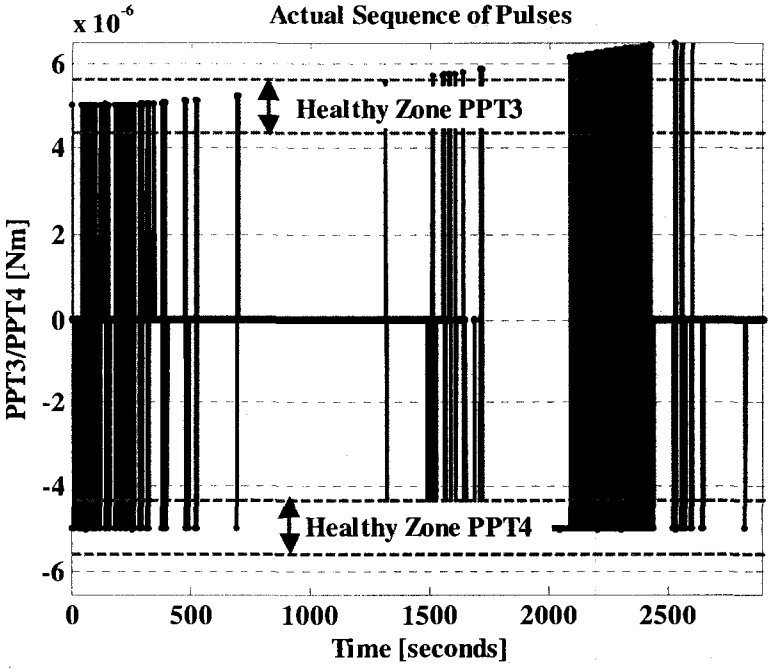

Figure 6.25. Actual Sequence of Pulses Generated by PPT_3/ PPT_4 for the Fault Scenario 7.

The fault is declared in the pair of thrusters PPT_3/ PPT_4. Based on the number of pulses that are generated by the pair, the Logic Threshold Selection Block defines the *Threshold* values for both thrusters. Table 6.XXIV shows the resulting Thresholds.

	Number of Pulses	*Threshold Value*
PPT_3	235	0.0300 (Lower)
PPT_4	849	0.0370 (Upper)

Table 6.XXIV. Logic Threshold Selection under Fault Scenario 7.

Once the *Thresholds* are assigned, the proposed "Integrated" FDI scheme activates the second stage of the detection and isolation. Figure 6.26 shows the health status signal for PPT_3 and PPT_4 during the simulated period. According to the health status signals, PPT_3 generates an isolated faulty pulse (number 80) and then starting with the pulse number 114 all the remaining generated pulses are faulty. All the pulses that are generated by PPT_4 are healthy. Figure 6.27 shows the progressive increase of the fault severity in PPT_3. Table 6.XXV shows the final health monitoring results that are obtained by using our proposed "Integrated" FDI scheme.

	Actual Healthy Pulses	Actual Faulty Pulses	Detected Healthy Pulses	Detected Faulty Pulses	Additional Information
PPT_3	114	121	112	123	Faulty Case 2
PPT_4	849	0	849	0	No fault detected

Table 6.XXV. "Integrated" FDI Scheme Results for s/c_{f1} for the Fault Scenario 7 Conditions.

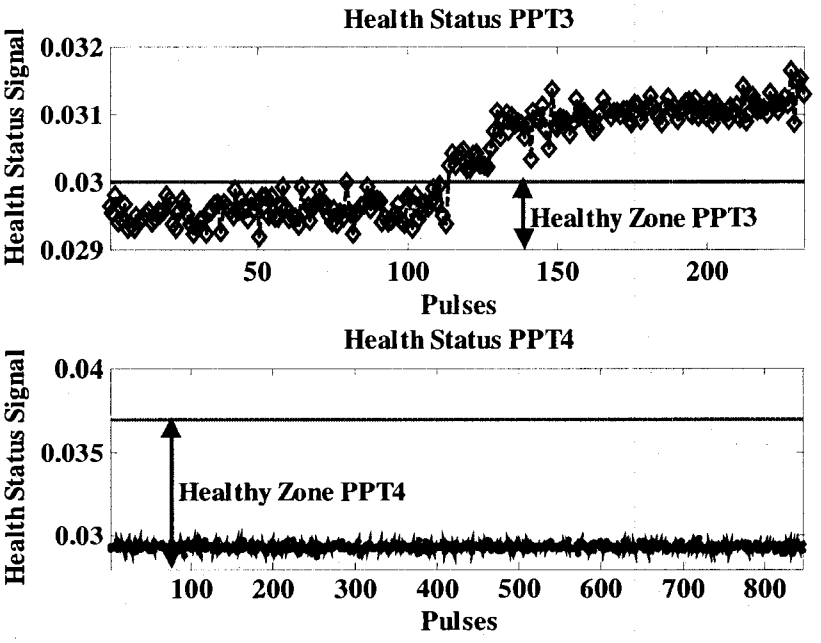

Figure 6.26. Health Status Signal for PPT_3/ PPT_4 (Fault Scenario 7).

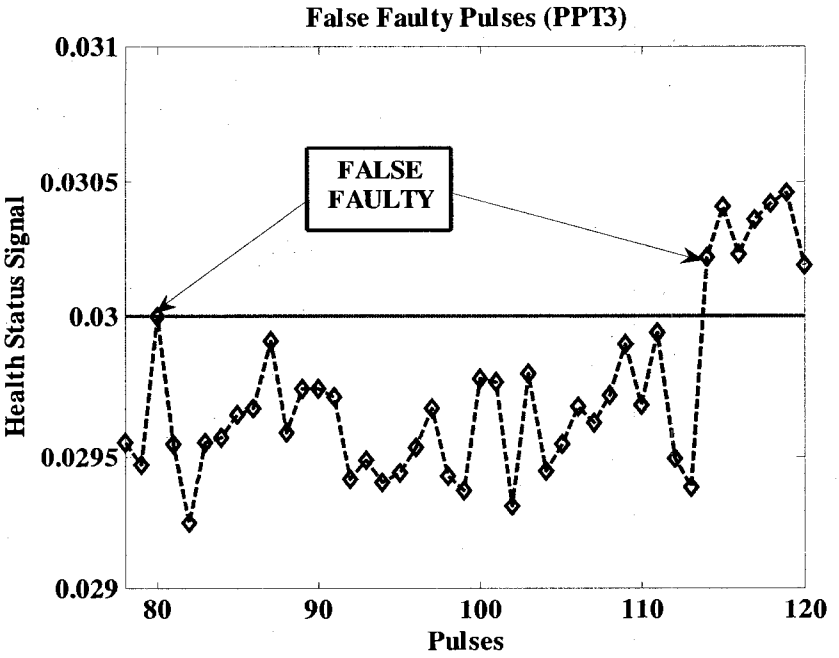

Figure 6.27. Misclassification of Pulses Generated by PPT_3 (Fault Scenario 7).

Fault Scenario 8 Results: Figures 6.28 shows the actual augmentation in the amount of the torque that is generated by the thruster PPT_4 due to the fault that is injected after t = 300 sec. Meanwhile, some of the pulses that are generated by PPT_4 are outside the healthy zone and all the pulses that are generated by PPT_3 are healthy. The first stage of our proposed "Integrated" FDI scheme estimates the three components of the angular velocity and then compares the estimates with the actual variables to generate the corresponding residuals (SAE_i). The results are shown in Table 6.XXVI.

	SAE_i	$Threshold_i$	$Health\ Status_i$
DNN_{Roll}	117.37	135.00	Healthy
DNN_{Pitch}	**92.07**	50.00	Faulty
DNN_{Yaw}	53.84	76.00	Healthy

Table 6.XXVI. Health Analysis Results Obtained by our Proposed FDI Approach for the Fault Scenario 8.

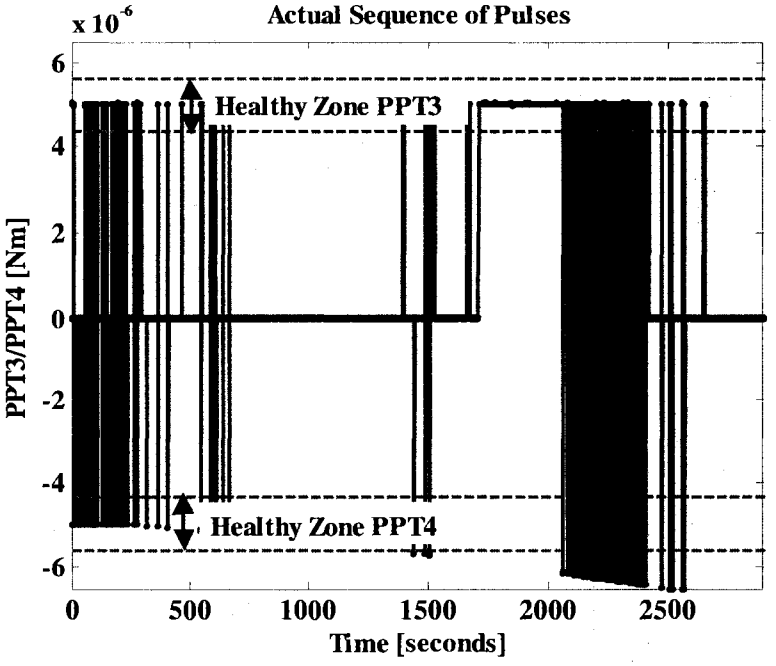

Figure 6.28. Actual Sequence of Pulses Generated by PPT_3/ PPT_4 for the Fault Scenario 8.

The fault is declared in the pair of thrusters PPT_3/ PPT_4. Based on the number of pulses that are generated by the pair, the Logic Threshold Selection Block defines the *Threshold* values for both thrusters. Table 6.XXVII shows the resulting Thresholds.

	Number of Pulses	*Threshold Value*
PPT_3	769	0.0370 (Upper)
PPT_4	191	0.0300 (Lower)

Table 6.XXVII. Logic Threshold Selection for the Fault Scenario 8.

Once the *Thresholds* are assigned, the proposed "Integrated" FDI scheme activates the second stage of the detection and isolation. Figure 6.29 shows the health status signals for PPT_3 and PPT_4 during the simulated period. According to the health status signals of PPT_4, there are five healthy pulses that are misclassified as faulty (pulses: 60, 62, 66, 70 and 75) and one faulty pulse misclassified as a healthy pulse (pulse number 81). As expected, all the pulses that are generated by PPT_3 are healthy. Figure 6.30 shows the progressive increase of the fault severity in PPT_4. Table 6.XXVIII shows the final health monitoring results that are obtained by using our proposed "Integrated" FDI scheme.

	Actual Healthy Pulses	**Actual Faulty Pulses**	**Detected Healthy Pulses**	**Detected Faulty Pulses**	**Additional Information**
PPT_3	769	0	769	0	No fault detected
PPT_4	76	115	71	120	Faulty Case 2

Table 6.XXVIII. 'Combined' FDI Scheme Results for s/c_{f1} for the Fault Scenario 8.

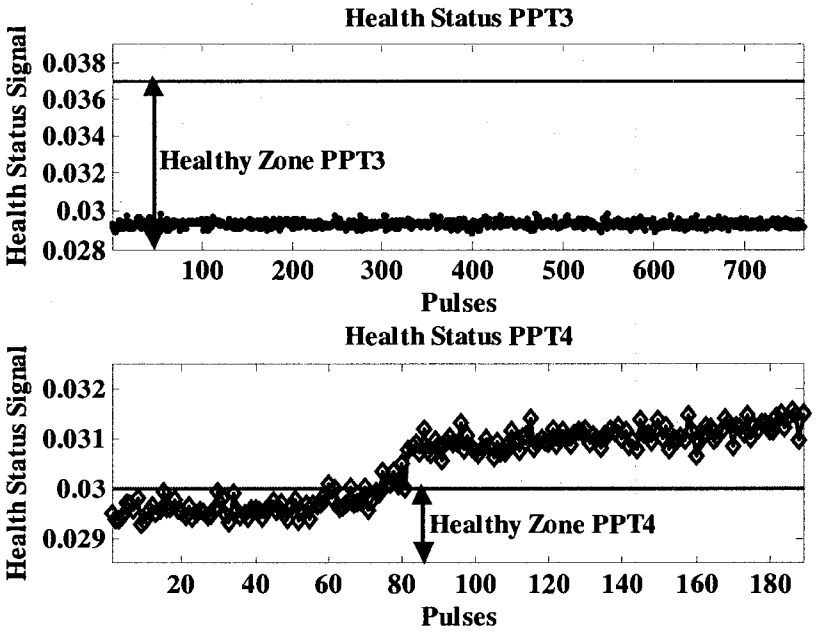

Figure 6.29. Health Status Signal for PPT_3/ PPT_4 (Fault Scenario 8).

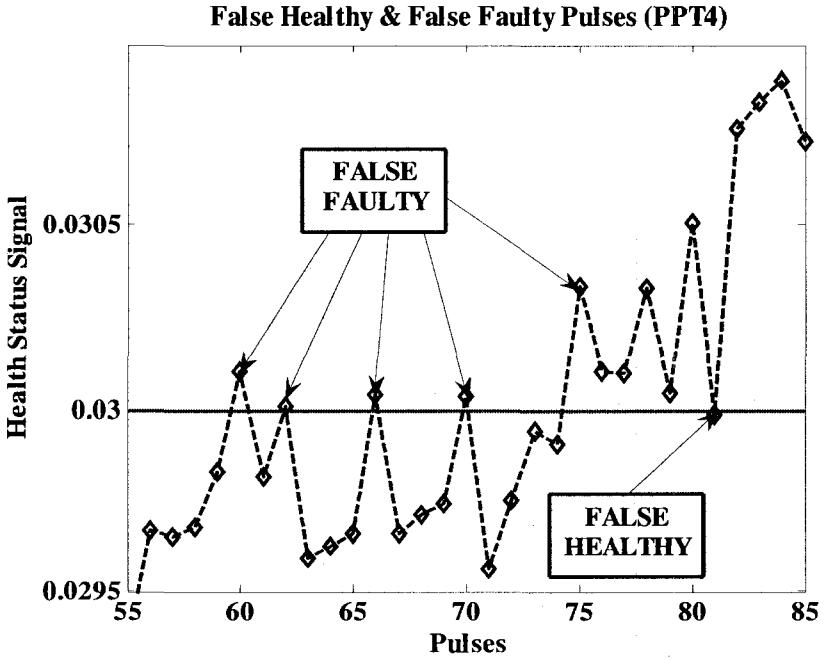

Figure 6.30. Misclassification of Pulses Generated by PPT_4 (Fault Scenario 8).

6.4. Confusion Matrix Results for the Integrated FDI Scheme

The performance of our proposed "Integrated" FDI scheme is studied using the Confusion Matrix as described in Chapter 4, Section 4.4. Table 6.XXIX contains the results for the four Confusion Matrix parameters evaluated for each of the fault scenarios. The last row of this table shows the overall results.

	TRUE FAULTY	FALSE HEALTHY	FALSE FAULTY	TRUE HEALTHY
Faulty Sc.1	2770	0	0	0
Faulty Sc.2	2883	0	0	5
Faulty Sc.3	108	0	7	541
Faulty Sc.4	44	0	0	338
Faulty Sc.5	433	0	6	259
Faulty Sc.6	819	2	0	296
Faulty Sc.7	121	0	2	961
Faulty Sc.8	115	0	5	840
TOTAL	**7293**	**2**	**20**	**3240**

Table 6.XXIX. Confusion Matrix for the Integrated FDI Scheme.

Similar to the evaluation that was performed in Chapter 4, Section 4.4, in case of our proposed "Integrated" FDI scheme we can calculate the corresponding six performance

parameters. Table 6.XXX provides the results that are obtained in this chapter that are compared with the results that are obtained in Chapter 4.

	"Low Level" FDI Scheme Performance Results	**"Integrated" FDI Scheme Performance Results**
Accuracy	88.89 [%]	**99.79 [%]**
True Healthy	96.09 [%]	**99.39 [%]**
False Healthy	42.37 [%]	**0.03 [%]**
True Faulty	57.63 [%]	**99.97 [%]**
False Faulty	3.90 [%]	**0.61 [%]**
Precision	66.67 [%]	**99.94 [%]**

Table 6.XXX. Performance Results for Our Proposed "Low Level" and "Integrated" FDI Schemes.

6.5. Conclusions

In this chapter, the strengths and weaknesses of the FDI schemes that were proposed in Chapters 4 and 5 are presented. The "High Level" FDI scheme (i.e. the FDI scheme proposed in Chapter 5) detects behavioral deviations in the relative attitudes of the followers spacecraft in a formation flying system. Meanwhile, the "Low Level" FDI scheme (i.e. the FDI scheme proposed in Chapter 4) detects abnormalities in the electromechanical behavior of the pulsed plasma thrusters.

An "Integrated" FDI scheme can take advantages of the strengths of each scheme and at same time reduces their individual weaknesses. The "High Level" FDI scheme is used for detecting faults that affects the relative attitudes of the spacecraft and identifying in which of the three pairs of thrusters the faulty PPT is located. The "Low Level" FDI scheme is used for detecting which thruster is the faulty one and, more specifically, which generated pulse is faulty. Finally, the implementation of the Logic Threshold Selection Block allows the "Low Level" FDI scheme to use different threshold values (i.e. Upper and Lower Thresholds) and therefore, improves its precision and accuracy levels.

To demonstrate the capabilities of the "Integrated" FDI scheme, various fault scenarios (i.e. eight fault scenarios) were simulated and the performance of the proposed FDI scheme was

evaluated. The results shown above demonstrate a significant improvement in the performance of the "Integrated" FDI scheme when compared to the "Low Level" FDI scheme. Our proposed approach exhibits a great level of accuracy as well as precision. Furthermore, the misclassification rate as expressed as False Healthy and False Faulty parameters is quite negligible. In addition to these important improvements, our proposed "Integrated" FDI scheme provides additional information that are related to the effects of the faults in the thrust production levels.

Chapter 7

Conclusions and Future Work

In this thesis, the problem of Fault Detection and Isolation (FDI) for satellite systems is investigated. The importance and necessity of a reliable FDI scheme for safety critical systems is discussed and spacecraft's attitude control subsystem (ACS) is considered as the focus of design and analysis. Formation flying systems is introduced where FDI schemes have not been extensively developed in the literature for this type of systems. An integrated FDI scheme for detecting and isolating faulty actuators (i.e. pulsed plasma thrusters (PPT)) of the formation flying spacecraft has been proposed and its capabilities are studied. The proposed FDI scheme is composed of a two-level dynamic neural networks (DNN) which uses the relative attitude variables of the formation flying spacecraft for detecting the occurrence of a fault and then uses the electrical variables of the PPTs for identifying the faulty PPT. The generated pulses that are faulty do provide information if the fault increases or decreases the amount of thrust produced by the actuator.

In Chapter 2, FDI systems that are developed in the literature for dynamical systems are reviewed. The set of desirable characteristic of an ideal FDI system is provided and the classification of different FDI techniques into model-based and history-based approaches is presented. Development of FDI systems for spacecraft with a special interest in unmanned formation flying spacecraft and their attitude control subsystems (ACS) are addressed. Two FDI approaches, namely model-based and history-based approaches are presented as examples of the actual level of development of FDI schemes for spacecraft systems. Finally, FDI systems for actuators in the ACS of spacecraft in formation flying missions are presented.

In Chapter 3, the concepts of coordinates systems and attitude representation techniques are defined and explained. The equations of motion that describe the rotational dynamics of a

spacecraft are presented and the concept of formation flying spacecraft is introduced. Formation flying control architectures and formation flying control laws are also provided and the design of the formation flying control law (i.e. the quaternion error vector command law for a formation of three spacecraft flying in a leader/follower architecture) are provided. The motivation for selecting the pulsed plasma thrusters (PPT) as the actuator of our formation flying spacecraft are presented and a dynamical model describing the PPT's electromechanical system and the PPT configuration (i.e. the so-called six-independent PPT configuration) are also provided. Finally, the dynamics of the formation flying and the PPT's electromechanical systems that are presented in this chapter are planned to be used to simulate the satellites' attitude maneuvers under normal and abnormal PPT's conditions. This has provided the required data for developing and testing our proposed FDI schemes.

In Chapter 4, a dynamic neural network-based fault detection and isolation scheme is developed to autonomously detect faults in a PPT actuator of a spacecraft. This scheme requires data from the electrical circuit of the thrusters thus avoiding a need for direct measurement of the thrust. Based on the simulation results presented it can be concluded that the proposed FDI scheme is not sufficiently capable of correctly classifying all of the faulty pulses that are generated during the experimental operations. The utilization of a fixed *Threshold* has resulted in inadequate capability for detecting faults under the three different faulty scenarios. Using a Confusion Matrix evaluation criteria we have demonstrated a high level of accuracy but the precision level is below expectations. Furthermore, the data set presented to the proposed scheme requires a sampling time of the order of milliseconds. For on-line fault diagnosis proposes, this amount of computational load may not be acceptable.

In Chapter 5, an alternative dynamic neural network-based fault detection and isolation scheme is developed to detect faults in the actuators of a follower spacecraft in a formation flying mission. This FDI scheme requires data from the attitude control subsystem of the follower spacecraft. According to the simulation results, one can conclude that the proposed scheme does

not require exhaustive computational load for detecting the presence of faults in the set of actuators, however for isolation purposes it does not work properly. Another characteristic of this approach is that the health monitoring analysis must be performed after the termination of the mission, implying that the fault detection cannot be performed in real-time.

In Chapter 6, the strengths and weaknesses of the "High Level" FDI scheme (i.e. the FDI scheme proposed in Chapter 5) and the "Low Level" FDI scheme (i.e. the FDI scheme proposed in Chapter 4) are discussed. An "Integrated" FDI scheme capable of taking advantages of the strengths of each scheme and at same time reducing their individual weaknesses is proposed. The "High Level" FDI scheme is used for detecting faults and for identifying in which of the three pairs of thrusters the faulty PPT is located. The "Low Level" FDI scheme is used for detecting which thruster is the faulty one and, more specifically, which generated pulse is faulty and the Logic Threshold Selection Block that is proposed allows the "Low Level" FDI scheme to use different threshold values to improve its precision and accuracy levels. Various fault scenarios were simulated and the performance of the proposed FDI scheme was evaluated and compared to the "Low Level" FDI scheme. Finally, our proposed "Integrated" FDI scheme exhibited a great level of accuracy as well as precision, meanwhile the misclassification rate of the False Healthy and the False Faulty parameters were quite insignificant. In addition to these important improvements, our proposed "Integrated" FDI scheme provides additional information that are related to the effects of the faults in the thrust production levels.

The proposed "Integrated" FDI scheme contains four dynamic neural networks, three in the first stage of detection and one in the second stage, which has to be implemented in each follower spacecraft. This approach does not require implementation of additional sensors, because it uses the data already used for other subsystems (e.g.: electrical variables and relative attitude variables). This FDI scheme proves to be a reliable health monitoring tool. The results obtained show high levels of accuracy (99.79%) and precision (99.94%) and the misclassification rate of the False Healthy (0.03%) and the False Faulty (0.61%) parameters are quite negliable. The

"Integrated" FDI scheme is also capable of detecting if the fault produces an increase or decrease in the amount of thrust generated by the faulty actuator.

7.2 Thesis Contributions

The contributions of the work developed in this thesis are detailed as follows:

- A novel Fault Detection and Isolation (FDI) scheme for Pulsed Plasma Thrusters (PPTs) of the Attitude Control Subsystem (ACS) of formation flying satellites has been proposed and tested. By means of four Dynamic Neural Networks (DNN) the proposed FDI scheme is capable of detecting and isolating faults of the actuators (i.e. PPTs) which affect the precision of the formation flying attitudes.
- The results obtained show high levels of accuracy (99.79%) and precision (99.94%) and the misclassification rate of the False Healthy (0.03%) and the False Faulty (0.61%) parameters are quite negligible. Therefore, the applicability of the DNN technique for solving fault diagnosis problems in highly complex nonlinear systems such as formation flying systems has been demonstrated.
- Although there are a number of results in the literature on fault diagnostic of the standard attitude control actuators (e.g. reaction wheels), the development of fault diagnostic systems for Pulsed Plasma Thrusters is not covered in the literature. Since the force generated by this actuators cannot be measured and due to the lack of precise mathematical models, the development of fault diagnostic system for PPTs is not a trivial work. In this thesis, we demonstrate that our proposed FDI scheme is a not computationally intensive and is a reliable tool for detecting and isolating faulty PPTs.
- Formation Flying missions are starting to gain popularity due to the advantages that are offered by these systems. A significant reduction in the amount of hours spent by the ground station personnel can be reached by implementing our proposed DNN-based FDI schemes. Therefore the cost of the mission can be significantly reduced.

7.3 Future Work

Based on the results obtained in this thesis, the suggested future work can be focused on the following areas: analysis for multiple fault scenarios (i.e. two or more faults affecting the same actuator or two or more actuators affected by faults concurrently) and the development of fault tolerant controllers or fault recovery systems which would allow the formation of spacecraft fulfills the mission objectives despite the presence of faults.

References

[1] S. P. Hughes, "Formation Flying Performance Measures for Earth-Pointing Missions," *Master Thesis, Aerospace Engineering, Virginia Polytechnic Institute and State University*, December 1999.

[2] M. Guelman, "Spacecraft Formation Flying," *Satellite Formation Flying and Applications Workshop*, July 2005.

[3] J. Sang-Pil Seo, "Analytical Solution for Low-Thrust Minimum Time Control of a Satellite Formation," *Department of the Air Force Air University, Air Force Insitute of Technology*, 2004.

[4] M. Mitchell, L. Breger, and J. P. How, "Effects of Navigation Filter Properties on Formation Flying Control," *AIAA Guidance, Navigation, and Control Conference and Exhibit*, August 2004.

[5] Z. Wang, and Y. Zhang, "Design and Verification of a Robust Formation Keeping Controller," *Journal of the International Academy of Astronautics*, Acta Astronautica, Vol. 61, Issues 7-8, pp. 565-574, October 2007.

[6] H. Wong, V. Kapila, and A. Sparks, "Adaptive Output Feedback Tracking Control of Multiple Spacecraft," *Proceedings of the American Control Conference*, June 2001.

[7] H. Wong, H. Pan, M. S. de Queiroz, and V. Kapila, "Adaptive Learning Control for Spacecraft Formation Flying," *Proceedings of the 40th IEEE Conference on Decision and Control*, December 2001.

[8] B. J. Naasz, "Classical Element Feedback Control for the Spacecraft Orbital Maneuvers," *Master Thesis, Aerospace Engineering, Virginia Polytechnic Institute and State University*, May 2002.

[9] V. Venkata, "Modelling and Control of Satellite Formations," *PhD Thesis, Aerospace Engineering, Texas A&M University,* May 2003.

[10] M. Tillerson, and J. P. How, "Formation Flying Control in Eccentric Orbits," *Proceedings of the AIAA Guidance, Navigation, and Control Conference*, August 2001.

[11] Y. Xu, N. Fitz-Coy, R. Lind, and A. Tatsch, "μ Control for Satellites Formation Flying," *Journal of Aerospace Engineering, ASCE*, January 2007.

[12] H. Wong, V. Kapila, and A. G. Sparks, "Adaptive Output Feedback Tracking Control of Spacecraft Formation," *International Journal of Robust and Nonlinear Control*, pp. 117-139, 2002.

[13] W. Ren, and R. W. Beard, "A Decentralized Scheme for Spacecraft Formation Flying via the Virtual Structure Approach," *Proceedings on the 2003 American Control Conference*, June 2003.

[14] M. Aung, A. Ahmed, M. Wette, D. Scharf, J. Tien, G. Purcell, and M. Regehr, "An Overview of Formation Flying Technology Development for the Terrestrial Planet Finder Mission," *Proceedings on the 2004 IEEE Aerospace Conference*, 2004.

[15] J. A. Roberts, "Satellite Formation Flying for an Interferometry Mission," *PhD Thesis, College of Aeronautics, Cranfield University*, October 2005.

[16] M. R. LaPointe, "Formation Flying with Shepherd Satellites," *Ohio Aerospace Institute, NIAC Phase I presentation*, October 2001.

[17] M. Campbell, R. R. Fullmer, and C. D. Hall, "The ION-F Formation Flying Experiments," *AAS/AIAA Space Flight Mechanics Meeting*, January 2000.

[18] S. Persson, P. Bodin, E. Gill, J. Harr, and J. Jorgensen, "PRISMA - An Autonomous Formation Flying Mission," *Small Satellite Systems and Services – The 4S Symposium*, September 2006.

[19] S. Gidlund, "Design Study for a Formation Flying Nanosatellite Cluster," *Master Thesis, Department of Space Science, Lulea University of Technology*, 2005.

[20] M. E. Campbell, V. Knagenhjelm, and J. Yingling, "Flight Software Development for the ION-F Formation Flying Mission," *IEEE Proceedings on Aerospace Conference 2001*,

2001.

[21] M. Campbell, A. P. Bruckner, G. Hwee, R. Ewig, S. Kaltenbech, E. Beltran, G. Lai, A. Nadkarni, E. Carlson, K. Parker, K. Carpenter, M. Peyton, S. Chung, S. Pillar, B. Davenport, W. M. Shell, F. Forouhar, D. Titus, J. K. Halligan, M. Tucker, J. Hammack, A. Vlachos, and Mark Hilstad, "UW Dawgstar: One Third of ION-F. An Element of the Ionospheric Obsevation Nanosatellite Formation (ION-F)," *13th AIAA/USU Conference on Small Satellites*, 1999.

[22] R. Sanchez, and P. Renard, "Design of a Micro-satellite for Precise Formation Flying Demonstration," *Fifth IAA International Conference on Low-Cost Planetary Missions*, September 2003.

[23] B. J. Makins, "Interferometer Architecture Trade Studies for the Terrestrial Planet Finder Mission," *Master Thesis, Massachusetts Institute of Technology*, February 2002.

[24] T. Yairi, Y. Kawahara, R. Fujimaki, Y. Sato, and K. Machida, "Telemetry-mining: A Machine Learning Approach to Anomaly Detection and Fault Diagnosis for Space Systems," *2nd IEEE International Conference on Space Mission Challenges for Information Technology*, 2006.

[25] B. Rubin, M. Guelman, and A. Kapulkin, "Principles of Hall Thruster Onboard Malfunction Diagnostics Based on Magnetic Field Measurements of Plasma Currents," *Proceeding of 4th International Spacecraft Propulsion Conference*, June 2004.

[26] E. Wilson, C. Lages, and R. Mah, "Gyro-based Maximum-Likelihood Thruster Fault Detection and Identification," *Proceedings of the 2002 American Control Conferences*, May 2002.

[27] E. Wilson, D. W. Sutter, D. Berkovitz, B. J. Betts, R. del Mundo, E. Kong, C. R. Lages, R. Mah, and R. Papasin, "Motion-based System Identification and Fault Detection and Isolation Technologies for Thruster Controlled Spacecraft," *Proceedings of the JANNAF 3rd Modeling and Simulation Joint Subcommittee Meeting*, December 2005.

[28] A. Barua, "A fault-tree approach for identifying causes of actuator failure in attitude control subsystem of space vehicles," *Msc Thesis*, Concordia University, 2004.

[29] I. Al-Dein Al-Zyoud, "Neural network-based actuator fault detection and isolation for the attitude control subsystem of a satelite," *Msc Thesis*, Concordia University, 2005.

[30] F. Piromoradi, F. Sassini, and C. W. da Silva, "An Efficient Algorithm for Health Monitoring and Fault Diagnosis in a Spacecraft Attitude Determination System," *IEEE International Conference on System, Man and Cybernetics ISIC*, October 2007.

[31] N. Venkateswaran, M. S. Silva, and P. S. Goel, "Analytical Redundancy Based Fault Detection of Gyroscopes in Spacecraft Applications," *International Astronautical Federation, Acta Astronautica*, Vol. 50, No 9, pp. 535-545, 2002.

[32] E. C. Larson, B. E. Parker Jr., and B. R. Clark, "Model-Based Sensor and Actuator Fault Detection and Isolation," *Proceedings of the American Control Conference*, May 2002.

[33] B. M. Gardner, G. Jongeward, and I. Katz, "An Analysis of the Ion Thruster Impact on New Millennium Spacecraft Subsystems," *Proceedings of the 31st Intersociety of Energy Conversion Engieering Conference IECEC 96*, Vol. 1, pp. 438-443, August 1996.

[34] T. J. Stueber, "Discharge Chamber Primary Electron Modeling Activities in 3-Dimension," *40th AIAA/ASME/SAE/ASEE Joint Propulsion Conference and Exhibit*, July 2004.

[35] R. E. Wirz, "Discharge Plasma Processes of Ring-Cusp Ion Thrusters," *PhD Thesis, California Institute of Technology*, 2005.

[36] R. Wirz, and D. Goebel, "Ion Thruster Discharge Performance per Magnetic Field Topography," *42nd AIAA/ASME/SAE/ASEE Joint Propulsion Conference*, July 2006.

[37] R. Wirz, "Discharge Hollow Cathode and Extraction Grid Analysis for the MiXI Ion Thruster," *42nd AIAA/ASME/SAE/ASEE Joint Propulsion Conference*, July 2005.

[38] S.W. Kim, "Experimental Investigations of Plasma Parameters and Species-Dependent Ion Energy Distribution in the Plasma Exhaust Plume of a Hall Thruster," *PhD Thesis,*

Aerospace Engineering, University of Michigan, 1999.

[39] M. Keidar, I. D. Boyd, and J. Parrilla, "Modeling of the Plasma Flow in High-Power TAL," *39th AIAA/ASME/SAE/ASEE Joint Propulsion Conference*, July 2003.

[40] R. R. Hofer, and A. D. Gallimore, "Efficiency Analysis of a High-Specific Impulse Hall Thruster," *40th AIAA/ASME/SAE/ASEE Joint Propulsion Conference*, July 2004.

[41] D. Manzella, J. Yim, and I. Boyd, "Predicting Hall Thruster Operational Lifetime," *40th AIAA/ASME/SAE/ASEE Joint Propulsion Conference and Exhibit*, July 2004.

[42] J. T. Yim, M Keidar, and I. D. Boyd, "A Hydrodynamic-Based Erosion Model for Hall Thruster," *29th International Electric Propulsion Conference*, November 2005.

[43] D. T. Jacobson, and R. S. Jankovsky, "Test Results of a 200W Class Hall Thruster," *34th AIAA/ASME/SAE/ASEE Joint Propulsion Conference and Exhibit*, July 1998.

[44] R. R. Hofer, and R. S. Jankovsky, "A Hall Thruster Performance Model Incorporating the Effects of a Multy-Charged Plasma," *37th AIAA/ASME/SAE/ASEE Joint Propulsion Conference and Exhibit*, July 2001.

[45] L. R. Pinero, P. Y. Peterson, and G. E. Bowers, "High Performance Power Module for Hall Effect Thrusters," *38th AIAA/ASME/SAE/ASEE Joint Propulsion Conference and Exhibit*, July 2002.

[46] A. Smirnov, Y. Raitses, and N. J. Fisch, "Electron Cross-field Transport in a Miniaturized Cylindrical Hall Thruster," *IEEE Transactions on Plasma Science*, April 2006.

[47] V. Hruby, M. Ganero-Castano, D. Spence, C. Gasdaska, N. Demmons, R. McCormick, P. Falkos, J. Young, and W. Connolly, "Colloid Thrusters for the New Millennium, ST7 DRS Mission," *Proceedings on the 2004 IEEE Aerospace Conference*, 2004.

[48] J. Carretero, and M. Martinez-Sanchez, "Numerical Simulation of a Colloidal Thruster in the Droplet Regime," *Journal of Computer Physics Communications*, Vol. 164, pp. 202-208, 2004.

[49] P. Lozano, "Studies on the Ion-Droplet Mixed Regime in Colloid Thrusters," *PhD Thesis,*

Department of Aeronautics and Astronautics, MIT, February 2003.

[50] K. Sankaran, L. Martinelli, and E. Y. Choueiri, "A Flux-Limited Numerical Method for the MHD Equations to Simulate Propulsive Plasma Flows," *31st AIAA Plasmadynamics and Lasers Conference*, June 2006.

[51] P. J. Turchi, "The Effects of Magnetic Nozzle Configurations on Plasma Thrusters," *Final Contractor Report NASA CR-202341*, May 1997.

[52] M. R. LaPointe, E. Strzempkowski, and E. Pencil, "High Power MPD Thruster Performance Measurements," *40th AIAA/ASME/SAE/ASEE Joint Propulsion Conference and Exhibit*, July 2004.

[53] E. Martines, F. Paganucci, M. Zuin, M. Bagatin, R. Cavazzana, P. Rossetti, G. Serianni, M. Signori, V. Antoni, and M. Andrenucci, "Efficiency Enhancement due to Kink Inestability Suppression in MPD Plasma Thrusters," *32nd EPS Conference on Controlled Fusion and Plasma Physics*, June 2005.

[54] E. J. Pencil, H. Kamhawi, L. A. Arrington, "Overview of NASA's Pulsed Plasma Thruster Development Program," *40th AIAA/ASME/SAE/ASEE Joint Propulsion Conference and Exhibit*, July 2004.

[55] J. K. Ziemer, E. Y. Choueiri, and R. G. Jahn, "Scaling Laws for Pulsed Electric Propulsion with Application to the Pluto Express Mission," *24th International Electric Propulsion Conference IEPC 95*, Vol. 2, pp. 981-994, 1996.

[56] W. J. Guman, and D. J. Palumbo, "Pulsed Plasma Propulsion System for North-South Stationkeeping," *International Electric Propulsion Conference, American Institute of Aeronautics and Astronautics*, November 1976.

[57] W. A. Hoskins, M. J. Wilson, M. J. Willey, N. J. Meckel, M. Campbell, and S. Chung, "PPT Development Effors at Primex Aerospace Company," *35th AIAA/ASME/SAE/ASEE Joint Propulsion Conference and Exhibit*, June 1999.

[58] D. R. Bromaghim, G. G. Spanjers, R. A. Spores, R. L. Burton, D. Carroll, and J. H.

Schilling, "A Proposed On-Orbit Demonstration of an Advanced Pulsed-Plasma Thruster for Small Satellite Applications," *Defense Technical Information Center OAI-PMH Repository*, 1998.

[59] R. M. Myers, S. R. Oleson, M. McGuire, N. J. Meckel, and J. Cassady, "Pulsed Plasma Thruster Technology for Small Satellite Missions," *9th Annual Small Satellite Conference*, September 1995.

[60] M. L. McGuire, and Roger M. Myers, "Pulsed Plasma Thrusters for Small Spacecraft Attitude Control," *NASA/GSFC Flight Mechanics/Estimation Theory Symposium*, 1996.

[61] T. Edamitsu, and H. Tahara, "Experimental and Numerical Study of an Electrothermal Pulsed Plasma Thruster for Small Satellites," *5th International Symposium on Applied Plasma Science*, Vol. 80, pp. 1223-1228, September 2005.

[62] C. Zakrzwski, J. Cassady, S. Benson, and P. Sanneman, "Pulsed Plasma Thruster (PPT) Summary,"eo1.gsfc.nasa.gov/new/validationReport/Technology/Documents/Summaries/08-PPT_Rev-0.pdf.

[63] C. Zakrzwski, S. Benson , J. Cassady, and P. Sanneman, "Pulsed Plasma Thruster (PPT) Validation Report," *NASA/GSFC*, June 2002.

[64] T. Hiroyuki, I. Masaaki, A. Akira, and H. Kunihiko, "Spatial Distribution of Lorentz Forces in an Applied-Field Magneto-Plasma-Dynamic Arcjet Plasma," *Journal of Plasma and Fusion Research*, Vol. 80, No. 8, 2004.

[65] C. Rossi, B. Larangot, P. Pham, D. Briand, N. R. de Rooij, M. Puig-Vidal, and J. Samitier, "Solid Propellant Microthrusters on Silicon: Design, Modeling, Fabrication, and Testing," *Journal of Microelectromechanical Systems*, Vol. 15, No. 6, December 2006.

[66] S. Anghaie, and T. W. Kinght, "Development of a Robust Tri-Carbide Fueled Reactor for Multi-Megawatt Space Power and Propulsion Applications," *Transactions Of The American Nuclear Society 2004 Winter Meeting*, November 2004.

[67] V. Venkatasubramanian, R. Rengaswany, K. Yin, and S. N. Kavuri, "A review of process

fault detection and diagnosis – Part I Quantitative model-based methods," *Computers & Chemical Engineering*, Vol. 27, No. 3, pp. 293 – 311, March 2003.

[68] X. Hu, "Intelligent Fault Diagnosis in Computer Networks," *Technical University of Denmark, Informatics and Mathematical Modelling Building*, IMM-Thesis-2007-49, May 2007.

[69] S. Katipamula, and M. R. Brambley, "Methods for Fault Detection, Diagnostics, and Prognostics for Building Systems – A Review, Part II," *American Society of Heating, Refrigerating and Air-Conditioning Engineers, Inc.*, Vol. 11, No 2, April 2005.

[70] M. C. Comstock, and J. E. Braun, "Literature Review for Applications of Fault Detection and Diagnostic Methods to Vapor Compression Cooling Equipment," *Research Project 1043-RP, Report #4036-2*, December 1999.

[71] S. Poyhonen, "Support Vector Machine Based Classification in Condition Monitoring of Induction Motors," *Helsinki University of Technology Control Engineering Laboratory*, June 2004.

[72] V. Venkatasubramanian, R. Rengaswany, K. Yin, and S. N. Kavuri, "A review of process fault detection and diagnosis – Part II Qualitative models and search strategies," *Computers & Chemical Engineering*. Vol 27, No 3, pp. 313 – 326, March 2003.

[73] V. Venkatasubramanian, R. Rengaswany, K. Yin, and S. N. Kavuri, "A review of process fault detection and diagnosis – Part III history based methods," *Computers & Chemical Engineering*. Vol 27, No 3, pp. 327 – 346, March 2003.

[74] E. Frisk, "Residual Generation for Fault Diagnosis," *PhD Thesis, Department of Electrical Engineering, Linkoping University,* Sweden 2001.

[75] O. Durou, V. Godet, L. Mangane, D. Perarnaud, and R. Roques, "Hierarchical Fault Detection, Isolation and Recovery Applied to COF and ATV Avionics," *Acta Astronautica*, Vol.50, No 9, pp. 547-556, 2002.

[76] A. Joshi, V. Gavriloiu, A. Barua, A. Garabedian, P. Sinha, and K. Khorasani, "Intelligent

and Learning-based Approaches for Health Monitoring and Fault Diagnosis of RADARSAT-1 Attitude Control System," *IEEE International Conference on System, Man and Cybernetics ISIC*, October 2007.

[77] M. Lavagna, G. Sangiovanni, and A. Da Costa, "Modelization, Failures Identification and High-level Recovery in Fast Varying Non-linear Dynamical Systems for Space Autonomy," *6th International Conference on Dynamics and Control of Systems and Structures in Space 2004*, July 2004.

[78] A. M. Salkham, "Fault Detection, Isolation and Recovery (FDIR) in On-Board Software," *Master's Thesis, Department of Computer Science and Engineering, Chalmers University of Technology*, 2005.

[79] A. Guiotto, A. Martelli, and C. Paccagnini, "SMART-FDIR: Use of Artificial Intelligence in the Implementation of a Satellite FDIR," *Data Systems in Aerospace DASIA 2003*, June 2003.

[80] N. Holsti, and M. Paakko, "Towards Advanced FDIR Components," *Proceedings of the DASIA 2001 Conference*, June 2001.

[81] P. S. Morgan, "Fault Protection Techniques in JPL Spacecraft," *1st International Forum on Integrated System Health Engineering and Management in Aerospace ISHEM*, November 2005.

[82] J. R. Carnes, and A. Misra, "Model-Integrated Toolset for Fault Detection, Isolation and Recovery (FDIR)," *IEEE Symposium and Workshop on Engineering of Computer-Based Systems, 1996*, March 1996.

[83] E. I. Grotli, "Modeling and Control of Formation Flying Satellites in 6 DOF," *Master Thesis, Norwegian University of Science and Technology*, June 2005.

[84] Juergen Schlutz, "Attitude and Orbit Control of Small Satellites Using Thruster Systems," *Diploma Thesis, Institute of Flight Dynamics and Control (IFR) of the University of Stuttgart*, 2005.

[85] D. P. Scharf, F. Y. Hadaegh, and S. R. Ploen, "A Survey of the Spacecraft Formation Flying Guidance and Control (Part II): Control," *Proceeedings of the 2004 American Control Conference ACC*, pp. 2976-2985, 2004.

[86] H. Weidong, and Z. Yulin, "Rate Damping Control for Small Satellite using Thruster," *Journal of the International Academy of Astronautics, Acta Astronautica*, Vol. 55, pp. 9-13, July 2004.

[87] T. R. Krogstad, "Attitude Control of Satellites in Clusters," *Master Thesis, Department of Engineering Cybernetics, Norwegian University of Science and Technology*, June 2005.

[88] M. C. VanDyke, "Decentralized Coordinated Attitude Control of a Formation of Spacecraft," *Aerospace Engineering, Virginia Polytechnic Institute and State University*, May 2004.

[89] P. K. C, Wang, and F. Y. Hadaegh, "Coordination and Control of Multiple Microspacecraft Moving un Formation," *Journal of the Astronautical Sciences*, pp. 315-355, 1996.

[90] B. J. Naasz, M. M. Berry, H. Y. Kim, and C. D. Hall, "Integrated Orbit and Attitude Control for a Nanosatellite with Power Constraints," *2003 AAS/AIAA Space Flight Mechanics Conference*, February 2003.

[91] S. E. Lennox, "Coupled Orbital and Attitude Control Simulations for Spacecraft Formation Flying," *2004 AIAA Region I-MA Student Conference*, April 2004.

[92] W. Ren, and R. W. Beard, "Formation Feedback Control for Multiple Spacecraft via Virtual Structures," *IEE Proceedings on the Control Theory Applications*, Vol. 151, No 3, May 2004.

[93] J. Y. Tien, G. H. Purcell, L. R. Amaro, L. E. Young, M. Aung, J. M. Srinivasan, E. D. Archer, A. M. Vozoff, and Y. Chong, "Technology Validation of the Autonomous Formation Fying Sensor for Precision Formation Flying," *Proceedings on the 2003 IEEE Aerospace Conference*, Vol. 1, March 2003.

[94] R. J. Cassady, N. J. Meckel, W. A. Hoskins, R. M. Myers, S. R. Oleson, and M. McGuire, "Pulsed Plasma Thruster Systems for Spacecraft Attitude Control," *10 th AIAA/USU Conference on Small Satellites*, September 1996.

[95] J. K. Ziemer, E. A. Cubbin, and E. Y. Choueiri, "Pulsed Plasma Propulsion for a Small Satellite: COMPASS P^3OINT," *32nd AIAA/ASME/SAE/ASEE Koint Propulsion Conference and Exhibit*, July 1996.

[96] C. Rayburn, P. Hall, and T. Mattick, "UW Dawgstar/ION-F CDR Document: Propulsion Subsystem (Prop)," *Department of Aeronautics & Astronautics, University of Washington*, October 2000.

[97] R. J. Cassidy, W. A. Hoskins, M. Campbell, and C. Rayburn, "A Micro Pulsed Plasma Thruster (PPT) for the 'Dawgstar' Spacecraft," *Proceedings on the 2000 IEEE Aerospace Conference*, Vol. 4, pp. 7-14, 2000.

[98] S. W. Benson, L. A. Arrigton, W. A. Hoskins, and N. J. Meckel, "Development of a PPT for the EO-1 Spacecraft," 35th *AIAA/ASME/SAE/ASEE Joint Propulsion Conference and Exhibit*, June 1999.

[99] M. Keidar, and I. D. Boyd, "Optimization Issues for a Micro-Pulsed Plasma Thruster," *40th AIAA/ASME/SAE/ASEE Joint Propulsion Conference*, July 2004.

[100] L. A. Arrington, and T. W. Haag, "Multi-Axis Thrust Measurements of the EO-1 Pulsed Plasma Thruster," *35th AIAA/ASME/SAE/ASEE Joint Propulsion Conference and Exhibit*, June 1999.

[101] A. M. Johnson, "Analysis of the Feasibility of Demonstrating Pulsed Plasma Thrusters on FalconSAT-3,".

[102] L. B. King, G. G. Parker, and M. D. Tervo, "POWERSAIL Propulsion System Design Trade Study," *Final Report for AFRL Contract No. F04700-01-P-0048*, September 2001.

[103] K. Patan, "Training of the Dynamic Neural Networks via Constrained Optimisation," *IEEE International Joint Conference on Neural Networks.*, vol. 1, pp. 195-200, Jul. 2004.

[104] K. Patan, and T. Parisini, "Identification of Neural Dynamic Models for Fault Detection and Isolation: the Case of a Real Sugar Evaporation Process," *Journal of Process Control*, pp. 67-79, 2005.

[105] K. Patan, "Fault detection of actuators using dynamic neural networks," *2nd Damadics Workshop on Neural Methods for Modelling and Fault Diagnosis*, May 2003.

[106] R. J. Vondra, "A final report on the LES 8/9 pulsed plasma thruster," *AIAA International Electric Propulsion Conference*, AIAA-1976-998, Nov 1976.

[107] H. Kamhawi, P. J. Turchi, R. J. Leiweke, and R. M. Myers, "Design and operation of a laboratory benchmark PPT," *ASME, SAE, and ASEE, 32nd Joint Propulsion Conference and Exhibit*, AIAA-1996-2732, Jul. 1996.

[108] G. Aston and L. C. Pless, "Ignitor plug erosion and arc initiation processes in a one-millipound pulsed plasma thruster," *15th International Electric Propulsion Conference*, pp. 1-8, 1981.

[109] V. Khayms, "Advanced Propulsion for Microsatellites," *PhD Thesis, Department of Aeronautics & Astronautics MIT*, June 2000.

[110] K. A. Polzin, E. Y. Choueiri, P. Gurfil, and N. J. Kasdin, "Plasma Propulsion Options for Multiple Terrestrial Planet Finder Architectures," *Journal of Spacecraft and Rockets*, Vol. 39, pp. 347-356, 2002.

[111] B. S. Yang, T. Han, and J. L. An, "ART-KOHONEN Neural Network for Fault Diagnosis of Rotating Machinery," *Mechanical Systems and Signal Processing*, pp. 645-657, 2004.

[112] A. T. Vemuri, and M. M. Polycarpou, "Neural-Network-Based Robust Fault Diagnosis in Robotic Systems," *IEEE Transactions on Neural Networks*, Vol. 8 No. 6, November 1997.

[113] R. Tinos, and M. H. Terra, "Fault Detection and Isolation in Robotic Manipulators using a Multilayer Perceptron and a RBF Network Trained by the Kohonen's Self-Organizing Map," *SBA Controle & Automacao*, Vol. 12, No. 1, 2001.

[114] F. J. Uppal, and R. J. Patton, "Fault Diagnosis of an Electro-pneumatic Valve Actuator

using Neural Networks with Fuzzy Capabilities," *ESANN'2002 Proceedings – European Symposium on Artifical Neural Networks*, pp. 501-506, April 2002.

[115] T. Torigoe, M. Konishi, J. Imai, and T. Nishi, "Application of Neural Network to Fault Diagnosis of Electro-Mechanical System," *Memoirs of the Faculty of Engineering, Okayama University*, Vol. 39, pp. 21-27, January 2005.

[116] P. Xu, S. Xu, and H. Yin, "Application of Self-Organaizing Competitive Neural Network in Fault Diagnosis of Suck Rod Pumping System," *Journal of Petroleum Science and Engineering*, 2006.

[117] T. Marcu, L. Mirea, and P. M. Frank, "Neural Observer Scheme for Robust Detection and Isolation of Process Faults," *UKACC International Conference on Control*, September 1998.

[118] Q. Chen, Y. W. Chan, and K. Worden, "Structural Fault Diagnosis and Isolation using Neural Networks Based on Response-Only Data," *Computers and Structures*, pp. 2165-2172, 2003.

[119] C. Wang, Y. Xie, and G. Chen, "Fault Diagnosis Based on Radial Basis Function Neural Network in Analog Circuits," *ICCCAS 2004 International Communications, Circuits and Systems*, Vol. 2, pp. 1183-1185, June 2004.

[120] K. S. Swarup, and H. S. Chandrasekharalah, "Power System Fault Diagnosis using Artificial Neural Networks," *Proceedings of XVI Annual Convention and Exhibition of the IEEE In India*, pp. 81-85, 1990.

[121] Y. Ma, L. Ma, and J. Ma, "RBF Neural Network Based Fault Diagnosis for the Thermodynamic System of a Thermal Power Generating Unit," *Proceedings of the Fourth International Conference on Machine Learning and Cybernetics*, August 2005.

[122] J. Korbiez, A. Obuchowicz, and K. Patan, "Network of Dynamic Neuron in Fault Detection Systems," *1998 IEEE International Conference on Systems, Man, and Cybernetics*, Vol. 2, pp. 1862-1867, November 1998.

[123] I. Al-Dein Al-Zyoud and K. Khorasani, "Detection of Actuator Faults Using a Dynamic Neural Network for the Attitude Control Subsystem of a Satellite," *Proceedings of International Joint Conference on Neural Networks*, 2005.

[124] R. Saeks, M. Lothers, R. Pap, and K. Mach, "A Neural Network Based Approach to Fault Diagnosis in Aerospace Systems," *IEEE Systems Readiness Technology Conference*, pp. 271-273, September 1992.

[125] H. Y. Hao, Z. Sun, and Y. Zhang, "Fault Diagnosis on Satellite Attitude Control with Dynamic Neural Network," *Lecture Notes in Computer Science, Advances in Neural Networks*, Vol. 3174, pp. 537-542, July 2004.

[126] Z. Q. Li, L. Ma, and K. Khorasani, "Dynamic Neural Network-Based Fault Diagnosis for Attitude Control Subsystem of a Satellite," PRICAI 2006, LNAI 4099, pp. 308-318, 2006.

[127] I. Al-Dein Al-Zyoud and K. Khorasani, "Neural Network-based Actuator Fault Diagnosis for Attitude Control Subsystem of an Unmanned Space Vehicle," *International Joint Conference on Neural Networks*, Jul. 2006.

[128] K. Patan, and T. Parisini, "Stochastic Learning Methods for Dynamic Neural Networks: Simulated and Real-Data Comparasions," *Proceedings of the 2002 American Control Conference, ACC'02*, pp. 2577-2582, May 2002.

[129] M. Ayoubi, "Nonlinear Dynamic Systems Identification with Dynamic Neural Networks for Fault Diagnosis in Technical Processes," *IEEE International Conference on Systems, Man, and Cybernetics.*, Vol. 3, pp. 2120–2125, Oct. 1994.

[130] P. CAmpolucci, F. Piaza, and A. Uncini, "On-Line Algorithms for Neural Networks with IIR Synapses," *Proceedings of IEEE Int. Conference on Neural Networks, ICNN-95*, December 1995.

[131] P. Campolucci, A. Uncini, and F. Piazza, "Fast Adaptive IIR-MLP Neural Networks for Signal Processing Applications," *Proceedings of the IEEE International Conference on Acoustics, Speech, and Signal Processing ICASSP-96*, Vol. 6, pp. 3529-3532, May 1996.

[132] P. Campolucci, S. Fiori, A. Uncini, and F. Piazza, "A New IIR-MLP Learning Algorithm for On-Line Signal Processing," *IEEE International Conference on Acoustics, Specch, and Processing (ICASSP 97)*, Vol. 4, 1997.

[133] "Computer Science 831: Knowledge Discovery in Databases," Available: http://www2.cs.uregina.ca/~dbd/cs831/notes/confusion_matrix/confusion_matrix.html

[134] D. D. Laperriere, "Electromechanical Modelling and Open-Loop Control of Parallel-Plate Pulsed Plasma Microthrusters with Applied Magnetic Fields," *Master Thesis, Department of Mechanical Engineering, Worchester Polytechnic Institute*, June 2005.

[135] S. J. Qin, amd W. Li, "Detection and Identification of Faulty Sensors with Maximized Sensitivity," *Proceedings of American Control Conference AACC*, June 1999.

[136] N. Viswanadahn, and K. D. Minto, "Fault Diagnosis in Multirate Sampled Data Systems," *Proceedings of the 29th Conference on Decision and Control IEEE*, December 1990.

[137] H. Niemann, and J. Stoustrup, "An Architecture for Fault Tolerant Controllers," *International Journal of Control*, Vol. 78, No 14, pp. 1091 – 1110, September 2005.